Electrochemistry of Hydrazine

A thesis submitted for the degree of

Doctor of Philosophy

in Physical and Theoretical Chemistry

Ruiyang Miao

Merton College

Trinity Term 2021

Contents

Chapter 1 Introduction to Electrochemistry

Chapter 2 Experimental

Chapter 3 Characterisation of Palladium Nanoparticles Decorated Graphene Oxides

Chapter 4 Hydrazine Oxidation at Glassy Carbon: Marcusian Kinetics

Chapter 5 Hydrazine Oxidation at Glassy Carbon: Self-inhibition

Chapter 6 Catalytic Hydrazine Oxidation at Palladium Nanoparticles Decorated Graphene Oxides

Chapter 7 Catalytic Hydrazine Oxidation at Bulk Palladium

Chapter 8 Catalytic Hydrazine Oxidation at Palladium Nanoparticles

Abstract

The electrochemical oxidation of hydrazine is of widespread importance particularly in the area of fuel cells and also provides the basis for chemical sensors for this toxic chemical. In this thesis, electrochemical methods including cyclic voltammetry, chronoamperometry and nano-impacts are employed to develop a comprehensive understanding of the reaction mechanistically and kinetically.

Chapter 1 introduces the basic principles of electrochemistry and electrochemical techniques while the generic chemicals, reagents and instrumentation used in this thesis are summarised in Chapter 2.

Chapter 3 reports the electrochemical characterisation of Palladium nanoparticles decorated graphene oxides nanoplatelets (Pd/GO) via nano-impacts in terms of the hydrogen evolution (HER) and oxidation reactions (HOR). The key conclusion is that only the zone of the individual platelets physically close to the electrode surface is effectively catalytic, and this insight provides the basis of the study of the Pd/GO catalytic ability towards hydrazine oxidation in Chapter 6.

The investigation into hydrazine oxidation starts in Chapter 4 where the focus is placed on the interpretation of the mechanism and kinetics of hydrazine oxidation at generic carbon surfaces, necessarily prior to any catalysis study. It was found that the Marcus-Hush theory is more appropriate for describing the voltammetry of hydrazine oxidation in comparison with the well-recognized Butler-Volmer theory.

In Chapter 5, the mechanism of hydrazine oxidation is probed further at carbon surfaces

meanwhile with focus on the variation of the pH and buffer capacity of the electrolytes. It is revealed that the oxidation reaction is self-inhibited as the protons released from the oxidation easily combines with the electro-active N_2H_4 molecules (local to the working electrode surface) to form inactive $N_2H_5^+$.

Chapter 6 targets the catalysis of the above-mentioned Pd/GO nanoplatelets towards hydrazine oxidation via studies using both macroelectrodes modified by drop-casting and by single entity electrochemistry using nano-impacts, demonstrating that the first electron transfer of the four electron, four proton oxidation of hydrazine is rate-determining and involves no proton loss in the initial step. The electro-catalysis towards hydrazine oxidation is then extended to bulk Palladium (Chapter 7) and Palladium nanoparticles (Chapter 8). Chapter 7 evidences the existence of a long-lived radical di-cation $N_2H_5^{\bullet 2+}$ on the voltammetric timescale. Finally in Chapter 8, the markedly reduced over-potential for the oxidation at the surface of Palladium nanoparticles is identified quantitatively to arise from partly the increased surface area of the interface and partly an increased catalytic ability of the nanoparticles relative to the bulk Palladium.

Acknowledgements

First and foremost, I would express my deep gratitude to my supervisor, Prof. Richard G. Compton, for his extraordinary support and inspiration throughout my DPhil. Your extreme enthusiasm upon research and persistency in electrochemical fundamentals greatly and positively influence my scientific perspective. Benefiting from your thoughtful advice and kind patience as ever, I was able to start my road of electrochemistry and overcome the obstacles along the way. You are a big man in electrochemistry and also a best supervisor I show my full respect to. Thank you.

I would also like to thank Dr. Lifu Chen for your helpful advice and on-hand guidance, as well as your company at each meeting in my first year of DPhil. Additionally, I do enjoy our quotidian chats about both research projects and life trivia.

As one of the members of ‘Compton Group 2018’, I am so lucky to experience the whole three years of DPhil together with Yuanzhe and Yanjun. I appreciate much for the companionship with both of you, and I do wish we will progress together in future as ever.

I value the cooperation with Prof. Lidong Shao, Prof. Bingsen Zhang, Dr. Minjun Yang, Dr. Pranati Nayak and Archana. Thanks to Dr. Christopher Batchelor-McAuley, Dr. Enno Kätelhön, Dr. Bertold Rasche and Dr. Hatem Amin for your professional advice. Thanks to Dr. Ruochen Xie, Dr. Alex Suherman, Dr. Korbua Chaisiwamongkhol and Dr. Haonan Le for your great help. Thanks to Yifei, Haotian, Yuanyuan, Yuqi, Raphael and Annie for your significant support.

Last but not least, I would like to thank my family for your endless love and care. You accompany with me and support me all the time. I am so lucky to have all of you!

Glossary

Roman Symbols

Symbol	Meaning	Unit
A	Electrode area	m^2
$A_{surface}$	Surface area of nanoparticles	m^2
$A_{geometric}$	Geometric area	m^2
$A_{project}$	Projected area	m^2
A_{red}	Reduction reaction frequency factor (1st order)	s^{-1}
A_{ox}	Oxidation reaction frequency factor (1st order)	s^{-1}
a	Number of protons released in the rate determining step	Dimensionless
a_i^0	Standard activity of the species i	mol dm^{-3}
c	Concentration	mol dm^{-3}
c^*	Standard concentration	mol dm^{-3}
D	Diffusion coefficient	$cm^2\ s^{-1}$
d	Diameter	m
E	Applied potential at the electrode	V
E^0	Standard electrode potential	V
E_f^0	Formal potential	V
$E_{f,eff}^0$	Effective formal potential	V
E_p	Peak potential	V
$E_{1/2}$	Midpoint potential	V

ΔE	Peak potential separation	V
F	The Faraday constant	C mol^{-1}
ΔG	Reaction Gibbs energy change	J mol^{-1}
$\Delta G^{\dagger}$	Gibbs energy of activation	J mol^{-1}
$\Delta G_0^{\dagger}$,	Standard Gibbs energy of activation	J mol^{-1}
$\Delta G_{red}^{\dagger}$	Reductive Gibbs energy of activation	J mol^{-1}
$\Delta G_{ox}^{\dagger}$	Oxidative Gibbs energy of activation	J mol^{-1}
I_p	Peak current	A
I_{red}	Reductive current	A
I_{ox}	Oxidative current	A
$I_{\lim}$	Mass transport limiting current	A
$i(t)$	Current at time t	A
$[i]$	Concentration of species i	mol dm^{-3}
$[i]_0$	Surface concentration of species i	mol dm^{-3}
J	Peak current density	A/m^2
j	Surface flux	mol cm^{-2} s^{-1}
K_{eq}	Equilibrium constant	variable
$K_{eq,eff}$	Effective equilibrium constant	variable
K_a	Dissociation constant	M
$K_{a,eff}$	Effective dissociation constant	M
k_f	Forward rate constant in equilibrium	variable
k^0	Standard rate constant	cm s^{-1}

k_{eff}^0	Effective standard rate constant	variable
k_s	Salt parameter	$dm^3\ mol^{-1}$
k_{red}	Reductive rate constant	$cm\ s^{-1}$
k_{ox}	Oxidative rate constant	$cm\ s^{-1}$
L	Layers	Dimensionless
l	Microband length	m
$m_{dropcast}$	Mass of drop-casting	g
m	Number of protons	Dimensionless
N	Number of drop-casted particles	Dimensionless
N_A	Avogadro constant	mol^{-1}
n	Number of transferred electrons	Dimensionless
R	Gas constant	$J\ K^{-1}\ mol^{-1}$
r	Radius	m
T	Absolute temperature	K
t	Time	s
$V_{dropcast}$	Volume of drop-casting	m^3
v	Potential scan rate	$V\ s^{-1}$
w	Microband width	m
Z_i	Charge of species i	Dimensionless

Greek Symbols

Symbol	Meaning	Unit
α	Cathodic transfer coefficient	Dimensionless
β	Anodic transfer coefficient	Dimensionless
ρ	Density	g m^{-3}
$\overline{\mu}_i$	Electrochemical potential of species i	J mol^{-1}
μ_i	Chemical potential of species i	J mol^{-1}
μ_i^0	Standard chemical potential of species i	J mol^{-1}
ϕ	Electrical potential	V
ϕ_M	Electrical potential of the metallic electrode	V
ϕ_S	Electrical potential of the solution	V
γ_i	Activity coefficient of the species i	Dimensionless
λ	Reorganization energy	eV
λ_i	Inner-sphere reorganization energy	eV
λ_o	Outer-sphere reorganization energy	eV
ε	Continuum of states	V
η	Dimensionless potential	Dimensionless
Λ	Dimensionless reorganization energy	Dimensionless
ψ	Roughness factor	Dimensionless

Abbreviations

Abbreviation	Meaning
aMH	asymmetric Marcus-Hush
BV	Butler-Volmer
CE	Counter Electrode
CV	Cyclic Voltammetry or Voltammogram
EDL	Electrical Double Layer
GC	Glassy Carbon
GCE	Glassy Carbon Electrode
GO	Graphene Oxide
HER	Hydrogen Evolution Reaction
HET	Heterogeneous Electron Transfer
HOR	Hydrogen Oxidation Reaction
ICP-MS	Inductively Coupled Plasma Mass Spectrometry
IHP	Inner Helmholtz Plane
MH	Marcus-Hush
MSE	Mercury Sulfate Electrode
NP	Nanoparticle
OHP	Outer Helmholtz Plane
PBS	Phosphate Buffer Solution
Pd/GO	Palladium nanoparticles decorated Graphene Oxide
RE	Reference Electrode

SCE	Saturated Calomel Electrode
SEM	Scanning Electron Microscopy
SHE	Standard Hydrogen Electrode
sMH	symmetric Marcus-Hush
TEM	Transmission Electron Macroscopy
WE	Working Electrode
XPS	X-ray Photoelectron Spectroscopy

Chapter 1

Introduction to Electrochemistry

Electrochemistry is the branch of chemistry which deals with the relation of electricity to chemical changes and the conversion between electrical and chemical energy. This chapter presents an overview of the fundamental concepts of electrochemistry and important electrochemical techniques. Topics specifically included in this chapter are the description of electrochemical equilibrium, electrode kinetics, mass transport, and electrochemical cell, as well as voltammetric and chronoamperometric techniques.

1.1 Electrochemical Equilibrium

Electrochemical equilibrium is commonly studied at the interface of an electronic conductor (electrode) and an ionic conductor (electrolyte), in terms of chemical reactions and electron transfer. Herein a metal electrode (m) immersed into a solution phase (aq) containing redox species A and B is discussed. Consider a simple one-electron transfer electrochemical equilibrium between A and B at the interface:

$$A_{(aq)} + e^{-}_{(metal)} \rightleftharpoons B_{aq} \tag{1.1}$$

At the solution-electrode interface, the established electrode potentials can be understood through the energy levels of the pertinent redox species in the potential determining equilibrium, as displayed in Figure 1.1. In regard with the electronic structure of a metal, electrons can move freely, that are delocalized, in the electronic conduction bands, in which the metal cations are bound together. The energy levels of the electrons in the conduction bands form an effective continuum of energy levels which are occupied by a finite number of electrons to an energy maximum known as the *Fermi level*. In contrast, the energy levels related to the species A and B that are solution-phase, are discrete. For the hypothetical situation ‘before electron transfer’, the electrons are assumed in Figure 1.1 to be thermodynamically favoured transferring from the Fermi level to the vacant orbital of A forming B, since the Fermi level of the electrode is higher in comparison with the lowest unoccupied molecular orbital. With the progress of the electron transfer, the Fermi level of the electrode decreases as a result of developing positive charge and simultaneously the energy levels of the solution phase increase in energy as a result of the negative charge development.[1] Once the energy levels match, the reverse reaction can happen, in which the electrons transfer from B to the metallic phase. When the forward and backward reaction rate constants match, a dynamic equilibrium is attained without further net charge. Note that the charge separation between both phases (electrode and solution), at the equilibrium, is the genesis of the *electrode potential*.

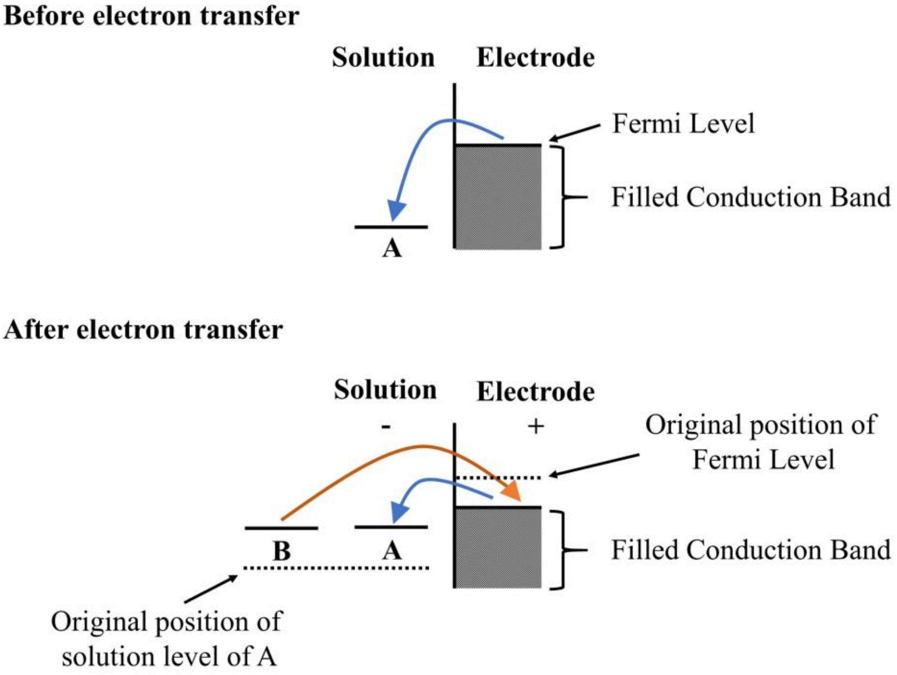

Figure 1.1. Change in the energy levels between the metallic electrode and solution-phase species.

In contrast with a *chemical* equilibrium that depends on the chemical energies of reactant and product, an *electrochemical* equilibrium is controlled by both the chemical, and electrical energies during the electron transfer between the electrode and the solution phase, as indicated below via the electrochemical potential (J mol^{-1}), $\overline{\mu}_i$, of a species i:

$$\overline{\mu}_i = \mu_i + Z_i F \phi \tag{1.2}$$

where μ_i is the chemical potential (J mol^{-1}) of i, Z_i the molecule charge of i, F Faraday constant of 96,485 C mol^{-1} and ϕ the potential (V) of the electrode (ϕ_M) or of the solution (ϕ_S) where the species i is found. Note that the first and second terms denote the contribution of the chemical and electrical energy of i, respectively. A balance between the electrochemical potentials of the reactants and products is seen at electrochemical equilibrium. Consider the equilibrium of Eq. (1.1),

$$\overline{\mu}_A + \overline{\mu}_{e^-} = \overline{\mu}_B \tag{1.3}$$

Together with Eq. (1.2),

$$\left(\mu_A + Z_A F \phi_S\right) + \left(\mu_{e^-} - F\phi_M\right) = \left[\mu_B + \left(Z_A - 1\right) F \phi_S\right] \tag{1.4}$$

Namely

$$F\left(\phi_S - \phi_M\right) = \mu_B - \mu_A - \mu_{e^-} \tag{1.5}$$

In addition, the chemical potential is expressed as[2]

$$\mu_i = \mu_i^0 + RT \ln a_i^0 \tag{1.6}$$

where μ_i^0 is the standard chemical potential, R the gas constant (J K^{-1} mol^{-1}), T the absolute temperature (K), and a_i^0 the activity of the species i in solution phase.

Therefore, Eq. (1.5) is updated with Eq. (1.6):

$$\phi_M - \phi_S = \frac{\Delta\mu^0}{F} + \frac{RT}{F} \ln\left(\frac{a_A^0}{a_B^0}\right) \tag{1.7}$$

where $\Delta\mu^0$ is a constant under certain pressure and temperature

$$\Delta\mu^0 = \mu_A^0 + \mu_{e^-} - \mu_B^0 \tag{1.8}$$

Note that Eq. (1.7) is the Nernst equation for a single interface between the solution and electrode phases.

However, it is experimentally impossible to measure an absolute value of $\phi_M - \phi_S$. Therefore, a second electrode, (for example a standard hydrogen electrode SHE, saturated calomel electrode SCE, mercury sulfate electrode MSE) is introduced into the electrochemical system, serving as a 'reference electrode'. In contrast, the first electrode is regarded as a 'working electrode'. The reference electrode has a constant value of the interfacial potential drop at its surface $\phi_M - \phi_S$ because the electrolyte concentration inside the reference electrode remains unchanged, which enables the measurement and control of the potential difference E between both electrodes. For such a two-electrode system (commonly used in potentiometric electrochemical measurements),[3]

$$E = \lim_{I \to 0}\left[\left(\phi_M - \phi_S\right)_{test} + IR - \left(\phi_M - \phi_S\right)_{reference}\right] = \left(\phi_M - \phi_S\right)_{test} + \left(\phi_M - \phi_S\right)_{reference} \tag{1.9}$$

where R is the resistivity of the electrolyte solution, and the term IR corresponding to the drop in potential in the solution phase between the two electrodes is negligible due to the very tiny current flowing.

Hence, the Nernst equation for a two-electrode system is given by[4]

$$E = E^0 + \frac{RT}{F}\ln\left(\frac{a_A^0}{a_B^0}\right) \tag{1.10}$$

where E^0 is the standard electrode potential of the redox couple A/B measured against the pertinent reference electrode. Nevertheless, the accurate value of the activity is usually unknown since it is controlled by not only the species involved in the potential determining equilibrium, but also other electrolytes around the electrode. To optimise Eq. (1.10) to a more generic and accessible form, the activity of the species is introduced:

$$a_i^0 = \gamma_i c_i \tag{1.11}$$

where γ_i is the activity coefficient of the species i and c_i is the absolute concentration of the species i.

Thus, Eq. (1.10) can be described as

$$E = E^0 + \frac{RT}{F}\ln\left(\frac{\gamma_A c_A}{\gamma_B c_B}\right) = E^0 + \frac{RT}{F}\ln\left(\frac{\gamma_A}{\gamma_B}\right) + \frac{RT}{F}\ln\left(\frac{c_A}{c_B}\right) \tag{1.12}$$

Then, the concept of the formal potential E_f^0 is introduced:

$$E_f^0 = E^0 + \frac{RT}{F}\ln\left(\frac{\gamma_A}{\gamma_B}\right) \tag{1.13}$$

so that

$$E = E_f^0 + \frac{RT}{F}\left(\frac{c_A}{c_B}\right) \tag{1.14}$$

This form of the *Nernst equation* is widely used by the experimentalists for describing the variation of the electrode potential with the species concentration in solution, with the recognition that it is only applicable to a dynamic equilibrium.

Since the pH variation in electrochemical reactions is common in practice, the expression of the Nernst equation involving pH is necessary to be deduced.

Consider an electrochemical one-electron oxidation process

$$A = B + mH^+ + e^- \tag{1.15}$$

According to Eq. (1.14),

$$E = E_f^0\left(A/B\right) + \frac{RT}{F}\ln\left(\frac{[B]\left[H^+\right]^m}{[A]}\right) = E_f^0(A/B) + \frac{RT}{F}\ln\left(\frac{[B]}{[A]}\right) + \frac{mRT}{F}\ln\left[H^+\right] \tag{1.16}$$

where $E_f^0(A/B)$ is the formal potential involving the activity coefficients of the species A and B; $[A]$, $[B]$ and $\left[H^+\right]$ are the concentrations of the species A, B and H^+, respectively; m is the number of the protons.

The definition of pH by IUPAC is

$$pH = -\log_{10}[\gamma_{H^+} H^+] \tag{1.17}$$

where γ_{H^+} is the proton activity coefficient.

Hence, Eq. (1.16) can be updated with Eq. (1.17):[5]

$$E = E_f^0(A/B) + \frac{RT}{F}\ln\left(\frac{[B]}{[A]}\right) - 2.303\frac{mRT}{F}pH \tag{1.18}$$

Notably, for a buffered media, the electro-oxidation equilibrium can be expressed as

$$A = B + e^- \tag{1.19}$$

The *effective* formal potential $E_{f,eff}^0$ corresponds to

$$E_{f,eff}^0\left(A/B\right) = E_f^0\left(A/B\right) - 2.303\frac{mRT}{F}pH \tag{1.20}$$

Hence,

$$E = E_{f,eff}^0(A/B) + \frac{RT}{F}\ln\left(\frac{[B]}{[A]}\right) \tag{1.21}$$

1.2 Electrode Kinetics

The thermodynamics interpreted above can be only employed to describe the electrochemical equilibrium state, and the deduced Nernst equation only applies to the equilibrium under ‘fast electrode kinetics’. To probe into the temporal evolution of the various species, especially in terms of the rate of chemical change and related electron transfer, the kinetics of electrode processes must be discussed.

1.2.1 Butler-Volmer Theory

Consider an electrochemical equilibrium of the one-electron transfer

$$A_{(aq)} + e^{-}_{(metal)} \underset{k_{ox}}{\overset{k_{red}}{\rightleftharpoons}} B_{aq} \tag{1.22}$$

where k_{red} and k_{ox} are the heterogenous electron transfer rate constants for the reduction and oxidation reaction, respectively, which depend on temperature and pressure and show great sensitivity to the electric potential.

The electrical current caused by the transfer and flow of electrons is given as[6, 7]

$$I = FAj \tag{1.23}$$

where A is the area of the electrode and j (mol cm^{-2} s^{-1}) is the surface flux of the heterogeneous reaction. The net rate law for the reaction is given by

$$j = j_{red} - j_{ox} = k_{red}\left[A\right]_0 - k_{ox}\left[B\right]_0 \tag{1.24}$$

where $\left[A\right]_0$ and $\left[B\right]_0$ denote the concentrations of the species A and B at the electrode surface. Note that the surface concentration usually diverges from the bulk concentration due to the formation of the diffusion layer with the passage of the electrochemical reaction around the working electrode.[8]

Then the Arrhenius equation is introduced to relate the rate constants to the Gibbs energy of activation:

$$k^0 = A_{red}\exp\left(\frac{-\Delta G_0^{\dagger}}{RT}\right) = A_{ox}\exp\left(\frac{-\Delta G_0^{\dagger}}{RT}\right) \tag{1.25}$$

$$k_{red} = A_{red}\exp\left(\frac{-\Delta G_{red}^{\dagger}}{RT}\right) \tag{1.26}$$

$$k_{ox} = A_{ox}\exp\left(\frac{-\Delta G_{ox}^{\dagger}}{RT}\right) \tag{1.27}$$

where k^0, k_{red} and k_{ox} are the standard, reductive and oxidative rate constants, respectively. A_{red} and A_{ox} are the pre-exponential factors relying on the number of reaction collision per second on the electrode surface. $\Delta G_0^\dagger$, $\Delta G_{red}^\dagger$ and $\Delta G_{ox}^\dagger$ (J mol^{-1}) are the standard, reductive and oxidative Gibbs energy of activation, respectively. The schematic diagram for the Gibbs energy varying with the reaction process is presented in Figure 1.2. The reaction coordinate starts from reactants to products, experiencing a maximum energy, namely the transition state of the reaction indicated by †.

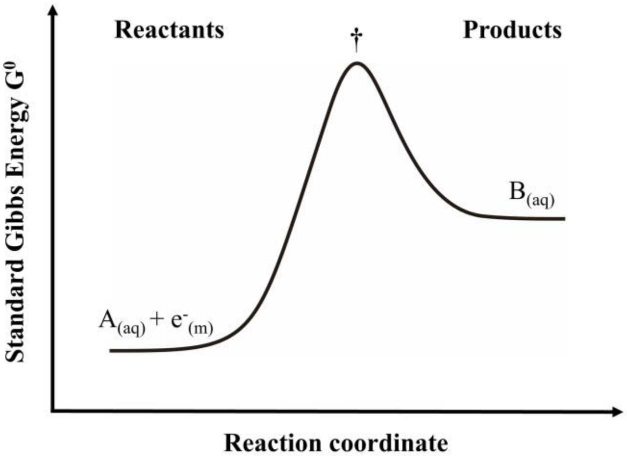

Figure 1.2. A simple electrochemical reaction profile for the electrode process.

The Gibbs energy of activation can be expressed as[9, 10]

$$\Delta G_{red}^\dagger = \Delta G_0^\dagger + \alpha F \left(E - E_f^0\right) \tag{1.28}$$

$$\Delta G_{ox}^\dagger = \Delta G_0^\dagger - \beta F \left(E - E_f^0\right) \tag{1.29}$$

where α and β are the cathodic and anodic transfer coefficients, respectively; E is the applied potential and E_f^0 is the formal potential as indicated in Eq. (1.13). In terms of a one-electron transfer reaction, the transfer coefficients vary from 0 to 1, and follow the relationship

$$\alpha + \beta = 1 \tag{1.30}$$

As α is close to 0, the transition state is *reactant-like*, whereas as α approaches unity, the state is *product-like*.[11, 12] In practice, the transfer coefficients usually locate at 0.5 suggesting the similarity in the electrical behaviour between the reactants and products.

$$\alpha \sim \beta \sim 0.5 \tag{1.31}$$

Rearrange Eq. (1.25) ~ (1.29) and then give

$$k_{red} = k^0 \exp\left(-\frac{\alpha F(E - E_f^0)}{RT} \right) \tag{1.32}$$

$$k_{ox} = k^0 \exp\left(\frac{\beta F(E - E_f^0)}{RT} \right) \tag{1.33}$$

Eq. (1.32) and (1.33) are the well-recognized Butler-Volmer forms for the electrochemical rate constants, where $(E - E_f^0)$ denotes the potential applied at the working electrode relative to the formal potential of the reference electrode, known as *overpotential.*

Then substituting Eq. (1.32) and (1.33) with Eq. (1.24),

$$j = k^0 \left[A\right]_0 \exp\left(-\frac{\alpha F(E - E_f^0)}{RT} \right) - k^0 \left[B\right]_0 \exp\left(\frac{\beta F(E - E_f^0)}{RT} \right) \tag{1.34}$$

Under extreme potentials, one of the terms in Eq. (1.34) can be neglected to give

for a reduction reaction,

$$j = k^0 \left[A\right]_0 \exp\left(-\frac{\alpha F(E - E_f^0)}{RT} \right) \tag{1.35}$$

and for an oxidation reaction,

$$j = k^0 \left[B\right]_0 \exp\left(\frac{\beta F(E - E_f^0)}{RT} \right) \tag{1.36}$$

If the analyte concentration around the working electrode is close to the bulk concentration:

$$\ln\left|I_{red}\right| = -\frac{\alpha FE}{RT} + constant \tag{1.37}$$

$$\ln\left|I_{ox}\right| = \frac{\beta FE}{RT} + constant \tag{1.38}$$

where I_{red} and I_{ox} are the reductive and oxidative currents, respectively. The well-known

Tafel plot is exactly the plot of $\ln|I_{red}|$ vs E or $\ln|I_{ox}|$ vs E, from which the value of the anodic or cathodic transfer coefficient can be extracted[9, 13]:

$$\alpha = -\frac{RT}{F}\frac{\partial \ln|I_{red}|}{\partial E} \tag{1.39}$$

$$\beta = \frac{RT}{F}\frac{\partial \ln|I_{ox}|}{\partial E} \tag{1.40}$$

Note that the accurate estimation requires the consistency between the analyte concentration around the working electrode with the bulk concentration over the potential range studied.

1.2.2 Marcus-Hush Theory

In the 1950s, Marcus[14] developed his famous microscopic model for the analysis of electron transfer kinetics in outer-sphere homogeneous reactions, where the molecular nature of the system was characterized in terms of the reorganization energy (λ) and the reaction Gibbs energy change (ΔG). The reorganization energy is defined as the Gibbs energy required to distort the atomic positions of the reactant molecule and its solvation shell to those of the product in its relaxed nuclear configuration.[15] It reflects the intramolecular vibrations leading to changes in bond lengths and angles (the inner-sphere reorganization energy, λ_i) as well as the changes in the polarization of solvent molecules (the outer-sphere reorganization energy, λ_o).

The Marcus theory was simultaneously developed and then extended by Hush especially from a chemical perspective[16, 17], whilst in the 1990s, Chidsey's work[18] clarified the symmetry and thermodynamic consistency of the Marcus-Hush model, conditional on the metal electrode having a continuum of electronic states. Thus, the well-known symmetric Marcus-Hush (sMH) model was established and widely employed, assuming the Gibbs energy parabolae of the reductants and oxidants to have equal curvature. The Gibbs energy versus reaction profile[19] is presented in Figure 1.3.

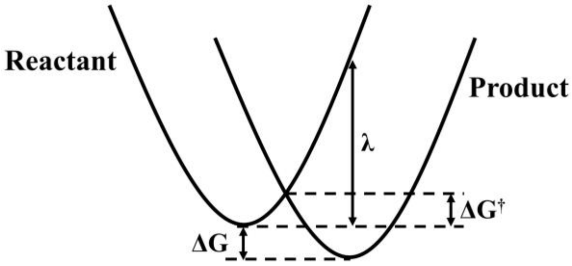

Figure 1.3. Gibbs energy reaction coordinate diagram for the reactant and product.

On this basis the Gibbs energy of activation, $\Delta G^{\dagger}$ is given by:

$$\Delta G^{\dagger} = \frac{\left(\lambda + \Delta G\right)^2}{4\lambda} \tag{1.41}$$

The electrons in the electrode are thought to form a continuum of states (ε) in the heterogeneous electron transfer reactions in accordance with the Fermi-Dirac distribution. The electrochemical rate constants based on sMH (k_{red}^{MH} , k_{ox}^{MH}) are given by:

$$k_{red}^{MH} = k_0 \frac{S_{red}\left(\eta, \Lambda\right)}{S_{red}\left(0, \Lambda\right)} \tag{1.42}$$

$$k_{ox}^{MH} = k_0 \frac{S_{ox}\left(\eta, \Lambda\right)}{S_{ox}\left(0, \Lambda\right)} \tag{1.43}$$

where $k_{red/ox}^{MH}$ is dependent on the standard rate constant k_0, the dimensionless potential η as well as the dimensionless reorganization energy Λ, and $S_{red/ox}\left(\eta, \Lambda\right)$ are integrals:

$$S_{red/ox}\left(\eta, \Lambda\right) = \int_{-\infty}^{+\infty} \frac{\exp\left[-\Delta G_{sym,red/ox}^{\dagger}\left(x\right) / RT\right]}{1 + \exp\left(\mp x\right)} dx \tag{1.44}$$

and where $\Delta G_{sym,red/ox}^{\dagger}\left(x\right)$ is the activation Gibbs energy of the electro-reduction/oxidation process for each electronic level:

$$\frac{-\Delta G_{sym,red/ox}^{\dagger}(x)}{RT} = \frac{\Lambda}{4}\left(1 \pm \frac{\eta + x}{\Lambda}\right)^2 \tag{1.45}$$

where

$$\eta = \frac{F}{RT}\left(E - E_f^0\right) \quad (1.46)$$

$$x = \frac{F}{RT}\left(\varepsilon - E\right) \quad (1.47)$$

$$\Lambda = \frac{F}{RT}\lambda \quad (1.48)$$

The upper sign in $\mp$ or $\pm$ involved in the above formulas refers to reduction, while the lower one refers to oxidation.

The sMH model, unlike the BV theory, predicts a potential dependence of the transfer coefficient leading to curved Tafel plots[20-22]. The predictions can be linked to the BV theory as follows. From the analysis of the electrochemically irreversible Butler-Volmer kinetics for an oxidation process,

$$\beta = \frac{RT}{F}\frac{\partial \ln\left|I_{ox}\right|}{\partial E} = \frac{RT}{F}\frac{\partial \ln\left|k_{ox}^{BV}\right|}{\partial E} \quad (1.49)$$

where according to the Arrhenius equation,

$$k_{ox}^{BV} = A\exp\left(-\frac{\Delta G^{\dagger}}{RT}\right) \quad (1.50)$$

in which A is the pre-exponential factor.

Together with Eq. (1.41), the link between Butler-Volmer kinetics and symmetric Marcus-Hush theory is given by:

$$\beta = \frac{1}{2}\left(1 + \frac{\Delta G}{\lambda}\right) \quad (1.51)$$

where for the electrode process,

$$\Delta G = -F\left(E - E_f^0\right) \quad (1.52)$$

Hence,

$$\beta = \frac{\lambda + FE_f^0}{2\lambda} - \frac{F}{2\lambda}E \quad (1.53)$$

This relationship in principle enables the extraction of values for λ and E_f^0 from experimental voltammograms[23]. Note that Eq. (1.51) is derived assuming the symmetric form of the MH theory which is reflected in the limiting value of 0.5 for the transfer coefficient as the reorganization energy increases to a large value or when $E = E_f^0$.

Hitherto, numerous systems have been successfully interpreted by the sMH model[18, 24-26] and surface bound couples in particular. The application for solution phase processes is more limited largely since diffusional effects take over with increasing over-potential before significant Marcusian behaviour becomes apparent. Accordingly the difference between sMH and BV theory is not great although often BV gives a slightly better fit with experiment[27-30]. However if the assumption that the reactant and product Gibbs energy parabolae have the same curvature is relaxed - leading to asymmetric MH (aMH) theory then the superiority of the latter is apparent[31, 32].

1.3 Mass Transport

The electrode kinetics at the interface of the electrode and solution phase have been discussed above, under the assumption that the analyte concentration around the electrode is constant. However, in reality, consumption of reactants and formation of products on or around the working electrode always results in the movement of the reactants from bulk to the electrode surface and that of the products away from the electrode surface. This phenomenon in the study of the electrochemical equilibrium is *mass transport*. Mass transport is attributed to three main processes (diffusion, convection and migration) in solution phase.

1.3.1 Diffusion

Diffusion is the net movement of a species from high to low concentration and driven by the concentration gradient, following Fick's 1st law

$$j = -D\frac{\partial c}{\partial x} \tag{1.54}$$

where j is the number of moles of a species passing through unit area per second, known as *flux* (mol cm^{-2} s^{-1}), D the diffusion coefficient of the species (cm^{2} s^{-1}) and $\frac{\partial c}{\partial x}$ the local concentration gradient at point x.

A schematic reactant concentration profile against the distance from the electrode surface where the Nernst diffusion layer is indicated, is presented in Figure 1.4. The diffusion layer comprises the zone of reactant depletion around the electrode.

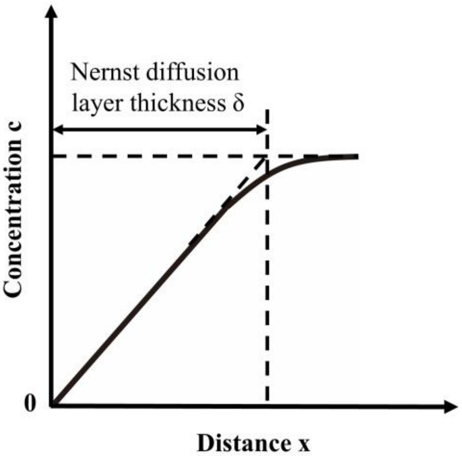

Figure 1.4. Nernst diffusion layer.

Using Fick's 1st law together with conservation of mass, Fick's 2nd law considering the variation of concentration as a function of distance and time can be derived for a point x:

$$\frac{\partial c}{\partial t} = D\frac{\partial^2 c}{\partial x^2} \tag{1.55}$$

where t is the time.

Complementary to Fick's Laws the Einstein-Smoluchowski equation[33-35] can be derived based on the random motion of molecules and/or particles to give the root mean square displacement in time t, enabling the approximate measurement of the diffusion layer thickness in practice:

$$\sqrt{\langle x^2 \rangle} = \sqrt{2Dt} \tag{1.56}$$

Furthermore, in three dimensions, Eq. (1.55) is expanded to

$$\frac{\partial c}{\partial t} = D\left(\frac{\partial^2 c}{\partial x^2} + \frac{\partial^2 c}{\partial y^2} + \frac{\partial^2 c}{\partial z^2}\right) \tag{1.57}$$

The root mean square distance becomes

$$\sqrt{\langle x^2 \rangle + \langle y^2 \rangle + \langle z^2 \rangle} = \sqrt{6Dt} \tag{1.58}$$

1.3.2 Convection

Convection is the hydrodynamic transport of species with two forms (natural and forced).[36, 37] Natural convection is controlled by density gradients such that the movement of the species is down the gradient, namely from the dense to the less dense regions. This always occurs around the surface of working or/and counter electrodes due to the reactant consumption and product formation. Additionally, thermal variations also exert an effect on the density gradient. For instance, the heat produced from chemical reactions as well as imperfect thermostatting may result in the deviation of the local density from that of the bulk solution. Note that the high irreproducibility of the natural convection is likely to lower the experimental precision. Hence, usually a short time of the electrochemical measurement is preferred so to diminish its influence. The other convection is forced convection which originates from the mechanical agitation usually via solution stirring, electrode rotation, gas bubbling, etc. The higher controllability of forced convection enables us to effectively alter the rates of mass transport to better facilitate quantitative analysis.

1.3.3 Migration

As discussed in the Section 1.1, there is an electric field formed due to the potential drop at the electrode/solution interface, which facilitates the movement of charged species in solution. This transport phenomenon is called *migration*. The migratory flux, $j_{m,i}$ at point x for any species i is expressed as

$$j_{m,i}(x) = -\frac{z_i F}{RT} D_i c_i \frac{\partial \phi(x)}{\partial x} \tag{1.59}$$

where z_i is the ionic charge, D_i the diffusion coefficient, c_i the concentration and $\frac{\partial \phi(x)}{\partial x}$ is the gradient of the electrical potential or electric field.

Owing to the significant influence of migration on electrochemical systems, an electrolyte with high concentration (in comparison with that of the electro-active species) is necessarily employed to restrict the electrical differences between ions in different locations and simultaneously lower the ohmic drop, so to eliminate the migration. Under the circumstances of high support, the interfacial potential drop can be confined to a very small region to the electrode, giving rise to a very thin *electrical double layer* (EDL) with respect to the diffusion layer. Note that the double layer where the decay of the potential is rapid is comprised of a layer of specifically adsorbed species (Inner Helmholtz Plane IHP), and another of non-specifically adsorbed species (Outer Helmholtz Plane OHP). Beyond this layer is the diffuse layer) where an excess of ions of opposite charge to the electrode are present but where the thermal forces exceed the electrostatic forces of attraction so that the ions are free to move.[38]

1.4 Electrochemical Cells

In electrochemical experiments, a three-electrode system[39] is usually employed to study the reaction and its kinetics, as illustrated in Figure 1.5 (left). The electrochemical cell consists of three electrodes: a working electrode (WE) where the reaction of interest occurs; a reference electrode (RE) that provides a stable control value for measuring and controlling the potential drop at the working electrode/solution interface; a counter electrode (CE) from which the current passes instead of the reference electrode in order to avoid the chemical change inside the reference electrode.

The three-electrode system is controlled by a *potentiostat* as indicated in Figure 1.5 (right). The potentiostat applies a constant potential, E, between the working electrode and reference electrode, but without currents flowing through the latter as facilitated by the presence of the counter electrode. As described in Eq. (1.60), the reference electrode provides a constant value of $\left(\phi_M - \phi_S\right)_{RE}$, so any changes in the applied potential E can be achieved in $\left(\phi_M - \phi_S\right)_{WE}$ of the working electrode.

$$E = \left(\phi_M - \phi_S\right)_{WE} + IR - \left(\phi_M - \phi_S\right)_{RE} \tag{1.60}$$

Meanwhile, the current caused by the potential change can be recorded by the amperemeter. Therefore, this allows the real-time monitor on the variation of I with E from which the reaction information including mechanism and kinetics is extracted.

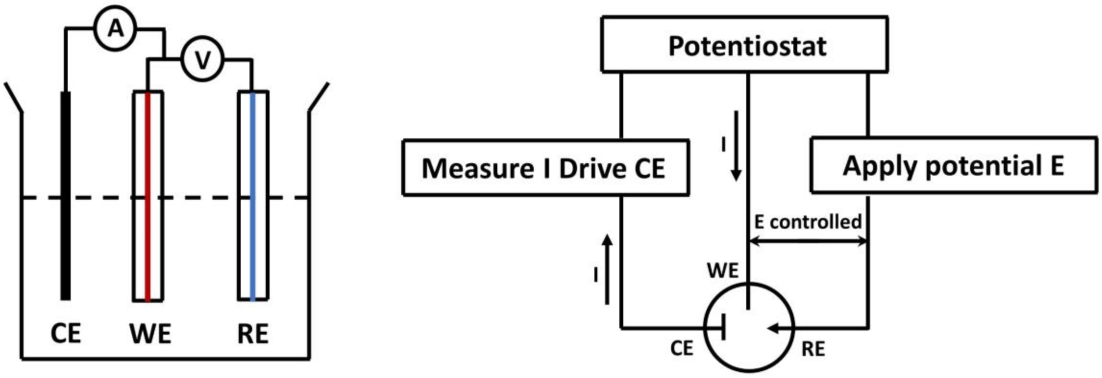

Figure 1.5. Schematic diagram of an electrochemical cell with a three-electrode system.

1.5 Electrochemical Techniques

This section introduces some of the electrochemical techniques available to electrochemists to measure the mechanistic, kinetic and thermodynamic data related to electrode processes, including cyclic voltammetry, chronoamperometry and nano-impacts.

1.5.1 Cyclic Voltammetry

Cyclic voltammetry (CV) is widely employed to measure the current response of the electrochemical reaction of interest in solution, which is conducted through a linearly cycled potential sweeping within set potential ranges at a constant scan rate, v (V s^{-1}).[40] The sweep usually starts at a potential E_1 where there are no Faradaic (oxidative or reductive) currents, and arrives at a vertex potential E_2 where the reaction is fully driven, and then the scan reverses to the initial potential E_1, to complete a full cycle. The nominally 'linear' potential sweep is actually not linear but consists of multiple tiny potential steps, or staircases imposed digitally, as indicated in Figure 1.6. The currents measured at certain position of each potential steps create a close approximation to linear sweep voltammetry. The plot of the current response with the variation of the applied potential is the *cyclic voltammogram*.

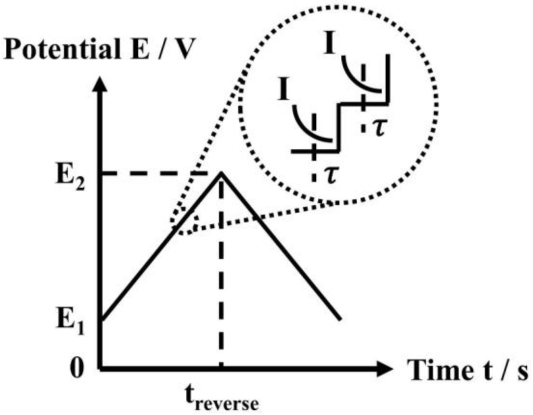

Figure 1.6. Potential sweep of staircase cyclic voltammetry.

1.5.2 Chronoamperometry

Chronoamperometry is popular for electrochemical analysis, which is conducted by stepping the potential from E_1 where usually no Faradaic reactions occur to E_2 where the electrolysis of interest proceeds, as shown in Figure 1.7A. Commonly E_2 is expected to provide a sufficient overpotential so that the reactant diffusing to the electrode surface can be fully consumed. Since the reaction is not induced at the potential E_1, the current is zero or close to zero. However, following the potential step to E_2, a significant current response can be instantly observed from the oxidation or reduction of an electro-active species if present at sufficient concentration. Then with time, the current gradually decays to zero (for macroelectrode where the transport is controlled by linear diffusion) or a steady-state value (for microelectrode where there is convergent diffusion) on account of the consumption of the reactant in the vicinity of the electrode surface, as illustrated in Figure 1.7B and C.[1]

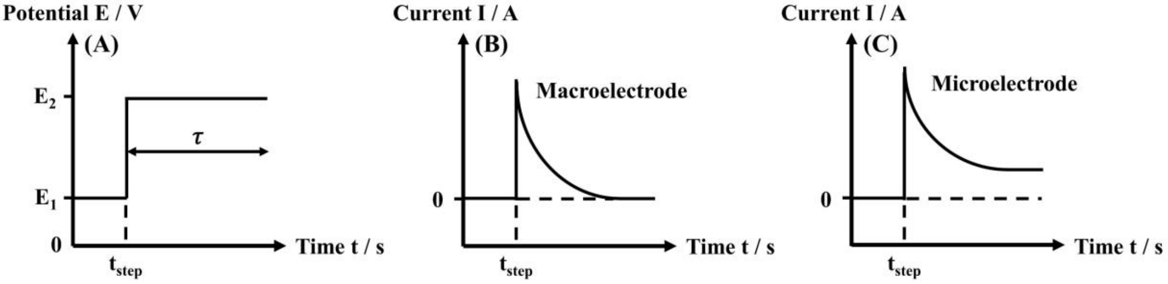

Figure 1.7. (A) Potential profile with time for a single-step chronoamperometry. The chronoamperometric current at (B) a macroelectrode and (C) a microelectrode.

1.5.3 Nano-impacts

In recent years, nanomaterials (defined as having at least one dimension in the range of 1 - 100 nm) have received extensive attention, and contributed to advances in diverse areas including catalysis[41], sensors[42], fuel cells[43], and medicine[44]. In practice, most electrochemical studies in these areas are conducted based on ensembles of the nanomaterials, the voltammetric responses of which actually reflect not only chemical and physical characteristics of single entities, but also the special structure or morphology with porosity, orientation or agglomeration formed by their interaction and stacking within the ensemble. This significantly increases the difficulty in the identification upon what features of the nanomaterials are functioning on the electrochemical reactions. Hence, an electrochemical technique specially for investigating the nanomaterials from the perspective of single entity is essential.

Nano-impacts, or impact electrochemistry, has been rapidly developed recently to detect and characterise individual nanoparticles (NPs), as well as extract the kinetics of associated electrochemical reactions.[45-47] This technique is conducted by detecting the (Faradaic or non-Faradaic) current response from the random collision of well-dispersed single nanoparticles (via Brownian motion in solution) onto the working microelectrode. Note that the concentration of the nanoparticle suspension is critical. It cannot be too high otherwise particle aggregation may occur but also it must not be too low as this results in a very low collision frequency and impact experiments take an unfeasibly long time.

There are commonly several classes of impact collisions as illustrated in Figure 1.8. Figure 1.8 (A) shows that in *direct* nano-impacts the individual nanoparticle following the collision is immediately oxidised (or reduced) at/close to the electrode surface during the chronoamperometric measurements, whereas Figure 1.8B illustrates the *mediated* nano-impacts where the individual nanoparticles serve as an electro-catalyst towards the oxidation (reduction) of the species A to B. Furthermore, for mediated catalysis, the impact of short residence time, namely that the impacting nanoparticle leaves the electrode surface soon, usually gives a sharp current signal (named *spike*), while the contrary that the nanoparticle sticks or absorbs to the surface produces a stable steady-state current (named *step*). In addition to the two common impacts inducing the redox reactions, there is also capacitive (non-Faradaic) impacts originating from the displacement of charge from the electrode/surface interface or the charging of the impacting nanoparticle. Provided that the working electrode is applied with a potential that is not equal to the zero charge potential, oxidative or reductive current responses due to ionic motion and double layer charging may be observed during the impact.[48] Note that impacts experiments are usually performed at a microelectrode, not a macroelectrode, since the impacting-induced current signals are easily overwhelmed by the background capacitance of the macroelectrode. Moreover the relatively huge surface area of the macroelectrode in comparison with the size of nanoparticles easily results in abundant simultaneous impacts onto the electrode surface with the result that the current spikes or steps are likely to overlap.

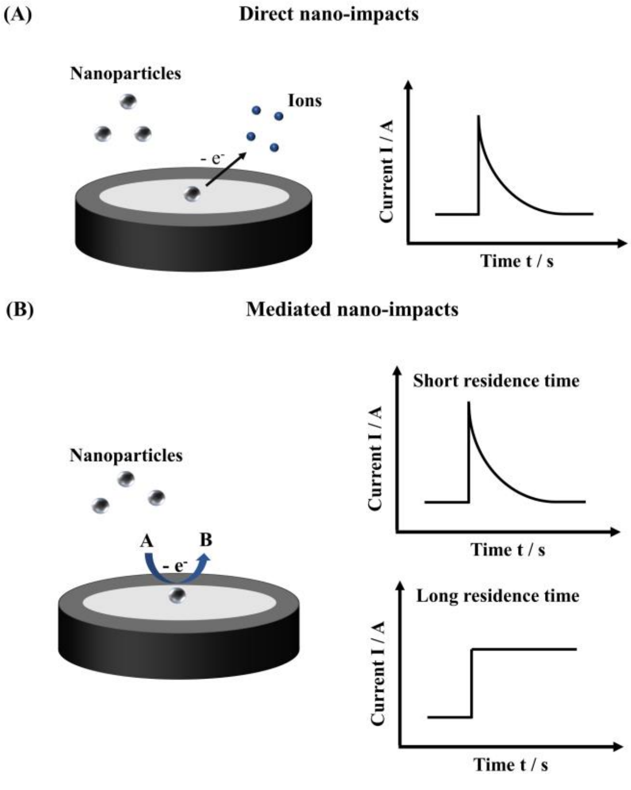

Figure 1.8. Diagrams of nano-impacts and related current responses: (A) direct nano-impacts and (B) mediated nano-impacts of short and long residence time.

References

[1] R.G. Compton, C.E. Banks, Understanding Voltammetry, World Scientific, 2018.

[2] A. Arevalo, G. Pastor, Verification of the Nernst equation and determination of a standard electrode potential, J. Chem. Educ., 62 (1985) 882.

[3] F.J. Vidal-Iglesias, J. Solla-Gullón, E. Herrero, A. Rodes, A. Aldaz, Do you really understand the electrochemical Nernst equation?, Electrocatalysis, 4 (2013) 1-9.

[4] F.J. Vidal-Iglesias, J. Solla-Gullón, A. Rodes, E. Herrero, A. Aldaz, Understanding the Nernst equation and other electrochemical concepts: an easy experimental approach for students, J. Chem. Educ., 89 (2012) 936-939.

[5] M.M. Walczak, D.A. Dryer, D.D. Jacobson, M.G. Foss, N.T. Flynn, pH dependent redox couple: An illustration of the Nernst equation, J. Chem. Educ., 74 (1997) 1195.

[6] M.C. Henstridge, R.G. Compton, Direct extraction of kinetic parameters from experimental cyclic voltammetry, J. Electroanal. Chem., 681 (2012) 109-112.

[7] J.L. Melville, R.G. Compton, The simulation of differential pulse voltammetry, Electroanalysis, 13 (2001) 123-130.

[8] V.S. Bagotsky, Fundamentals of Electrochemistry, John Wiley & Sons, 2005.

[9] R. Guidelli, R.G. Compton, J.M. Feliu, E. Gileadi, J. Lipkowski, W. Schmickler, S. Trasatti, Defining the transfer coefficient in electrochemistry: An assessment (IUPAC Technical Report), Pure Appl. Chem., 86 (2014) 245-258.

[10] J.C.R. Reis, Thermodynamic analysis of the symmetry factor and the transfer coefficient in electrode kinetics, J. Electrochem. Soc., 144 (1997) 2404.

[11] F. Bordwell, W. Boyle Jr, Acidities, Broensted coefficients, and transition state structures for 1-arylnitroalkanes, J. Am. Chem. Soc., 94 (1972) 3907-3911.

[12] S.J. Formosinho, Theoretical studies of proton-transfer reactions, J. Chem. Soc., Perkin trans. 2, (1987) 61-66.

[13] G. Kear, F.C. Walsh, The characteristics of a true Tafel slope, Corros. Mater., 30 (2005) 51-55.

[14] R.A. Marcus, On the theory of oxidation-reduction reactions involving electron transfer. I, J. Chem. Phys., 24 (1956) 966-978.

[15] L. Eberson, R. Gonzalez-Luque, J. Lorentzon, M. Merchan, B.O. Roos, The ab initio calculation of inner sphere reorganization energies of inorganic redox couples, J. Am. Chem. Soc., 115 (1993) 2898-2902.

[16] N. Hush, Adiabatic rate processes at electrodes. I. Energy-charge relationships, J. Chem. Phys., 28 (1958) 962-972.

[17] N. Hush, Electron transfer in retrospect and prospect: 1: Adiabatic electrode processes, J. Electroanal. Chem., 460 (1999) 5-29.

[18] C.E. Chidsey, Free energy and temperature dependence of electron transfer at the metal-electrolyte interface, Science, 251 (1991) 919-922.

[19] E. Laborda, M.C. Henstridge, C. Batchelor-McAuley, R.G. Compton, Asymmetric Marcus–Hush theory for voltammetry, Chem. Soc. Rev., 42 (2013) 4894-4905.

[20] A.J. Appleby, J.H. Zagal, Free energy relationships in electrochemistry: a history that started in 1935, J. Solid State Electrochem., 15 (2011) 1811-1832.

[21] P. Bai, M.Z. Bazant, Charge transfer kinetics at the solid–solid interface in porous electrodes, Nat. Commun., 5 (2014) 1-7.

[22] E. Laborda, M.C. Henstridge, R.G. Compton, Giving physical insight into the Butler–Volmer model of electrode kinetics: Part 2-Nonlinear solvation effects on the voltammetry of heterogeneous electron transfer processes, J. Electroanal. Chem., 681 (2012) 96-102.

[23] J.-M. Savéant, Elements of molecular and biomolecular electrochemistry, Willey-VCH, New Jersey, (2006).

[24] R.J. Forster, L.R. Faulkner, Electrochemistry of spontaneously adsorbed monolayers. Equilibrium properties and fundamental electron transfer characteristics, J. Am. Chem. Soc., 116 (1994) 5444-5452.

[25] N. Madhiri, H.O. Finklea, Potential-, pH-, and isotope-dependence of proton-coupled electron transfer of an osmium aquo complex attached to an electrode, Langmuir, 22 (2006) 10643-10651.

[26] B.R. Kozub, M.C. Henstridge, C. Batchelor-McAuley, R.G. Compton, Edge Plane Pyrolytic Graphite Electrode Covalently Modified with 2-Anthraquinonyl Groups: Theory and Experiment, Chemphyschem, 12 (2011) 2806-2815.

[27] M.C. Henstridge, Y. Wang, J.G. Limon-Petersen, E. Laborda, R.G. Compton, An experimental comparison of the Marcus–Hush and Butler–Volmer descriptions of electrode kinetics applied to cyclic voltammetry. The one electron reductions of europium (III) and 2-methyl-2-nitropropane studied at a mercury microhemisphere electrode, Chem. Phys. Lett., 517 (2011) 29-35.

[28] E. Laborda, Y. Wang, M.C. Henstridge, F. Martínez-Ortiz, A. Molina, R.G. Compton, Quantitative weaknesses of the Marcus-Hush theory of electrode kinetics revealed by Reverse Scan Square Wave Voltammetry: The reduction of 2-methyl-2-nitropropane at mercury microelectrodes, Chem. Phys. Lett., 512 (2011) 133-137.

[29] M.C. Henstridge, E. Laborda, E.J. Dickinson, R.G. Compton, Redox systems obeying Marcus–Hush–Chidsey electrode kinetics do not obey the Randles–Ševčík equation for linear sweep voltammetry, J. Electroanal. Chem., 664 (2012) 73-79.

[30] D. Suwatchara, N.V. Rees, M.C. Henstridge, E. Laborda, R.G. Compton, Experimental comparison of the Butler–Volmer and Marcus–Hush–Chidsey formalisms of electrode kinetics: The reduction of cyclooctatetraene at mercury hemispherical electrodes via cyclic and square wave voltammetries, J. Electroanal. Chem., 665 (2012) 38-44.

[31] E. Laborda, M.C. Henstridge, R.G. Compton, Asymmetric Marcus theory: Application to electrode kinetics, J. Electroanal. Chem., 667 (2012) 48-53.

[32] Y. Zeng, P. Bai, R.B. Smith, M.Z. Bazant, Simple formula for asymmetric Marcus–Hush kinetics, J. Electroanal. Chem., 748 (2015) 52-57.

[33] M. Islam, Einstein–Smoluchowski diffusion equation: a discussion, Phys. Scr., 70 (2004) 120.

[34] A. Einstein, Über die von der molekularkinetischen Theorie der Wärme geforderte Bewegung von in ruhenden Flüssigkeiten suspendierten Teilchen, Ann. Phys., 4 (1905).

[35] M. Von Smoluchowski, Zur kinetischen theorie der brownschen molekularbewegung und der suspensionen, Ann. Phys., 326 (1906) 756-780.

[36] J.K. Novev, R.G. Compton, Natural convection effects in electrochemical systems, Curr. Opin. Electrochem., 7 (2018) 118-129.

[37] J. Rubio-Garcia, A. Kucernak, A. Charleson, Direct visualization of reactant transport in forced convection electrochemical cells and its application to redox flow batteries, Electrochem. Commun., 93 (2018) 128-132.

[38] J. Lück, A. Latz, Modeling of the electrochemical double layer and its impact on intercalation reactions, Phys. Chem. Chem. Phys., 20 (2018) 27804-27821.

[39] D. Pletcher, R. Greff, R. Peat, L. Peter, J. Robinson, Instrumental Methods in Electrochemistry, Woodhead Publishing, 2001.

[40] A.J. Bard, L.R. Faulkner, Electrochemical Methods: Fundamentals and Applications, Wiley, 2001.

[41] S. Chaturvedi, P.N. Dave, N. Shah, Applications of nano-catalyst in new era, J. Saudi Chem. Soc., 16 (2012) 307-325.

[42] G. Maduraiveeran, W. Jin, Nanomaterials based electrochemical sensor and biosensor platforms for environmental applications, Trends Environ. Anal. Chem., 13 (2017) 10-23.

[43] S. Guo, E. Wang, Noble metal nanomaterials: controllable synthesis and application in fuel cells and analytical sensors, Nano Today, 6 (2011) 240-264.

[44] A.M. Wen, N.F. Steinmetz, Design of virus-based nanomaterials for medicine, biotechnology, and energy, Chem. Soc. Rev., 45 (2016) 4074-4126.

[45] W. Cheng, R.G. Compton, Electrochemical detection of nanoparticles by 'nano-impact'methods, Trends Anal. Chem., 58 (2014) 79-89.

[46] M. Pumera, Impact electrochemistry: measuring individual nanoparticles, ACS Nano, 8 (2014) 7555-7558.

[47] L.K. Allerston, N.V. Rees, Nanoparticle impacts in innovative electrochemistry, Curr. Opin. Electrochem., 10 (2018) 31-36.

[48] S.V. Sokolov, S. Eloul, E. Kätelhön, C. Batchelor-McAuley, R.G. Compton, Electrode-particle impacts: a user's guide, Phys. Chem. Chem. Phys., 19 (2017) 28-43.

Chapter 2

Experimental

This chapter introduces the general experimental details reported in this thesis including chemical reagents, materials and instrumentation. Specific descriptions of each experiment can be found in the Experimental sections of Chapters 3-8.

2.1 Chemical and Reagents

All chemicals and reagents involved in the experiments reported in this thesis are listed in Table 2.1, and were used without further purification. All solutions were prepared with deionised water (of resistivity 18.2 MΩ cm, Millipore, 25 °C).

Table 2.1 List of chemicals, reagents and materials mentioned in this thesis

Chemical	Formula	Purity	Supplier
Potassium nitrate	KNO_3	99.99%	Sigma-Aldrich
Potassium mono-hydrogen phosphate	K_2HPO_4	98%	Sigma-Aldrich
Potassium di-hydrogen phosphate	KH_2PO_4	99%	Sigma-Aldrich
Potassium chloride	KCl	99%	Sigma-Aldrich
Potassium hydroxide	KOH	85%	Sigma-Aldrich
Nitric acid	HNO_3	70%	Sigma-Aldrich
Hydrazine hydrate	$N_2H_4\cdot xH_2O$	98%	Sigma-Aldrich
Palladium nitrate	$Pd(NO_3)_2$	10% Pd	Sigma-Aldrich
Palladium nanoparticles (Pd NPs)	Pd	99.5%	Sigma-Aldrich
Hydrogen	H_2	99.99%	BOC
Nitrogen	N_2	99.99%	BOC
Helium	He	99.99%	BOC
Palladium nanoparticles decorated graphene oxides (Pd/GO)	/	/	Synthesis

The Pd/GO platelets were prepared via a procedure similar to that reported in a previous study[1] and the synthetic details are as follows. 400 mg graphite oxide synthesized via the Hummers method[2] was dispersed in 800 mL distilled water and sonicated for 2 hours. 240μL Palladium nitrate was dissolved in 10 mL distilled water and mixed with the dispersion of graphite oxide. Then the mixed solution was sonicated for 0.5 hour and desiccated by lyophilisation. Subsequently, heating was applied under vacuum at 500°C for 0.5 hour. Finally, heating was conducted under a H_2/He atmosphere for the reduction treatment at 250°C for 1 hour to obtain the final product Pd/GO. Note that the Pd/GO materials were synthesized and provided by Prof. Lidong Shao (Shanghai University of Electric Power). The C/O ratio by atom was measured to be ca. 8 obtained by X-ray Photoelectron Spectroscopy (XPS) as reported previously.[1] The prepared Pd/GOs were characterized via Transmission Electron Macroscopy (TEM, FEI Tecnai G2 F20). The weight loading of Pd was measured via Inductively Coupled Plasma Mass Spectrometry (ICP-MS). The size distribution and surface density of Pd were determined by the software ImageJ (The National Institute of Health, USA). Note that the TEM images were provided by Prof. Bingsen Zhang (Chinese Academy of Sciences, Shenyang).

2.2 Electrochemical Instrumentation

All voltammetric measurements were conducted in a Faraday cage (thermostated at 298 ± 0.5 K) using a μAutolab II potentiostat (Metrohm Ltd., Utrecht, NL). A standard three-electrode configuration was employed: a saturated calomel electrode (SCE, BASI Ltd., Japan) as the reference electrode; a graphite rod as the counter electrode; a macrodisc electrode as the working electrode including a Pd macrodisc (3 mm in diameter, Sigma-Aldrich Ltd., UK), a glassy carbon (GC) macrodisc (3 mm in diameter, BASI Ltd., Japan), Palladium nanoparticle modified GC macrodiscs, Pd/GO modified GC macrodiscs or home-fabricated carbon fibre microelectrodes (7 μm in diameter, ca. 1 mm length)[3].

2.2.1 Preparation of Macrodisc Electrodes

Prior to electrode surface modification (drop-casting) and all electrochemical measurements, the abovementioned Palladium and glassy carbon macrodisc electrodes were mechanically polished with alumina slurries of decreasing particle sizes of 1.0, 0.3 and 0.05 μm (Buehler Ltd., Illinois, USA) on soft lapping pads (Kemet Ltd., Kent, UK), followed with a water rinse, sonication and drying with nitrogen. The details of drop-casting onto the polished electrode vary from system to system are given in the relevant chapters.

2.2.2 Fabrication of Carbon Fibre Microelectrodes

The carbon fibre microelectrodes were home-made according to the method proposed by Ellison et al.[3] A carbon fibre with a diameter of 7 μm (GoodFellow Ltd., Huntingdon, UK) was connected to a conducting metal wire via the adhesive from the mixture of silver expoxy and the hardener (RS Components Ltd., UK), followed by a 15-min heating in the oven at ca. 60 °C. The connection was then threaded through a plastic pipette tip with only the carbon fibre out of the tip. The cyanoacrylate adhesive was subsequently employed to seal the interstice between the carbon fibre and tip. The fabricated electrode was left overnight for the adhesive drying. Lastly, the carbon fibre of the dried electrode was usually cut to the length of ca. 1 mm, and calibrated by the voltammetric experiments using a simple redox reactions.

References

[1] L. Shao, X. Huang, D. Teschner, W. Zhang, Gold supported on graphene oxide: an active and selective catalyst for phenylacetylene hydrogenations at low temperatures, ACS Catalysis, 4 (2014) 2369-2373.

[2] W.S. Hummers, R.E. Offeman, Preparation of Graphitic Oxide, Journal of the American Chemical Society, 80 (1958) 1339-1339.

[3] J. Ellison, C. Batchelor-McAuley, K. Tschulik, R.G. Compton, The use of cylindrical micro-wire electrodes for nano-impact experiments; facilitating the sub-picomolar detection of single nanoparticles, Sensors and Actuators, B: Chemical, 200 (2014) 47-52.

Chapter 3

Characterisation of Palladium Nanoparticles Decorated Graphene Oxides

Graphene oxides (GOs) are popular catalyst supports for precious metals in nanoparticle form. The hydrogen oxidation reaction (HOR) and the hydrogen evolution reaction (HER) on *individual* GO platelets decorated with Pd nanoparticles (Pd/GOs) were investigated in this chapter and suggest that the catalytic activity is confined to zone physically close to the point of electrical contact between platelet and electrode with just a fraction of the platelet active. Moverover, the electrochemical characterisation of the Pd/GO platelets is essential for the work reported in Chapter 6 concering the oxidation of hydrazine.

The work of Chapter 3 has been published in the journal *Angewandte Chemie International Edition*,[1] and was carried out under the supervision of Prof. Richard G. Compton (University of Oxford) and in collaboration with Dr. Lifu Chen (University of Oxford) who helped with the interpretation of the experimental results, Prof. Lidong Shao (Shanghai University of Electric Power) who synthesized the Pd/GO materials and provided the Pd weight loading information, and Prof. Bingsen Zhang (Chinese Academy of Sciences, Shenyang) who provided the TEM images of the Pd/GO materials.

3.1 Introduction

Graphene oxide (GO) is a widely-used support for nanoparticle catalysis (see Appendix Section A3.1, Figure A3.1).[2-4] In the context of redox and electro catalysis, the rate of heterogeneous electron transfer (HET) to and from the decorated GO particles is a key parameter characterizing their catalytic role. Eng *et al.* reported that for $[Fe(CN)_6]^{3-/4-}$ in aqueous solution, the electron transfer rate constant on GO was slow but increased significantly on potassium-doped GO, giving a value comparable with that of graphene.[5] Punckt *et al.* investigated the effect of the reduction degree of GO upon the HET rate for the $[Fe(CN)_6]^{4-/3-}$ couple in aqueous solution via electrochemical impedance spectroscopy.[6] However, the accurate assessment of the rate of HET is challenging if, as is usual, it is measured from an ensemble of particles, since the response is that from a layer of GO particles cast onto an electrode surface from which it is impossible to deconvolute effects due to the heterogeneity of the sample and the uncertainty of the inter particle contact resistance. Moreover it is impossible to assess whether all the particles are active or indeed if individual particles show uniform activity across their surface.

Herein, *single* nanoparticle measurements[7-11] are used to study both the hydrogen oxidation reaction (HOR) and the hydrogen evolution reaction (HER) on individually impacting graphene oxide particles decorated with palladium nanoparticles (Pd/GOs):

$$H_2 - 2e^- \underset{HER}{\overset{HOR}{\rightleftarrows}} 2H^+ \tag{3.1}$$

In this way the issue of the extent of electrical contact is clarified and the intrinsic catalytic activity of individual particles is assessed.

3.2 Experimental

Details of the synthesis and characterisation methods of the Pd/GOs were presented in Section 2.1.

Cyclic voltammetry of HOR and HER at Pd/GO modified GC electrodes

A Pd/GO suspension with a concentration of 3.6×10^{-13} M was prepared by adding 0.5 mg of

Pd/GO to 5 mL deionized water. Then the mixture was sonicated for 15 minutes in a Fisher Scientific FB15050 ultrasonic bath to obtain a well-dispersed solution. 14 μL Pd/GO suspension was drop-cast onto the polished glassy carbon (GC) electrode (diameter: 3.0 mm) and left to dry under N_2 atmosphere. The polishing detail has been shown in Section 2.2.1. The modified GC electrode was employed as the working electrode, a saturated calomel electrode (SCE) as the reference electrode and a graphite rod as the counter electrode.

For the hydrogen oxidation reaction (HOR), 5 mL of 0.2 M KNO_3 solution was vigorously bubbled with H_2 for 15 min to be fully saturated prior to the measurements and a H_2 atmosphere was maintained during the experiment. Two control experiments were conducted: a bare electrode in the H_2-saturated 0.2 M KNO_3 solution and a Pd/GO modified electrode in the N_2-saturated 0.2 M KNO_3 solution.

For the hydrogen evolution reaction (HER), a solution consisting of 1 mM HNO_3 (0.32 μL) and 0.2 M KNO_3 (5 mL) was vigorously bubbled with N_2 for 15 min to remove dissolved oxygen before the measurements and an atmosphere of N_2 was maintained during the experiment. Two control experiments were conducted: a bare electrode in the same solution and a Pd/GO modified electrode in the N_2-saturated 0.2 M KNO_3 solution without the addition of HNO_3.

Voltammetry of HOR and HER on single Pd/GO: Nano-impacts and Cyclic Voltammetry

For the voltammetry on single Pd/GO, a carbon fibre microwire electrode (diameter: 7 μm, length: 1 mm) fabricated as the Section 2.2.2 shows was employed as the working electrode, with the same reference electrode and counter electrode as above. Note the potentiostat employed herein precisely conserves the charge transferred during an impact event.[12]

For HOR, 5 mL of 0.2 M KNO_3 solution was first bubbled vigorously with H_2 for 15 min to get a fully saturated solution and an atmosphere of H_2 was maintained during the experiment. Then 100 μL Pd/GO suspension was added and bubbled with H_2 for further 10 seconds to make an even suspension, followed by immediate chronoamperometric or CV scans. Chronoamperometry was used to look for current spikes and steps ('nano-impacts'). A control experiment was carried out in the N_2-saturated 0.2 M KNO_3 solution.

For HER, the solution consisting of 1 mM HNO_3 (3.2 μL) and 0.2 M KNO_3 (5 mL) was vigorously bubbled with N_2 for 15 min and an atmosphere of N_2 was maintained during the experiment. Then 100 μL Pd/GO suspension was added and bubbled with N_2 for further 10 seconds to make an even suspension, followed by immediate chronoamperometric or CV scans. The control experiment was carried out in the N_2-saturated KNO_3.

3.3 Results and Discussion

As illustrated in Figure 3.1, a flat sheet-like morphology of Pd/GO was observed via TEM and quasi-spherical Pd nanoparticles with an average diameter of 2.7 ± 0.2 nm (98 samples) were seen to be highly dispersed on the surface of the GO sheet. The sheets are very approximately square-shaped with a mean side length of 3.1 ± 0.2 μm (34 samples). The corresponding size distribution of the Pd/GO sheets and decorated Pd nanoparticles are shown in Figure A3.2. Note that the thickness of the GO platelets prepared this way is *ca.* 3.0 nm corresponding to 2 ~ 5 layers.[13-15]

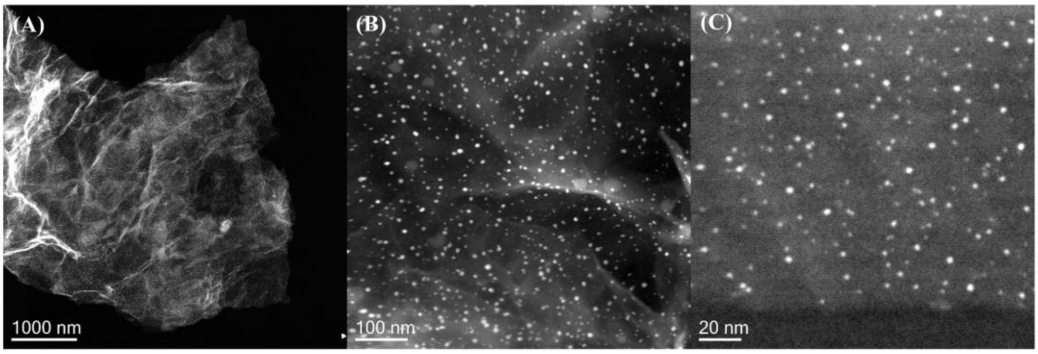

Figure 3.1. TEM images of graphene oxide nanosheets coated with palladium nanoparticles (Pd/GOs)

Both the hydrogen oxidation reaction (HOR) and hydrogen evolution reaction (HER) at the Pd/GO were investigated in this study. First, 14 μL of Pd/GO suspension was drop-casted on a glassy carbon (GC) macroelectrode and *ca.* four layers of Pd/GO nanosheets were immobilized on the electrode surface after drying. The cyclic voltammetry (CV) was then recorded on the Pd/GO modified electrode as shown in Figure 3.2A in the absence (dashed line) and presence (solid line) of hydrogen saturated solution. The latter corresponds to 0.77 mM based on Henry's Law solubility.[16] The voltammogram shows a quasi-reversible oxidation peak at -0.33 V vs SCE for hydrogen oxidation at the Pd/GO modified electrode. The experimental mid-point potential ($E_{1/2}$) of the oxidation reaction is determined as -0.42 V vs SCE, in excellent agreement with the thermodynamically calculated value of -0.43 V for HOR (see Appendix Section A3.3). The oxidative peak current was then studied as a function of scan rate as shown in Figure A3.3. The peak current was directly proportional to the square root of scan rate, suggesting a diffusion-controlled process. The diffusion coefficient of hydrogen was calculated to be $(5.3 \pm 0.4) \times 10^{-9}$ m^2 s^{-1} via the Randles-Sevcik equation (see Appendix Section A3.4), in agreement with the reported values of 5.0×10^{-9} m^2 s^{-1} at a Platinum microelectrode.[17] A control experiment was conducted with a bare GC electrode in a hydrogen-saturated solution (dotted line) and no voltammetric features were observed.

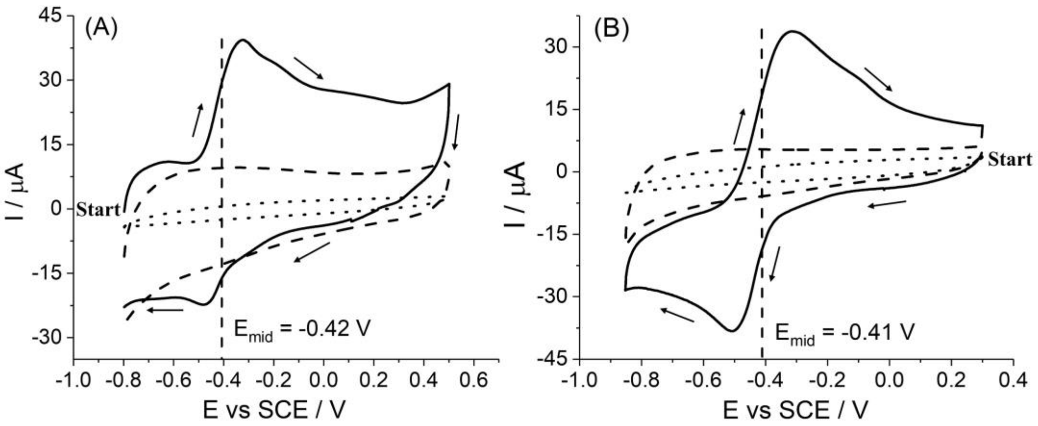

Figure 3.2. (A) Voltammogram at a bare GC electrode in H_2-saturated 0.2 M KNO_3 solution (dotted line), Voltammograms at a Pd/GO-modified GC electrode in 0.2 M KNO_3 solution saturated with N_2 (dashed line) and H_2 (solid line); (B) Voltammogram at a bare GC electrode in N_2-saturated solution containing 0.2 M KNO_3 and 1 mM HNO_3 (dotted line), Voltammograms at a Pd/GO-modified GC electrode in N_2-saturated 0.2 M KNO_3 solution with (solid line) and without (dashed line) HNO_3. Scan rate is 50 mV s^{-1}. Vertical dashed line represents the mid-point potential ($E_{1/2}$). The start and direction of the voltammogram scans are indicated.

Analogous experiments were conducted for HER in the N_2-degassed solution with 1 mM HNO_3 supported with 0.2 M KNO_3, as shown in Figure 3.2B. A clear reduction peak at -0.51 V vs SCE was seen in the voltammogram recorded with the modified electrode in the presence of HNO_3. The $E_{1/2}$ (-0.41 V) of the reduction reaction agrees with the thermodynamically calculated value of -0.44 V vs SCE and the measured diffusion coefficient of the proton is $(7.8 \pm 0.3) \times 10^{-9}$ m^2 s^{-1}, consistent with the literature value of 8.1×10^{-9} m^2 s^{-1}.[17]

Having evidenced the catalytic ability of the Pd/GO towards both HOR and HER, impact electrochemistry was then conducted to investigate this catalysis on individual Pd/GO particles. A clean carbon fibre microwire electrode (length *ca.* 1 mm and diameter *ca.* 7 μm) was inserted into a H_2-saturated solution containing 7.1×10^{-15} M Pd/GO and 0.2 M KNO_3 and chronoamperograms were immediately recorded at 0.6 V vs SCE. After several chronoamperometric scans, a clear current step was recorded as shown in Figure 3.3A whilst only capacitive charging of the electrode was observed in the absence of Pd/GO (Figure A3.5). This current step was ascribed to the HOR catalysed by a single Pd/GO stochastically impacting on the electrode surface. The sharp current onset manifests the arrival of the single entity at the electrode surface, and long duration of the current step reflects that the Pd/GO can remain immobilized for *ca.* 150 ± 60 s, the long timescale of which is partly indicative of the hindered diffusion of a particle close to a surface.[18] This long residence time of Pd/GO at the electrode surface enables the recording of CV signals for the HOR at single Pd/GO entities. Once the arrival of one particle is detected via the current change in the chronoamperogram, a cyclic voltammogram can then be immediately performed and completed before the particle departs from the electrode surface. As shown in Figure 3.3B, the voltammetric response was recorded exhibiting a steady state current at high overpotential for hydrogen oxidation, of which the magnitude (0.70 ± 0.25 nA) coincides well with that of the Faradaic current (0.65 ± 0.15 nA) detected via chronoamperometry. The observed current fluctuations likely correlate with the nanoscopic motion of the particle at the electrode surface that modulates the electric connection between the electrode and particle. Note the forward and reverse scans of the cyclic voltammetry show relatively little hysteresis consistent with the convergent/divergent diffusion of the nano entity. Figure 3.3C shows a step-off of the current in the chronoamperometric profile, indicating the loss of immobilized of Pd/GO from the electrode surface.

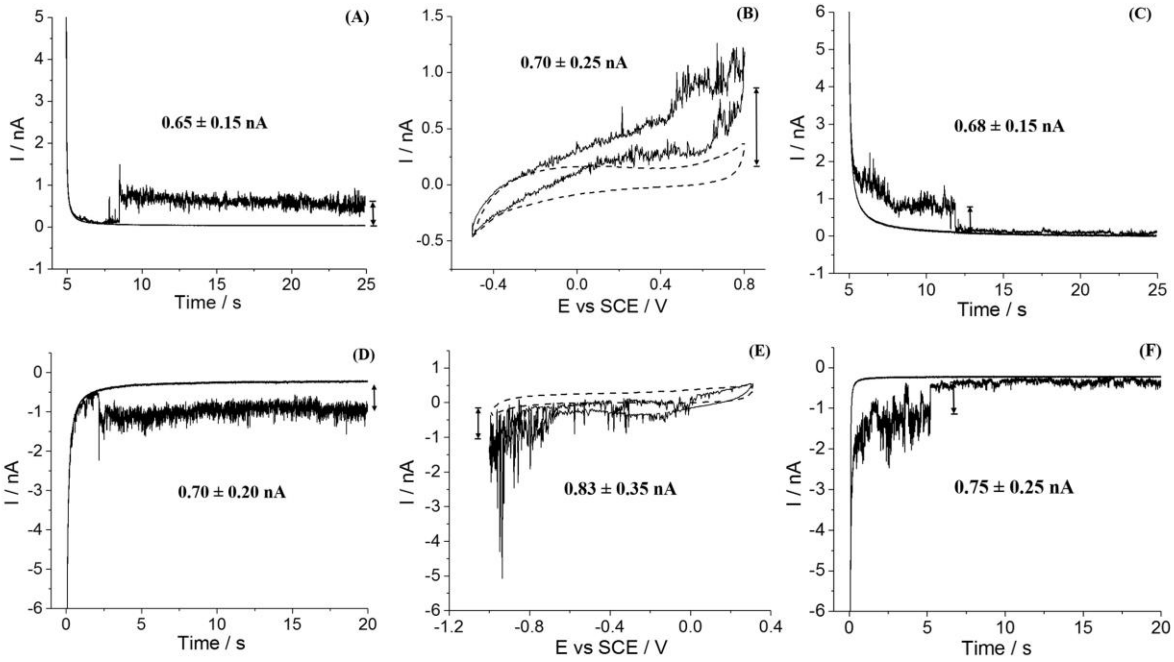

Figure 3.3. Chronoamperogram showing catalytic oxidative Faradaic steps from Pd/GO single particle impacts in H_2-saturated 0.2 M KNO_3 solution at 0.6 V (A: collision of Pd/GO with the wire electrode; C: falling-off). Voltammogram B of HOR at single immobilized Pd/GO on the wire electrode. D, E and F show the catalytic HER at Pd/GO in 1 mM HNO_3 supported with 0.2 M KNO_3 (at -0.9 V for D and F).

Impacts of HOR at single Pd/GO were then recorded at a series of applied potentials from -0.4 V to 0.8 V and the average current steps at each potential were obtained, as shown in Figure 3.4A, where the average current steps at potentials more positive than 0.6 V shows a plateau at *ca.* 0.60 nA. Mass-transport corrected Tafel analysis[19] was then performed on the 'voltammogram-like' feature in Figure 3.4A to separate out the electron transfer kinetics from the diffusion and give a single-particle measurement of the apparent anodic transfer coefficient β for the HOR (see Appendix Section A3.6). The apparent β was estimated to be 0.28 ± 0.01 in accord with that obtained from the macroelectrode (0.30).

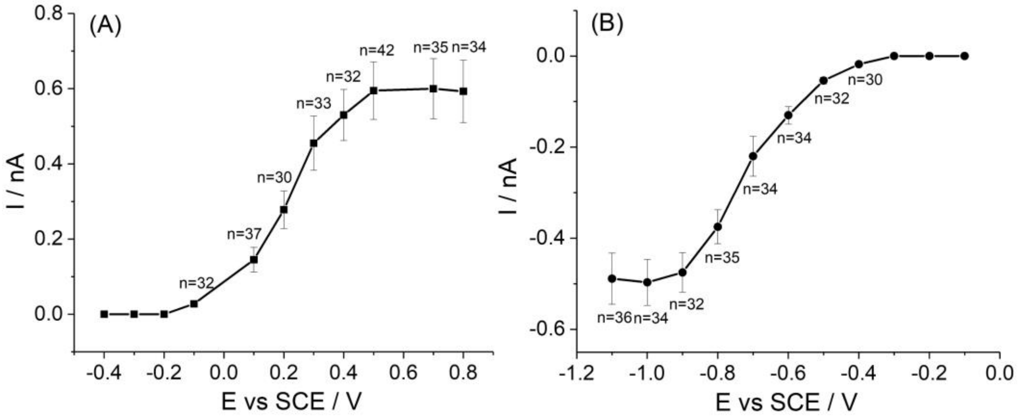

Figure 3.4. The average Faradaic step currents for HOR (A) and HER (B) on collided individual Pd/GO at different potentials. The error bars are derived from SD/$(n)^{1/2}$, where SD is the standard deviation and n is the number of the steps analysed.

Analogous impact experiments were conducted for HER in the N_2-degassed solution with 1 mM HNO_3 supported with 0.2 M KNO_3 on a carbon microwire electrode, as shown in Figure 3.3D-F. Potential variation study was also conducted and the average current steps plateaued at around -0.49 nA at potentials more negative than -0.9 V vs. SCE, as shown in Figure 3.4B. The apparent cathodic transfer coefficient α was found to be 0.26 ± 0.01 (vs. 0.32 for drop-casted macroelectrode).

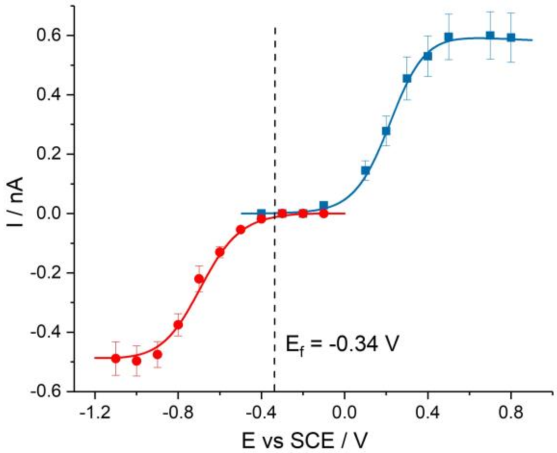

Figure 3.5. DIGISIM-simulated curves for HOR (blue line) and HER (red line) based on experimentally voltammogram-like features (squares for HOR and circles for HER).

Under diffusion-controlled conditions, the reaction rates of both HOR and HER are not expected to be sensitive to the Pd coverage on the GO nanosheets because the interparticle distance of Pd on GO is tiny compared to the diffusion layer thickness established. Consequently, both the chronoamperometric current steps and the quasi-steady-state current from CV of the impacted Pd/GO allow in principle the assessment of the sizing of the decorated GO platelets. First, the Pd/GO platelets immobilized flat on the surface of the carbon fibre as Figure 3.6A shows was modelled as a square electrode, considering the catalysis can proceed on the whole GO plane. The side length was calculated to be *ca.* 0.36 μm and 0.31 μm from HOR and HER respectively (see Appendix Section A3.7). However, these two values are much smaller than the actual size obtained from TEM, which implies that the contact between the GO and electrode is likely partial. If the contact with the platelet edge or corner (Figure 3.6A) were considered, the Pd/GO was treated as a microband electrode using the known width of 3.0 nm of the platelets. The length of the platelets was determined as 3.3 ± 0.1 μm and 2.9 ± 0.1 μm from the HOR and HER limiting currents respectively (see Appendix Section A3.7). This is consistent with the value from TEM analysis for the dimension of the square platelets. This was further evidenced by comparing the size distributions of these electrochemically assessed lengths with the data obtained from TEM, as shown in Figure A3.7. The correspondence between TEM and electrochemical sizing allows us to suggest that both HOR and HER only occur at or near the contact area between Pd/GO and electrode surface, which results from, at least in part, the high resistance of the ultrathin GO blocks preventing movement of electrons through the whole sheet.

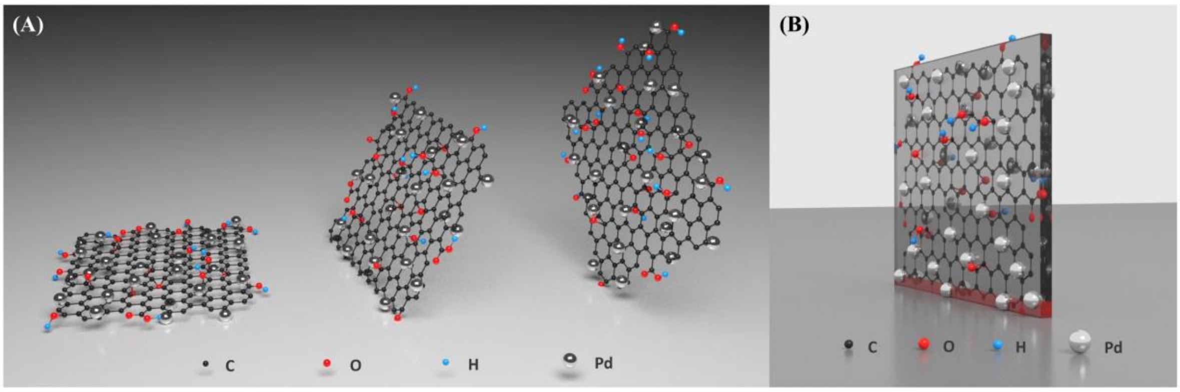

Figure 3.6. (A) Models of Pd/GO particles impacting onto the surface of carbon fibre: flat (left), edge (middle) and corner (right). (B) The highlighted red rectangle schematically represents the likely active area at or near the contact between Pd/GO particles and electrode.

To explore the kinetics of both reactions, DIGISIM[20] was next employed to model the observed voltammetry based on Butler-Volmer kinetics. A hemicylindrical band electrode geometry with the equivalent radius, r, of 1.0 nm according to the equation $r = w / \pi$ was used to approximate a microband electrode with a side length w of 3.2 μm (Figure 3.6B).[21] The formal potential of reactions, transfer coefficients and diffusion coefficients of both hydrogen and proton are given above. Consequently, the electrochemical rate constant k, the only unknown parameter, can be determined by fitting the numerical simulations to the voltammograms from impact electrochemistry (see Appendix Section A3.9). Figure 3.5 shows the excellent fitting between simulated voltammograms and the experimental data obtained from individual Pd/GO, and very fast rate constants, $k_{HOR} = 0.1$ cm s^{-1} and $k_{HER} = 1.6$ cm s^{-1}, were obtained. The voltammetric visibility of fast reaction rates is attributed to the very high mass transport conditions for HOR and HER occurring on single Pd/GO particles.

3.4 Conclusions

To conclude, both hydrogen oxidation reaction and hydrogen evolution reaction on ensemble and individual Pd/GO were investigated in this work. Impact electrochemistry reveals that the reactions only take place near the contact area, formally modelled as analogous to a microband electrode, between the GO and the electrode, as a result of the high resistance of the ultrathin GO with the size of the active area possibly controlled by tunnelling from the substrate electrode. Moreover, important and meaningful kinetic data was extracted via simulation showing fast electrochemical rate constants of k_{HOR} (0.1 cm s^{-1}) and k_{HER} (1.6 cm s^{-1}) at high mass transport conditions. This provides a new generic approach for the accurate assessment of the kinetics of catalytic reactions.

Appendix

Section A3.1: Structure of graphene oxide

Abundant oxygen functional groups (epoxide, hydroxyl, carboxyl, etc.) existing on the plane of GO can serve as both anchoring sites to support the decoration of multifarious metals and reaction centres for sensing as well as electrochemistry, the distribution and coverage of which vary greatly with different preparation methods.[3, 4] The C/O ratio on GO is *ca.* 2 ~ 10, and the relative atomic percentages of C = C/C – C, C – OH, C – O – C and O – C = O are 40 ~ 80%, 10 ~ 50%, 0 ~ 5% and 1 ~ 6% respectively.[22, 23] Water molecules in the interlayers of the GO sheets interact with the epoxides and hydroxyls on the basal plane through hydrogen bonding, which is essential for the stacking structure of the GO layers, as Figure A3.1 illustrates.[24, 25] However, the heavy density of functionality simultaneously decreases the electrical conductivity of GO even to the order of 10 S m^{-1} which is about 4 ~ 5 orders of magnitude lower than pristine graphene or graphite.[26]

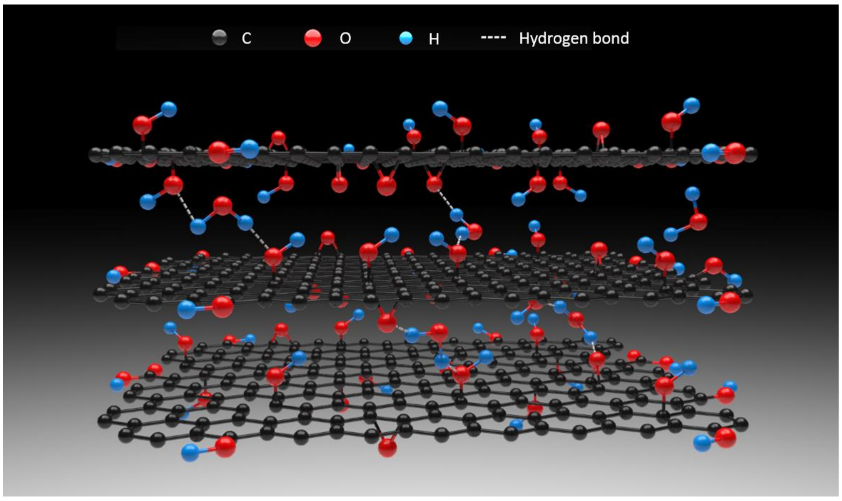

Figure A3.1. Schematic diagram of graphene oxide

Section A3.2: Size distributions of Pd/GO nanosheets and Pd nanoparticles

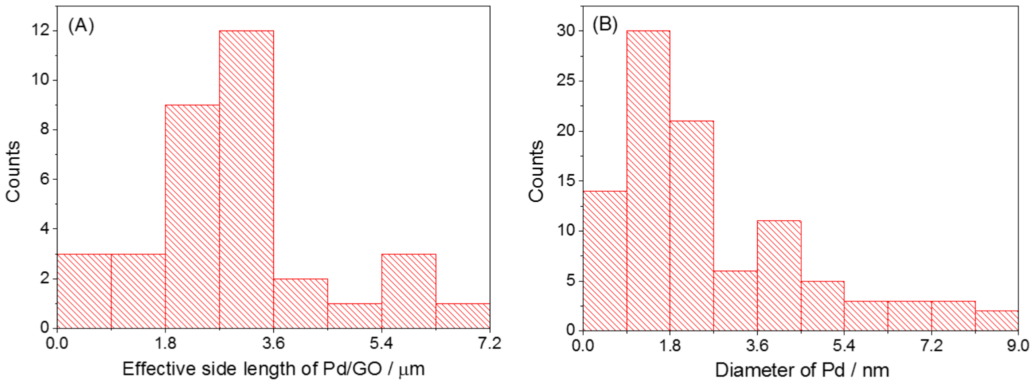

Figure A3.2. (A) The effective side length distribution of square-assumed Pd/GO nanosheets from the TEM analysis, giving the average length is 3.1 ± 0.2 µm (34 samples). (B) The diameter distribution of Pd nanoparticles on the Pd/GO surface from the TEM analysis via the software ImageJ, giving the mean diameter is 2.7 ± 0.2 nm (98 samples).

Section A3.3: Calculation of formal potential and midpoint potential

The formal potential of H^+/H_2 redox couple can be calculated using the following expression[17]:

$$E_f^0 = E^0_{H^+/H_2} + \frac{RT}{F}\ln\left(\frac{\gamma_{H^+}\Big/\left(p^0\right)^{1/2}}{K_{H_2}^{1/2}10^{k_s c_s/2}\left(a^0\right)^{1/2}}\right) \tag{3.2}$$

where the standard hydrogen electrode potential $E^0_{H^+/H_2}$ is 0.00 V; the gas constant R is 8.314 J K^{-1} mol^{-1}; the temperature T is 298.15 K; the Faraday constant F is 96485 C mol^{-1}; the proton activity coefficient γ_{H^+} is 0.754[27]; the standard pressure p^0 according to the IUPAC definition is 1 bar; the Henry's law constant of hydrogen K_{H_2} is 1292 dm^3 bar mol^{-1} under the temperature of 298 K and the pressure of 1.013 bar; the salt parameter k_s for molecular hydrogen in an aqueous KNO_3 is 0.07 dm^3 mol^{-1}[28]; the electrolyte KNO_3 concentration c_s is 0.2 mol dm^{-3}; the standard activity a^0 is 1 mol dm^{-3}. The formal potential E_f^0 was calculated in this way to be -0.0997 V vs SHE, namely -0.34 V vs SCE.

The half-wave potential for a macroelectrode voltammetric response varies with the concentration of H_2 and H^+ due to the non-1:1 stoichiometry of electrode reactions. However, under steady-state conditions, the half-wave potential is approximately the same as the midpoint potential. Hence, the midpoint potential is defined as[29]:

for HOR

$$E_{1/2} = \frac{RT}{F}\ln\left(\frac{D_{H_2}}{D_{H^+}}\frac{2c_{H_2}}{c^*}\right)^{1/2} + E_f^0 \tag{3.3}$$

for HER

$$E_{1/2} = \frac{RT}{F}\ln\left(\frac{D_{H_2}}{D_{H^+}}\frac{2c_{H^+}}{c^*}\right)^{1/2} + E_f^0 \tag{3.4}$$

where the diffusion coefficient D_{H_2} and D_{H^+} are (5.3 ± 0.3) × 10^{-9} m^2 s^{-1} and (7.8 ± 0.3) × 10^{-9} m^2 s^{-1} respectively; the concentrations c_{H_2} for HOR and c_{H^+} for HER are 0.77 mM and 1 mM respectively; the standard concentration c^* is 1 M. The midpoint potentials for the HOR and the HER at GC electrode under such conditions are calculated to be -0.43 V and -0.44 V, respectively.

Section A3.4: Tafel analysis and calculation of diffusion coefficients

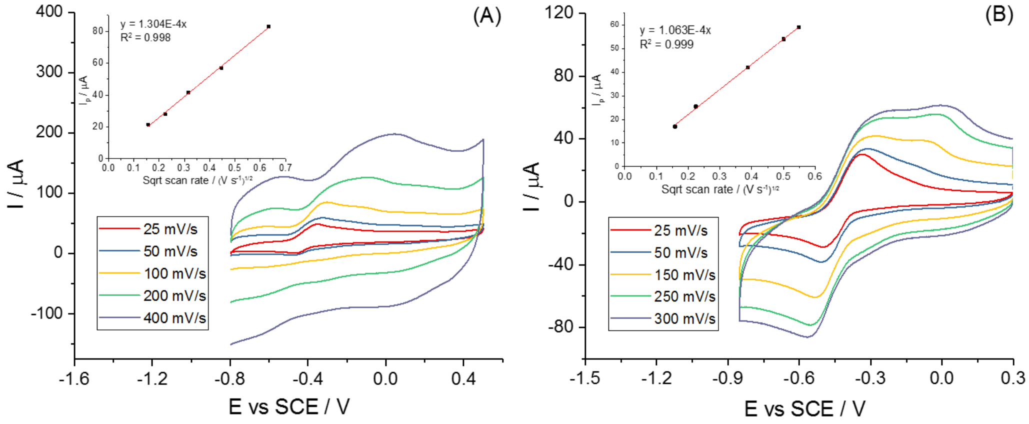

Figure A3.3. (A) CVs of the GC electrode modified with Pd/GOs in H_2-saturated 0.2 M KNO_3 at different scan rates: 25, 50, 100, 200 and 400 mV s^{-1}. Inset: plot of oxidative peak current and square root of scan rate. (B) CVs of the GC electrode modified with Pd/GOs in N_2-saturated 1 mM KNO_3 supported with 0.2 M

KNO_3 at different scan rates: 25, 50, 150, 250 and 300 mV s^{-1}. Inset: plot of reductive peak current and square root of scan rate. The Tafel Slopes are obtained from the Tafel analysis for HOR and HER on macroelectrode in the Figure A3.3 to be 11.7 ± 0.05 V^{-1} and 12.6 ± 0.04 V^{-1} respectively.

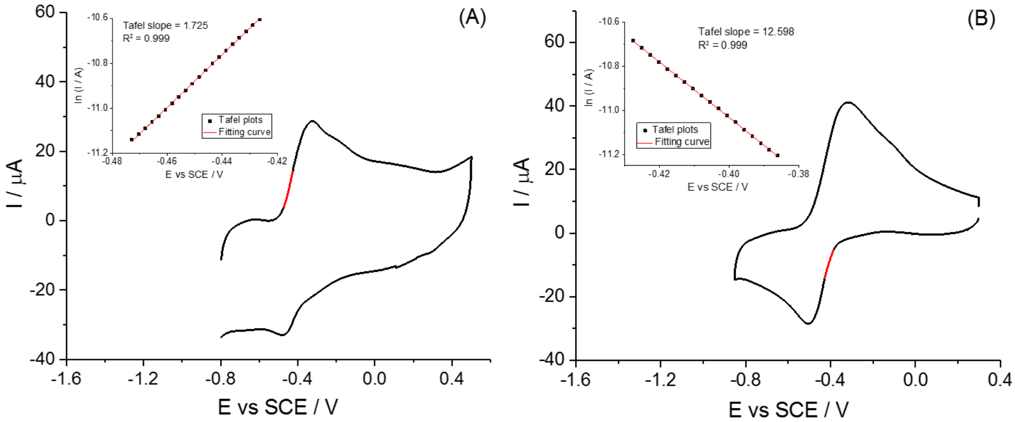

Figure A3.4. (A) CV of the GC electrode modified with Pd/GOs in H_2-saturated 0.2 M KNO_3 at 50 mV s^{-1}. Inset: Tafel plot of the highlighted part of the CV. (B) CV of the GC electrode modified with Pd/GOs in N_2-saturated 1 mM KNO_3 supported with 0.2 M KNO_3 at 50 mV s^{-1}. Inset: Tafel plot of the highlighted part of the CV.

Considering the HOR, the oxidative transfer coefficient β is estimated to be 0.30 ± 0.01 using the following expression:

$$\beta = Tafel \times \frac{RT}{F} \tag{3.5}$$

The Randles-Sevcik equation for an irreversible process at 298 K in which the first electron transfer is rate-determining[30]:

$$I_p = 2.99 \times 10^5 n \beta^{1/2} c A D^{1/2} v^{1/2} \tag{3.6}$$

where the relationship of peak current I_p and square root of scan rate is shown in Figure A3.3; the number of electrons transferred n is 2; the geometric area of the GC electrode A is 7.07 × 10^{-6} m^2 (diameter: 3.0 mm); the analyte concentration c is 0.77 mM. The diffusion coefficient D_{H_2} was calculated to be (5.3 ± 0.4) × 10^{-9} m^2 s^{-1} (literature value of 5.0 × 10^{-9} m^2 s^{-1})[17].

Analogous analysis was conducted for the HER. As the number of electron transferred is 1 and the analyte concentration c is 1 mM, the diffusion coefficient D_{H^+} is calculated to be (7.8 ± 0.3) × 10^{-9} m^2 s^{-1} (literature value of 8.1 × 10^{-9} m^2 s^{-1})[17] with the apparent reductive transfer coefficient α of 0.32 ± 0.01.

Section A3.5: Control experiments of nano-impacts in the absence of Pd/GO

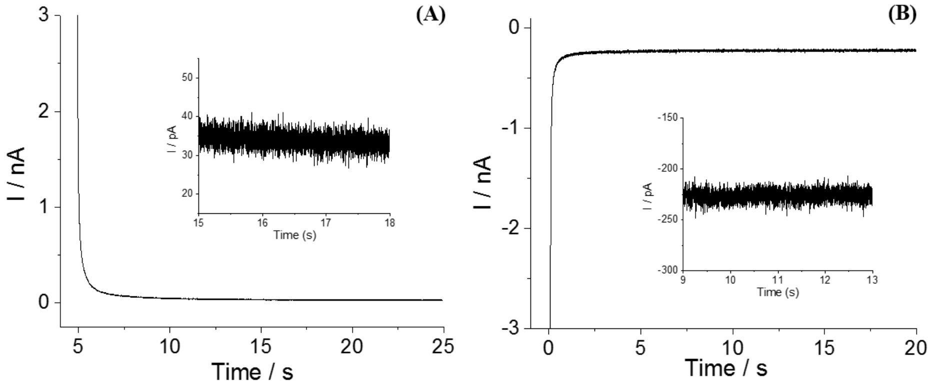

Figure A3.5. Chronoamperograms of the carbon fibre electrode (A) at 0.6 V vs SCE in H_2-saturated 0.2 M KNO_3 in the absence of Pd/GO and (B) at -0.9 V vs SCE in 1 mM HNO_3 supported with 0.2 M KNO_3 in the absence of Pd/GO.

Section A3.6: Mass transport corrected Tafel analysis

The Tafel Slopes were obtained from the mass transport corrected Tafel analysis for HOR and HER on microelectrode in the Figure A3.6 to be 10.2 ± 0.3 V^{-1} and 10.8 ± 0.4 V^{-1} respectively. The transfer coefficient β and α are 0.28 ± 0.01 and 0.26 ± 0.01 correspondingly.

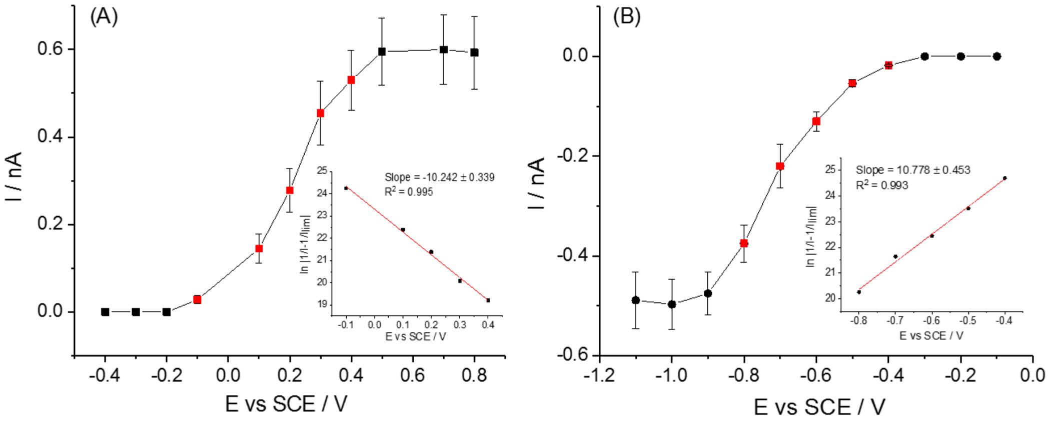

Figure A3.6. Squares for HOR (A) and circles for HER (B) formed by recording the average currents of the Faradaic steps from nano-impacts of individual Pd/GO at different potentials. Inset: Tafel plot of the highlighted points.

Section A3.7: Calculation of the steady-state current based on square and on microband electrode models

For a square/rectangular/band electrode with the length l and the width w, the normalised current at the electrode surface for time t is given[21, 31]:

$$i(t) = nFDclf(\tau) \tag{3.7}$$

with

$$f(\tau) = 1.004 + \frac{1}{\sqrt{\pi\tau}} + 1.3\exp(-2.53x) + \left(-1.133 + \frac{0.59}{1+\exp\left(\frac{x-1}{0.3415}\right)}\right) \times \exp\left(\frac{-9.85}{\left|\ln\left[\tau\left(17.22 - \frac{18.04}{1+\exp\left(\frac{x-1.113}{0.367}\right)}\right)\right]\right|}\right) \tag{3.8}$$

$$\tau = \frac{Dt}{w^2} \tag{3.9}$$

$$x = \log_{10}\frac{l}{w} \tag{3.10}$$

where the diffusion coefficient D and the analyte concentration c have been given before; the time t is 20 s.

Modelling the Pd/GO immobilized on the wire as a square electrode ($l = w$, hence $x = 0$), the side length was calculated to be *ca.* 0.36 μm and 0.31 μm from HOR and HER respectively.

Modelling the Pd/GO as a microband electrode ($l \gg w = 3.0\,nm$), the length of the Pd/GO was then determined as 3.3 ± 0.1 μm and 2.9 ± 0.1 μm from HOR and HER respectively.

Section A3.8: Comparison of length distributions among TEM, chronoamperometry and cyclic voltammetry

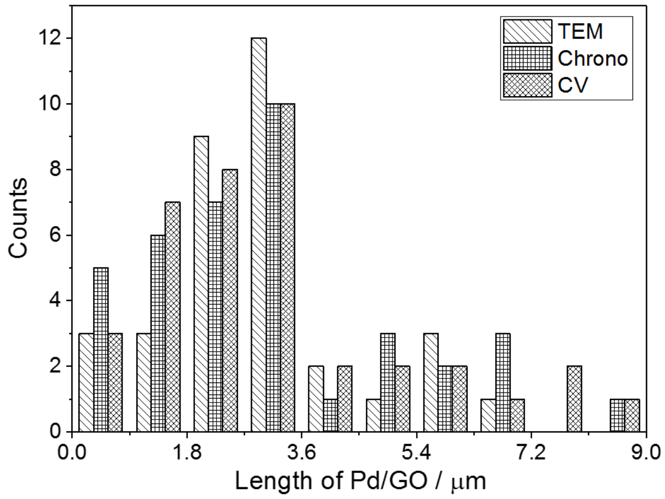

Figure A3.7. Comparison of the length distribution of Pd/GO amongst TEM analysis (34 samples), the chronoamperometry method for HOR at the potential of 0.6 V (38 samples) and the cyclic voltammetry method for HOR (38 samples).

Section A3.9: Simulation for electrochemical rate constants of HOR and HER via DIGISIM

The simulation was carried out using a commercial software DIGISIM to model the observed voltammetry based on Butler-Volmer kinetics. The proximal fitting model selected is hemicylindrical electrode geometry, of which the length is equivalent to that of the microband (3.2 μm) and the approximate radius is 1.0 nm according to the equation $r = w/\pi$. The transfer coefficient β and α from the mass transport corrected analysis on nano-impacts are correspondingly 0.28 and 0.26. The diffusion coefficients D_{H_2} and D_{H^+} were 5.3 × 10^{-9} m^2 s^{-1} and 7.8 × 10^{-9} m^2 s^{-1} at 298.2 K respectively as obtained in see Appendix Section A3.4. The formal potential E_f for the H_2/H^+ redox couple was calculated to be -0.34 V vs SCE (see

Appendix Section A3.3).

For HOR, two one-electron oxidation steps are set up:

$$H_2 - e^- = H_2^+ \tag{3.11}$$

$$H_2^+ - e^- = 2H^+ \left(fast \right) \tag{3.12}$$

The bulk concentration of C_{H_2} is 0.77 mM whilst $C_{H_2^+}$ and C_{H^+} are both 0 mM at the beginning of simulation. As the first step is rate-determining, we choose the limit value of 1 × 10^4 cm s^{-1} as the electrochemically rate constant of the second step to make it fully driven. Under the value of β, the experimental results from nano-impacts of individual Pd/GO in Figure 3.4A were fitted by numerical simulation of the H_2 oxidation process as the blue line in Figure 3.5 illustrates. The best fitting result gives the rate constant of k_{HOR} = 0.1 cm s^{-1}.

For HER, a simple one-electron reduction step is established:

$$H^+ + e^- = \frac{1}{2} H_2 \tag{3.13}$$

The bulk concentration of C_{H^+} is 1 mM as C_{H_2} is 0 mM. The simulation of the H^+ reduction process was performed to fit with the results in Figure 3.4B as the red line in Figure 3.5 shows. Likewise, the rate constant of k_{HER} = 1.6 cm s^{-1} is obtained.

References

[1] R. Miao, L. Chen, L. Shao, B. Zhang, R.G. Compton, Electron transfer to decorated graphene oxide particles, Angewandte Chemie-International Edition, 131 (2019) 12679-12682.

[2] C.K. Chua, M. Pumera, Chemical reduction of graphene oxide: a synthetic chemistry viewpoint, Chemical Society Reviews, 43 (2014) 291-312.

[3] Z. Sofer, J. Luxa, O. Jankovsky, D. Sedmidubsky, T. Bystron, M. Pumera, Synthesis of Graphene Oxide by Oxidation of Graphite with Ferrate(VI) Compounds: Myth or Reality?, Angewandte Chemie-International Edition, 55 (2016) 11965-11969.

[4] A. Bagri, C. Mattevi, M. Acik, Y.J. Chabal, M. Chhowalla, V.B. Shenoy, Structural evolution during the reduction of chemically derived graphene oxide, Nature Chemistry, 2 (2010) 581-587.

[5] A.Y.S. Eng, H.L. Poh, J. Luxa, Z. Sofer, M. Pumera, Potassium assisted reduction and doping of graphene oxides: towards faster electron transfer kinetics, RSC Advances, 3 (2013) 10900-10908.

[6] C. Punckt, M.A. Pope, Y.F.M. Liu, I.A. Aksay, Structure-Dependent Electrochemistry of Reduced Graphene Oxide Monolayers, Journal of the Electrochemical Society, 163 (2016) H491-H498.

[7] W. Xu, G. Zou, H. Hou, X. Ji, Single Particle Electrochemistry of Collision, Small, (2019) e1804908.

[8] L.K. Allerston, N.V. Rees, Nanoparticle impacts in innovative electrochemistry, Current Opinion in Electrochemistry, 10 (2018) 31-36.

[9] K.J. Stevenson, K. Tschulik, A materials driven approach for understanding single entity nano impact electrochemistry, Current Opinion in Electrochemistry, 6 (2017) 38-45.

[10] G. Zampardi, C. Batchelor-McAuley, E. Katelhon, R.G. Compton, Lithium-Ion-Transfer Kinetics of Single LiMn2O4 Particles, Angewandte Chemie-International Edition, 56 (2017) 641-644.

[11] W. Xu, Y.G. Zhou, X.B. Ji, Lithium-Ion-Transfer Kinetics of Single $LiFePO_4$ Particles, Journal of Physical Chemistry Letters, 9 (2018) 4976-4980.

[12] E. Katelhon, E.E.L. Tanner, C. Batchelor-McAuley, R.G. Compton, Destructive nano-impacts: What information can be extracted from spike shapes?, Electrochimica Acta, 199 (2016) 297-304.

[13] K.P. Loh, Q.L. Bao, G. Eda, M. Chhowalla, Graphene oxide as a chemically tunable platform for optical applications, Nature Chemistry, 2 (2010) 1015-1024.

[14] G. Eda, M. Chhowalla, Chemically Derived Graphene Oxide: Towards Large-Area Thin-Film Electronics and Optoelectronics, Advanced Materials, 22 (2010) 2392-2415.

[15] S. Stankovich, R.D. Piner, S.T. Nguyen, R.S. Ruoff, Synthesis and exfoliation of isocyanate-treated graphene oxide nanoplatelets, Carbon, 44 (2006) 3342-3347.

[16] E. Wilhelm, R. Battino, R.J. Wilcock, Low-Pressure Solubility of Gases in Liquid Water, Chemical Reviews, 77 (1977) 219-262.

[17] X. Jiao, C. Batchelor-McAuley, E. Katelhon, J. Ellison, K. Tschulik, R.G. Compton, The Subtleties of the Reversible Hydrogen Evolution Reaction Arising from the Nonunity Stoichiometry, Journal of Physical Chemistry C, 119 (2015) 9402-9410.

[18] S. Eloul, R.G. Compton, General Model of Hindered Diffusion, Journal of Physical Chemistry

Letters, 7 (2016) 4317-4321.

[19] R.G. Compton, C.E. Banks, Understanding Voltammetry, 3rd edition., World Scientific, London, 2018.

[20] M. Rudolph, D.P. Reddy, S.W. Feldberg, A simulator for cyclic voltammetric responses, Analytical Chemistry, 66 (1994) 589A-600A.

[21] J. Heinze, Ultramicroelectrodes in Electrochemistry, Angewandte Chemie-International Edition, 32 (1993) 1268-1288.

[22] S. Park, R.S. Ruoff, Chemical methods for the production of graphenes, Nature Nanotechnology, 4 (2009) 217-224.

[23] Z.W. Xie, Z.L. Yu, W.F. Fan, G.C. Peng, M.Z. Qu, Effects of functional groups of graphene oxide on the electrochemical performance of lithium-ion batteries, RSC Advances, 5 (2015) 90041-90048.

[24] S. Kim, S. Zhou, Y.K. Hu, M. Acik, Y.J. Chabal, C. Berger, W. de Heer, A. Bongiorno, E. Riedo, Room-temperature metastability of multilayer graphene oxide films, Nature Materials, 11 (2012) 544-549.

[25] Y.W. Zhu, S. Murali, W.W. Cai, X.S. Li, J.W. Suk, J.R. Potts, R.S. Ruoff, Graphene and Graphene Oxide: Synthesis, Properties, and Applications (vol 22, pg 3906, 2010), Advanced Materials, 22 (2010) 5226-5226.

[26] W. Kundhikanjana, K.J. Lai, H.L. Wang, H.J. Dai, M.A. Kelly, Z.X. Shen, Hierarchy of Electronic Properties of Chemically Derived and Pristine Graphene Probed by Microwave Imaging, Nano Letters, 9 (2009) 3762-3765.

[27] R.A. Robinson, R.H. Stokes, Tables of Osmotic and Activity Coefficients of Electrolytes in Aqueous Solution at 25-Degrees-C, Transactions of the Faraday Society, 45 (1949) 612-624.

[28] F.A. Long, W.F. Mcdevit, Activity Coefficients of Nonelectrolyte Solutes in Aqueous Salt Solutions, Chemical Reviews, 51 (1952) 119-169.

[29] A. Jaworski, M. Donten, Z. Stojek, J.G. Osteryoung, Conditions of strict voltammetric reversibility of the H+/H-2 couple at platinum electrodes, Analytical Chemistry, 71 (1999) 243-246.

[30] L. Sepunaru, S.V. Sokolov, J. Holter, N.P. Young, R.G. Compton, Electrochemical Red Blood Cell Counting: One at a Time, Angewandte Chemie-International Edition, 55 (2016) 9768-9771.

[31] I.J. Cutress, R.G. Compton, Theory of square, rectangular, and microband electrodes through explicit GPU simulation, Journal of Electroanalytical Chemistry, 645 (2010) 159-166.

Chapter 4

Hydrazine Oxidation at Glassy Carbon: Marcusian Kinetics

The last chapter characterised the materials Pd/GO electrochemically which will be further studied upon its catalytic ability towards hydrazine oxidation in Chapter 6. Before that, the mechanism and kinetics of hydrazine oxidation at un-modified carbon surface is necessary to be well understood. This chapter reports that the phenomenological Butler-Volmer (BV) theory is not appropriate for interpreting the process of hydrazine oxidation for which an astonishingly wide range of transfer coefficients, Tafel slopes and diffusion coefficient have been previously reported. Rather Tafel analysis for voltammetry recorded at Glassy Carbon (GC) electrodes reveals a strong potential dependence of the anodic transfer coefficient, consistent with the symmetric Marcus-Hush (sMH) theory. According to the relationship $\beta = \frac{\lambda + FE_f^0}{2\lambda} - \frac{F}{2\lambda}E$, the reorganization energy (0.35 ± 0.07 eV) and an approximate formal potential of the rate-determining first electron transfer were successfully extracted from the voltammetric responses. The work of Chapter 4 has been published in the journal *Science China Chemistry*,[1] and was carried out under the supervision of Prof. Richard G. Compton (University of Oxford) and in collaboration with Dr. Lifu Chen (University of Oxford) who helped with the interpretation of the experimental results.

4.1 Introduction

Whilst the chemical oxidation of hydrazine, N_2H_4, historically helped to launch the V-2 rockets developed in Peenemunde by Wernher von Braun[2], the *electro*-oxidation of hydrazine has considerable modern interest in the form of a valuable anodic reaction for use in some practical fuel cells[3-5]. Accordingly, the latter has received extensive attention especially from the applications perspective. Of underpinning fundamental interest and importance is the rate of the heterogeneous electron transfer involved in the electro-oxidation, thought to display a high over-potential, and hence electrochemically irreversible kinetics implying that the latter are slow compared to prevailing rates of mass transport on many electrodes made of diverse materials. This has led to the design and use of surfaces that catalyse the oxidation notably through the adsorptive stabilisation of reactive intermediates on the formation of di-nitrogen from hydrazine, involving the loss of four electrons and four protons from the latter.

In this context it is of interest to consider the intrinsic electron transfer behaviour of N_2H_4 on surfaces where adsorption effects are reported to be minimal[6]. Accordingly, we have investigated the electron transfer kinetics of hydrazine at carbon electrodes as an essential prerequisite underpinning any mechanistic study of active electro-catalysts. The oxidation of hydrazine at carbon electrodes has mostly, been studied from the perspective of developing the chemical sensors demanded by society because of the high toxicity of hydrazine and where amperometric approaches to sensing are sought for reasons for sensitivity and cost effectiveness[7, 8].

Hydrazine is protonated in aqueous solution at pH values below *ca.* 8 since the pK_a is reported as 8.1 at 25 °C[9-11] where the electrochemical oxidation likely requires deprotonation to take place in a chemical step preceding the electron transfer. As the first electron transfer is rate-determining[12, 13], the reaction mechanism is generally given as

$$N_2H_5^+ \rightleftarrows N_2H_4 + H^+ \tag{4.1}$$

$$N_2H_4 \xrightarrow{slow} N_2H_4^{+} + e^{-} \tag{4.2}$$

$$N_2H_4^{+} \xrightarrow{fast} N_2 + 4H^{+} + 3e^{-} \tag{4.3}$$

and in which the chemical step contributes additional over-potential to the electrode process and in which the possibility of concerted electron and proton transfer cannot be excluded. Accordingly, for electrochemical applications hydrazine is generally used and studied under conditions of high pH where it is deprotonated in bulk solution. Perusal of the literature[14-16] shows that on Glassy Carbon (GC) whilst clearly defined and reproducible voltammetric oxidation waves are seen they have a characteristically exceptionally ‘drawn out’ shape even beyond that expected for a typical electrochemically highly irreversible process. Moreover, the literature shows a startling and unusual diversity of values reported for the diffusion coefficient of hydrazine when measured electrochemically and typically inferred from the magnitude of the voltammetric currents flowing. Table A4.1 in the Appendix Section A4.1 summarises some of the reported values, which span the range from 7.82×10^{-7} to 4.10×10^{-5} cm^2/s much greater than typically expected for quantitative electrochemistry.

Hitherto the voltammetry of hydrazine, as often attempted, has been interpreted as a 4-electron oxidation in which the first electron transfer is slow and rate-determining and governed by phenomenological Butler-Volmer (BV) kinetics[17] usually with a transfer coefficient below the value of 0.5 although Table A4.1 shows a wide range of reported values. However in this chapter we show that analysis of the measured voltammetric wave-shapes reveals a strong potential dependence of the observed anodic transfer coefficient with the value decreasing linearly with increasingly positive overpotential. Accordingly the data is further and successfully analysed using Marcus-Hush (MH) theory[18, 19] revealing a rather low value for the re-organisation energy associated with the first electron transfer as compared to many in the literature. Whilst the equivalence - and hence indistinguishability - of BV and MH theories of electron transfer from solution phase species is established for large reorganisation energies significant differences can appear for lower values[20]. Under the latter conditions a reduced limiting current governed by the rate of electron transfer kinetics and not the rate of diffusion is seen at microelectrodes[20]; in the present chapter an analogous observation is made in respect of the voltammetric peak currents resulting from the oxidation of hydrazine at carbon macro-electrodes and the results quantified. These observations may explain the varying diffusion coefficients (and Tafel slopes) reported in the literature (see Appendix Section A4.1) as well as explaining the intrinsically slow kinetics of hydrazine oxidation in the absence of adsorptive catalysis.

4.2 Experimental

The working electrode was a polished GC electrode of diameter 3 mm (CH Instruments Inc., USA). The reference electrode was a standard saturated calomel electrode SCE (BASi Inc., Japan) and the counter electrode was a graphite rod of diameter 6 mm (Sigma-Aldrich Ltd., UK). The aqueous electrolyte used was 1.5 mM N_2H_4 supported by 0.1 M PBS (pH 9). Before the electrochemical measurement, the electrolyte was thoroughly out-gassed and saturated with high-purity N_2 for 15 mins to remove the dissolved O_2 fully and then maintained under a N_2 atmosphere during the measurement. A control experiment was conducted without N_2H_4. A series of analogous experiments were conducted in various supporting electrolytes (0.3 M PBS, 0.5 M PBS as well as 0.5 M PBS with the addition of 0.2 M KCl) at pH 9.

4.3 Results and Discussion

Heterogeneous electron transfer processes in electrochemistry are typically interpreted in terms of the Butler-Volmer[21, 22] and/or Marcus-Hush (symmetric and asymmetric)[19, 20, 23] models. The rate of an interfacial electrochemical reaction can be expressed as:

$$j = k(n)\left[reactant\right]_0^n \tag{4.4}$$

where j is the flux of reactant undergoing electrolysis, n the order of the reactant and $\left[reactant\right]_0$ the surface concentration of the reactant.

For a one-electron redox reaction

$$A - e^- \underset{k_{red}}{\overset{k_{ox}}{\rightleftarrows}} B \tag{4.5}$$

where k_{ox} and k_{red} are the rate constants for the oxidation and reduction respectively. Thus, the flux can be written for the *net* process:

$$j = k_{ox}\left[A\right]_0 - k_{red}\left[B\right]_0 \tag{4.6}$$

where $\left[A\right]_0$ and $\left[B\right]_0$ are the surface concentrations of the species A and B respectively. The rate constants can be described by either the phenomenological Butler-Volmer equation or the microscopic Marcus-Hush approach as summarised in Section 1.2.

We next see how the different theories are reflected in predicted voltammograms recorded at macro-electrodes. It is assumed that the following is limited to diffusion-controlled charge transfer processes so giving the transport equations for the species A and B according to Fick's law:

$$\frac{\partial\left[A\right]}{\partial t} = D_A \frac{\partial^2\left[A\right]}{\partial x^2} \tag{4.7}$$

$$\frac{\partial\left[B\right]}{\partial t} = D_B \frac{\partial^2\left[B\right]}{\partial x^2} \tag{4.8}$$

where $[A]$ and $[B]$ are the concentrations of A and B respectively, D_A and D_B the diffusion coefficients of A and B respectively, t the time and x the distance normal to the electrode.

Digisim[24], a commercial finite difference based simulation software, was employed for modelling the cyclic voltammetry. This is based on the symmetric Marcus-Hush theory. Our aim was to explore the extent to which the peak current in cyclic voltammetry might be limited by finite electron transfer kinetics in the same way that micro-disc limiting currents can be so influenced[20]. The one-electron redox reaction ($A - e = B$) is considered to take place at the surface of a planar macrodisc electrode (diameter: 3.0 mm), where the mass-transport limited flux is mainly contributed by linear diffusion. The concentrations $[A]$ and $[B]$ were set as 1.5 mM and 0 respectively, and the diffusion coefficients D_A and D_B were both 1×10^{-5} cm^2/s. A value for the formal potential E_f^0 of 0 was assumed and a value of 1 eV for the reorganization energy λ.

Figure 4.1 shows the effect of changing the electrochemical rate constant k_0 keeping the other parameters. For fast k_0 the electrochemically reversible limit is reached with a peak current consistent with the Randles-Sevcik equation:

$$I_p = 2.69 \times 10^5 S[A] D_A^{1/2} v^{1/2} \tag{4.9}$$

where given the geometric area S of the electrode and the applied scan rate v, the peak current I_p only depends on the bulk concentration and diffusional properties of the reactant. Moreover the peak-to-peak potential separation of 57 mV observed is again consistent with the established analytical theory[25, 26]. On decreasing the value of k_0 the wave becomes irreversible and the peak current decreases with the forward peak shifting anodically as over-potential develops.

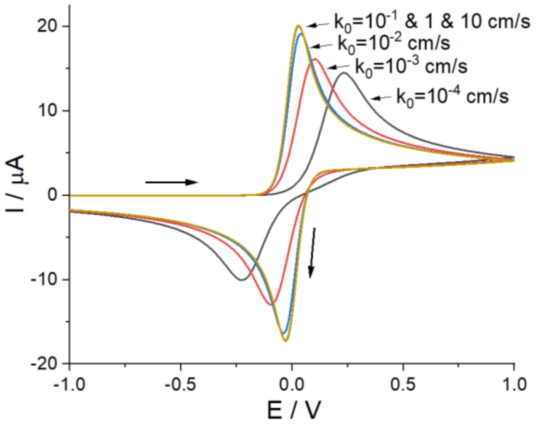

Figure 4.1. Theoretical voltammetry of the oxidation of A to B at a planar macrodisc electrode (diameter: 3 mm) using symmetric Marcus-Hush model for studying the effect of k_0. Parameters: E_f^0 = 0; λ = 1 eV; k_0 = 10^{-4}, 10^{-3}, … 10 cm/s; $[A]$ = 1.5 mM and $[B]$ = 0; D_A = D_B = 1×10^{-5} cm^2/s; v = 50 mV/s.

Next the effect of the reorganization energy λ on the typical cyclic voltammetry was studied. Figure 4.2 shows how the voltammetry responds to different values of the reorganization energy, λ = 0.2, 0.4 and 1 eV, for various values of k_0 in the range 10^{-4} to 10 cm/s. In general it is apparent that for low k_0, λ has the same influence on both oxidative and reductive peaks which are decreased in size significantly and broadened with a decrease of λ. This reflects the asymptotic behaviour of sMH kinetics that as λ decreases, the rate constants tend to level off at smaller overpotentials and give rise to smaller limiting current values[27]. For a fixed reorganization energy an increase in k_0 causes the voltammetric shape to become increasingly independent of λ, as the system becomes electrochemically reversible.

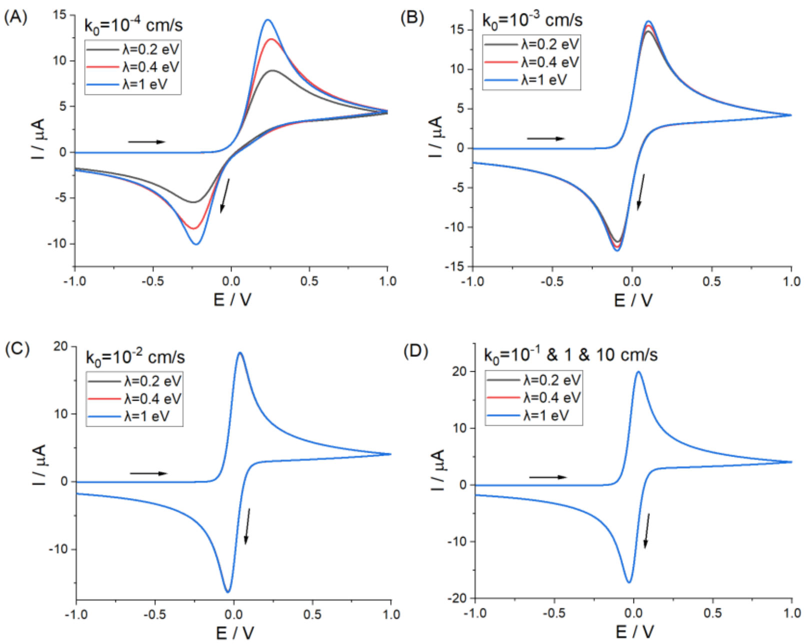

Figure 4.2. Theoretical voltammetry of the oxidation of A to B at a planar macrodisc electrode (diameter: 3 mm) using symmetric Marcus-Hush model for studying the effect of λ. Parameters: E_f^0 = 0; λ = 0.2, 0.4 and 1 eV; $[A]$ = 1.5 mM and $[B]$ = 0; D_A = D_B = 1 × 10^{-5} cm^2/s; ν = 50 mV/s; k_0 = (A) 10^{-4}, (B) 10^{-3}, (C) 10^{-2}, (D) 10^{-1}, 1 and 10 cm/s.

Then the disparity between the sMH and BV models in the variation of β with E was explored. Figure 4.3A presents the simulated voltammograms for the fully irreversible limit based on the BV (dotted) and sMH (dashed: λ = 0.5 eV and solid: λ = 1 eV) models with identical parameters, respectively, except for the choice of the reorganization energy and the transfer coefficient. The values of 1 eV and 0.5 were selected for comparison. The analysis over the current range of 1% to 99% of the peak current, namely the highlighted red parts of the figure, was conducted to give a plot of β with E as shown in Figure 4.3B, where β was obtained from the derivative of $\ln I$ with E according to $\beta = \frac{RT}{F}\frac{d\ln I}{dE}$. For BV, at very low currents, the measured anodic transfer coefficient β approaches the input value of 0.5 in the case of BV kinetics and the expected limit for sMH kinetics. A gradual deviation from the limit of 0.5 with the rise of overpotential is seen, especially from 0.3 to 0.45 V, on account of the depletion of the reactant at the electrode surface, reflecting an increasing mass transport effect. Hence, for practical analysis, usually the 10%~30% of the peak current is taken for Tafel analysis where the mass transport effect is minimal compared to the electrode kinetics since the diffusion layer is thin. Close to the peak current, β approaches zero. For sMH (both λ = 0.5 and 1 eV), β was observed to decrease almost linearly with the increasingly positive overpotential, even under conditions where diffusional effects are expected to be negligible (on the basis of the BV simulations) in accordance with the linear relationship described in $\beta = \frac{\lambda + FE_f^0}{2\lambda} - \frac{F}{2\lambda}E$ of Eq. (1.53). This observation contrasts markedly from the BV model for a fully irreversible process.

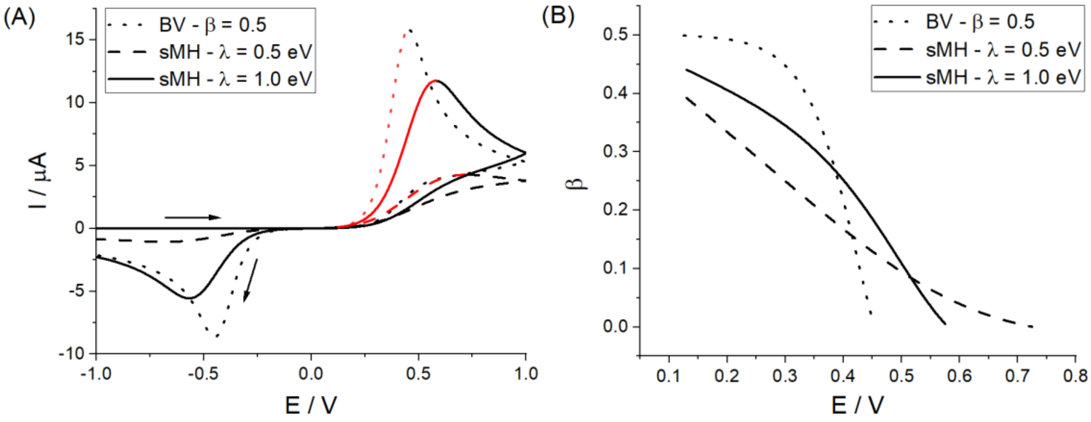

Figure 4.3. (A) Theoretical voltammetry of the oxidation of A to B at a planar macrodisc electrode (diameter: 3 mm) for studying the variation of β with E in the fully irreversible limit using the Butler-Volmer model with β = 0.5 (dotted) and symmetric Marcus-Hush model with λ = 0.5 (dashed) and 1 eV (solid). (B) Plot of β versus E analysed from the highlighted red parts of the voltammograms. Parameters: E_f^0 = 0; $k_0 = 10^{-6}$ cm/s; $[A]$ = 1.5 mM and $[B]$ = 0; D_A = D_B = 1×10^{-5} cm^2/s; v = 50 mV/s.

The electro-oxidation of hydrazine (N_2H_4) was studied via cyclic voltammetry (CV) at a Glassy

Carbon electrode to probe the *intrinsic* electron transfer kinetics of hydrazine. Figure 4.4A presents the voltammograms obtained at 50 mV/s in a 1.5 mM aqueous solution of N_2H_4 supported by 0.1 M PBS (pH 9). A fully irreversible wave with a peculiarly elongated shape was observed in the presence of N_2H_4 (solid) at 0.68 V vs SCE corresponding to four-electron hydrazine oxidation[6, 28], whereas no voltammetric features were shown in the absence of N_2H_4 (dashed). The effect of scan rate was investigated where an increase in the oxidative peak current was observed as shown in Figure 4.4B. The inset clearly indicates that the corresponding peak current was directly proportional to the square root of scan rate, suggesting a diffusion-controlled process.

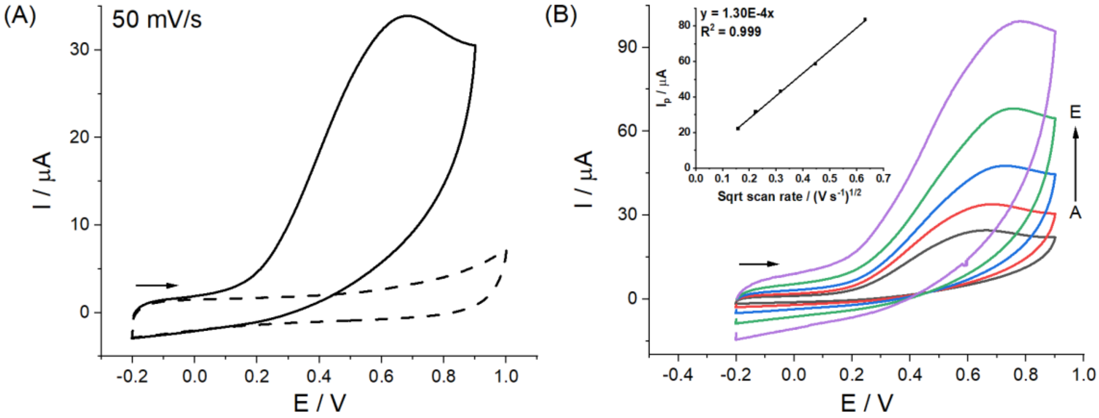

Figure 4.4. (A) Voltammograms on a GC electrode at 50 mV/s in 0.1 M PBS (pH 9) with 1.5 M hydrazine (solid) and without hydrazine (dashed). (B) Voltammograms recorded at different scan rates of 25, 50, 100, 200 and 400 mV/s (from A to E). The start of the voltammetric scans is indicated.

Tafel analysis was then applied for further exploring the electron transfer kinetics of the hydrazine oxidation. The region from 10% to 30% of the peak current was taken for analysis in order to avoid any influence from background currents (especially at very low overpotentials) or reactant depletion effects due to the limitation of mass transport.[29]. The local Tafel slopes at each potential were found by evaluating the derivative $\beta = \frac{RT}{F}\frac{\partial \ln|I_{ox}|}{\partial E}$. The Tafel plots (black) and the part of the voltammogram selected for fitting (red) for each scan rate are shown in Figure 4.5 where the anodic transfer coefficient β was observed to be strongly dependent on the potential E in a linearly negative relationship. This is exactly consistent with the symmetric Marcus-Hush (sMH) theory as depicted in Figure 4.3. Table 4.1 shows the evaluation of the formal potential and the reorganization energy for each of the scan rates studied. There is no systematic variation with scan rate of either parameter, thus λ is *ca.* 0.35 eV and E_f^0 is *ca.* 0.14 V, consistent with the absence of concentration depletion effects. Analogous experiments were conducted for different concentrations of hydrazine, for different buffer capacities and for different levels of supporting electrolytes as summarised in Table 4.2 where again a potential dependent transfer coefficient and a similar reorganization energy was observed.

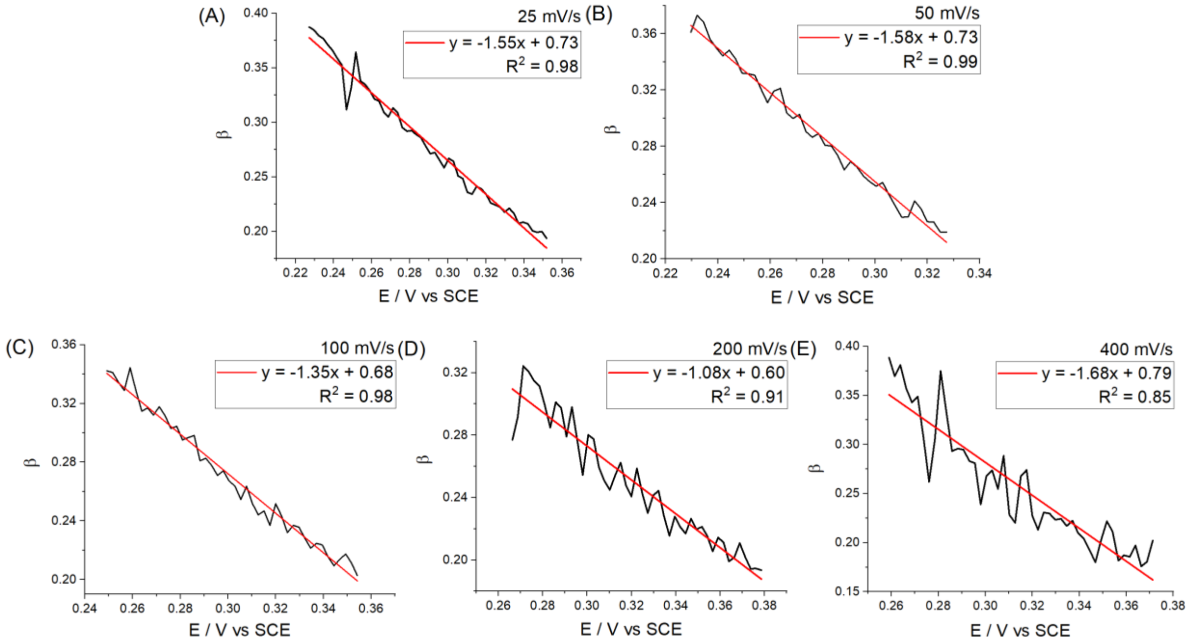

Figure 4.5. Plots of the measured anodic transfer coefficient β and the potential E in the range from 10% to 30% of the voltammetric peak current.

Table 4.1 Measured values of reorganization energy and formal potential for hydrazine oxidation at each scan rate on 0.1 M PBS

v / mV s^{-1}	25	50	100	200	400	Average

λ / eV	0.32	0.32	0.37	0.46	0.30	0.35 ± 0.07
E_f^0 / V	0.15	0.14	0.13	0.09	0.17	0.14 ± 0.03

Table 4.2 Measured average values of reorganization energy and formal potential for hydrazine oxidation in various electrolytes

Electrolyte	Initial concentration of N_2H_4 / mM	λ / eV	E_f^0 / V
0.1 M PBS	1.5	0.35 ± 0.07	0.14 ± 0.03
0.3 M PBS	1	0.44 ± 0.08	0.10 ± 0.04
0.5 M PBS	1	0.47 ± 0.06	0.08 ± 0.04
0.5 M PBS + 0.2 M KCl	1	0.44 ± 0.08	0.09 ± 0.05

Clearly the oxidation of hydrazine is not controlled by the Butler-Volmer (BV) kinetics but the sMH. This is primarily due to the fact that the reorganisation energy is sufficiently small that the differences between BV and sMH become apparent; this low value in turn might arise if the hydrazine molecule and the corresponding radical cation have a similar structure (bond lengths and angles) and solvation. Note that the formal potential applies to the thermodynamics of the first electron transfer assumed to be rate-determining, and not the overall 4 electron process. Note also that the inferred formal potential is highly approximate not least since it assumes that symmetric MH theory operates and that the transfer coefficient at zero over-potential is exactly 0.5.

It is also noteworthy that the re-organisation energy is rather low as compared to some outer sphere redox couples as analysed via the MH theory, as summarised in the Table A4.2 in the Appendix Section A4.2. Perusal of Eq. (1.53) shows that it is this low value, which amplifies the Marcusian effects and leads to the drawn out behaviour of the observed voltammetric waves. Moreover the inappropriate application of BV kinetics explains the diversity of the values of the oxidative transfer coefficient reported in the literature and highlighted in the Table A4.1. It was also highlighted that the literatures report a wide diversity of diffusion coefficients, however the method of data analysis used to infer the MH character of the electron transfer is independent of any value for the diffusion coefficient. Furthermore the range of literature values can be appreciated by exploring, via simulation, the effect of the reorganization energy for a fixed diffusion coefficient on the peak current for a slow k_0 value of 10^{-6} cm/s. An arbitrary value of 10^{-5} cm^2/s was selected for the diffusion coefficient given the large range of literature values (see Table A4.1). As depicted in Figure 4.6, the magnitude of the peak current significantly increases with the rise of the reorganization energy, and the linearity between the peak current and square scan rate is strongly associated with λ due to the asymptotic behaviour of sMH kinetics. As λ increases, the sMH theory tends to collapse into the BV. However for the value of the reorganization energy inferred above for the hydrazine oxidation system it is evident that plots of limiting current versus the square root of scan rate cannot be expected to quantitatively follow the Randles-Sevcik equation:

$$I_p = 2.99\times10^5 n\beta^{1/2}S[A]D_A^{\ 1/2}v^{1/2} \tag{4.10}$$

In this equation n is the number of electrons transferred[30], and is derived for a fully irreversible process following Butler-Volmer kinetics with a potential independent value of the transfer coefficient. This inapplicability in part explains the range of diffusion coefficients in the literature as well as the range of single transfer coefficient values reported. Note that if sMH rather than BV kinetics operates then a rigorous linear dependence of the peak current in the square root of scan rate is not expected[31] although the deviation is typically not great.

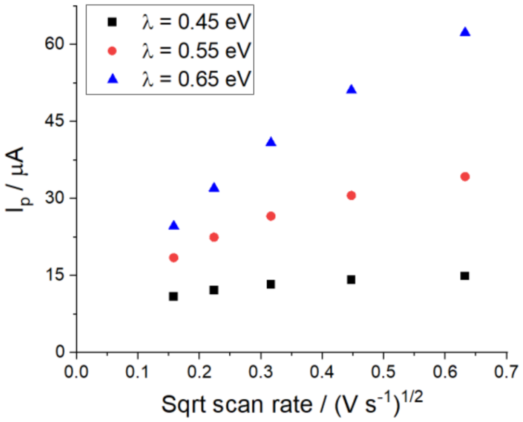

Figure 4.6. Plots of theoretical oxidative peak current and square root of scan rate from the simulation at a planar macrodisc electrode (diameter: 3 mm) using symmetric Marcus-Hush model for studying the effect of λ on the peak current. Reaction mechanism: $A-4e=B$. Parameters: E_f^0 $=0$ V; λ $=0.45$, 0.55 and 0.65 eV; $k_0=10^{-6}$ cm/s for the rate-determining electron transfer step; $[A]$ $=1.5$ mM and $[B]$ $=0$; D_A $=$ D_B $=1\times10^{-5}$ cm^2/s; ν $=100$ mV/s.

4.4 Conclusions

In this chapter, the *intrinsic* electron transfer kinetics of the hydrazine oxidation reaction was investigated on the Glassy Carbon electrode in 0.1 M PBS (pH 9). Tafel analysis for the voltammetry on the GC electrode reveals a negatively linear correlation between the anodic transfer coefficient and the potential, deviating distinctly from the well-recognized Butler-Volmer theory. The symmetric Marcus-Hush theory was adopted to describe the voltammetry. The reorganization energy was estimated to be 0.35 ± 0.07 eV from the relationship $\beta=\frac{\lambda+FE_f^0}{2\lambda}-\frac{F}{2\lambda}E$. The potential dependence of the transfer coefficient and the inapplicability of the Randles-Sevcik equation in the fully irreversible Butler-Volmer limit may explain in part the diversity of values for the transfer and diffusion coefficients present in the literature.

Appendix

Section A4.1: Literature data reported for the hydrazine oxidation

Table A4.1 Literature data reported for the hydrazine oxidation

Electrode	Electrolyte	pH	Method	D (cm^2/s)	β	Ref.
Pt microdisc electrode	0.1 M $HClO_4$	1	RDE voltammetry	1.40E-5	/	[32]
Pd nanoparticles decorated poly-3,4-ethylenedioxythiophene	0.2 M PBS	6.9	RDE voltammetry	1.20E-5	0.27	[33]
Pd nanoparticles decorated poly-3,4-ethylenedioxythiophene	0.2 M PBS	6.9	RDE voltammetry	1.20E-5	0.28	[34]
Pd nanoparticles decorated gaur gum	0.1 M PBS	7	Chronoamperometry	2.83E-6	0.67	[35]
Pd nanoparticles decorated ethylenediamine cellulose	0.1 M PBS	7	Chronoamperometry	2.30E-5	/	[36]
Pd-Au nanoparticles	0.1 M PBS	7	Chronoamperometry	2.61E-5	0.46	[37]
Pd nanoparticles decorated multiwalled carbon nanotubes	0.1 M PBS	7	Chronoamperometry	1.10E-5	0.55	[38]
Au nanoparticles decorated polypyrrole nanowire	0.1 M PBS	7	Chronoamperometry	2.50E-5	0.48	[39]
Au nanoparticles decorated TiO_2 nanotubes	0.1 M PBS	7	Chronoamperometry	4.10E-5	0.21	[40]
Au nanoparticles decorated multiwalled carbon nanotubes	0.1 M PBS	7	Chronoamperometry	2.05E-5	0.59	[41]
Hematoxylin multi-wall carbon nanotubes	0.1 M PBS	7	Chronoamperometry	4.58E-6	0.55	[42]
Co(II) complex multi-wall carbon nanotube	0.1 M PBS	7	Chronoamperometry	4.50E-6	0.53	[43]
p-aminophenol-modified multiwall carbon nanotubes	0.1 M PBS	7	Chronoamperometry	9.50E-6	0.30	[44]
rGO-Co_3O_4@Au nanocomposite	0.1 M PBS	7.2	Chronoamperometry	7.82E-7	/	[45]
Au nanoparticles decorated choline film	0.1 M PBS	7.4	Chronoamperometry	2.46E-5	0.50	[46]
Au nanoparticles decorated single-walled carbon nanohorns film	0.1 M PBS	7.4	Chronoamperometry	4.43E-6	/	[47]
Au nanocage decorated graphene	0.1 M PBS	7.4	Chronoamperometry	2.32E-6	0.54	[48]
Chlorogenic acid	0.15 M PBS	7.5	Chronoamperometry	8.20E-6	0.45	[49]
Curcumin multi-wall carbon nanotubes	0.5 M PBS	8	Chronoamperometry	2.45E-6	0.45	[50]
Carbon nanotubes and terpyridine manganese(II) complex	0.1 M PBS	8	RDE voltammetry	1.54E-6	0.60	[51]
Pt rotating disk electrode	0.05 PBS	8	RDE voltammetry	6.40E-6	/	[52]
Porous Au membranes	0.1 M PBS	8.5	Chronoamperometry	1.65E-5	/	[53]
Overoxidized polypyrrole (OPPy) modified glassy carbon	0.1 M ABS	9	Chronoamperometry	3.10E-5	0.46	[54]
Reduced graphene sheets	0.1 M KOH	13	Chronoamperometry	2.20E-5	0.48	[28]
Copper nanotubes on graphene paper	0.1 M KOH	13	Chronocoulometry	2.10E-5	0.50	[55]
Copper (hydr)oxide modified copper electrode	0.1 M NaOH	13	Chronoamperometry	3.00E-5	0.51	[56]

Ni(II)-baicalein complex modified multi-wall carbon nanotube paste electrode	0.1 M NaOH	13	Chronoamperometry	3.58E-5	0.35	[57]
(5,10,15,20-tetra(4-sulfophenyl) porphyrin-nickel	0.1 M NaOH	13	Chronoamperometry	4.19E-6	/	[58]
Ni-based ternary alloy electrode (G/NiCuCo)	0.1 M NaOH	13	Chronoamperometry	6.28E-6	/	[59]

Section A4.2: Literature values of the outer-sphere reorganization energy values

Table A4.2 Literature values of the outer-sphere reorganization energy for redox couples

Redox species	O_2^-/O_2	O_3/O_3^-	N_3/N_3^-	CO_2/CO_2^-	SO_2/SO_2^-
λ_{outer} / eV	2.30	2.02	1.93	2.22	2.20
Ref.	[60]	[60]	[60]	[60]	[60]
Redox species	ClO_2/ClO_2^-	NO^+/NO	NO_2^+/NO_2	$Fe^{2+}/^{3+}$	$Cr^{2+}/^{3+}$
λ_{outer} / eV	2.01	2.11	1.55	1.50	1.52
Ref.	[60]	[61]	[62]	[63]	[63]
Redox species	$Mn^{2+}/^{3+}$	$V^{2+}/^{3+}$	$Co^{2+}/^{3+}$	$Fe(phen)^{2+/3+}$	$Ru(bpy)_3^{2+/3+}$
λ_{outer} / eV	1.51	1.49	1.52	0.57	0.57
Ref.	[63]	[63]	[63]	[64]	[64]
Redox species	$Ru(en)_3^{2+/3+}$	$Ru(NH_3)_6^{2+/3+}$	$Fe(CN)_6^{4-/3-}$	$Ru(H_2O)_6^{2+/3+}$	$Cr(OH_2)_6^{2+/3+}$
λ_{outer} / eV	0.92	1.16	0.86	1.20	1.04
Ref.	[64]	[64]	[64]	[64]	[65]

References

[1] R. Miao, L. Chen, R.G. Compton, Electro-oxidation of hydrazine shows Marcusian electron transfer kinetics, Science China Chemistry, 64 (2021) 322-329.

[2] A. Furst, R.C. Berlo, S. Hooton, Hydrazine as a Reducing Agent for Organic Compounds (Catalytic Hydrazine Reductions), Chemical Reviews, 65 (1965) 51-68.

[3] Z. Lu, M. Sun, T. Xu, Y. Li, W. Xu, Z. Chang, Y. Ding, X. Sun, L. Jiang, Superaerophobic electrodes for direct hydrazine fuel cells, Advanced Materials, 27 (2015) 2361-2366.

[4] T. Wang, Q. Wang, Y. Wang, Y. Da, W. Zhou, Y. Shao, D. Li, S. Zhan, J. Yuan, H. Wang, Atomically Dispersed Semimetallic Selenium on Porous Carbon Membrane as an Electrode for Hydrazine Fuel Cells, Angewandte Chemie International Edition, 58 (2019) 13466-13471.

[5] G. Feng, Y. Kuang, P. Li, N. Han, M. Sun, G. Zhang, X. Sun, Single crystalline ultrathin nickel–cobalt alloy nanosheets array for direct hydrazine fuel cells, Advanced Science, 4 (2017) 1600179.

[6] B. Wang, X. Cao, The anodic oxidation of hydrazine on glassy carbon electrode, Electroanalysis, 4 (1992) 719-724.

[7] R. Baron, B. Šljukić, C. Salter, A. Crossley, R.G. Compton, Development of an Electrochemical Sensor Nanoarray for Hydrazine Detection Using a Combinatorial Approach, Electroanalysis, 19 (2007) 1062-1068.

[8] L. Xiong, R.G. Compton, Amperometric gas detection: A review, International Journal of Electrochemical Science, 9 (2014) 7152-7181.

[9] T.C. Bruice, J. Bruno, W.-S. Chou, Nucleophilic displacement reactions at the thiol-ester bond of δ-thiolvalerolactone, Journal of the American Chemical Society, 85 (1963) 1659-1669.

[10] J.H. Moreno, J.M. Diamond, Role of hydrogen bonding in organic cation discrimination by gallbladder epithelium, Nature, 247 (1974) 368-369.

[11] E. Hayon, M. Simic, Intermediates produced from the one-electron oxidation of hydrazine. Evidence for the formation and decay of tetrazane and triazene, Journal of the American Chemical Society, 94 (1972) 42-47.

[12] N. Korovin, B. Yanchuk, Hydrogen sorption by palladium in hydrazine electro-oxidation, Electrochimica Acta, 15 (1970) 569-580.

[13] V. Rosca, M. Duca, M.T. de Groot, M.T. Koper, Nitrogen cycle electrocatalysis, Chemical Reviews, 109 (2009) 2209-2244.

[14] C.C. Kocak, A. Altin, B. Aslisen, S. Koçak, Electrochemical preparation and characterization of gold and platinum nanoparticles modified poly (taurine) film electrode and its application to hydrazine determination, International Journal of Electrochemical Science, 11 (2016) 233-249.

[15] G. Maduraiveeran, R. Ramaraj, Gold nanoparticle-based sensing platform of hydrazine, sulfite, and nitrite for food safety and environmental monitoring, Journal of Analytical Science and Technology, 8 (2017) 1-10.

[16] S. Koçak, B. Aslışen, Hydrazine oxidation at gold nanoparticles and poly (bromocresol purple) carbon nanotube modified glassy carbon electrode, Sensors and Actuators B: Chemical, 196 (2014) 610-618.

[17] C. Batchelor-McAuley, E. Kätelhön, E.O. Barnes, R.G. Compton, E. Laborda, A. Molina, Recent advances in voltammetry, ChemistryOpen, 4 (2015) 224-260.

[18] C.E. Chidsey, Free energy and temperature dependence of electron transfer at the metal-

electrolyte interface, Science, 251 (1991) 919-922.

[19] E. Laborda, M.C. Henstridge, C. Batchelor-McAuley, R.G. Compton, Asymmetric Marcus–Hush theory for voltammetry, Chemical Society Reviews, 42 (2013) 4894-4905.

[20] S.W. Feldberg, Implications of Marcus−Hush theory for steady-state heterogeneous electron transfer at an inlaid disk electrode, Analytical Chemistry, 82 (2010) 5176-5183.

[21] Z. Ding, B.M. Quinn, A.J. Bard, Kinetics of heterogeneous electron transfer at liquid/liquid interfaces as studied by SECM, The Journal of Physical Chemistry B, 105 (2001) 6367-6374.

[22] Y. Wang, E. Laborda, M.C. Henstridge, F. Martinez-Ortiz, A. Molina, R.G. Compton, The use of differential pulse voltammetries to discriminate between the Butler–Volmer and the simple Marcus–Hush models for heterogeneous electron transfer: The electro-reduction of europium (III) in aqueous solution, Journal of Electroanalytical Chemistry, 668 (2012) 7-12.

[23] E. Laborda, M.C. Henstridge, R.G. Compton, Asymmetric Marcus theory: Application to electrode kinetics, Journal of Electroanalytical Chemistry, 667 (2012) 48-53.

[24] M. Rudolph, D.P. Reddy, S.W. Feldberg, A simulator for cyclic voltammetric responses, Analytical Chemistry, 66 (1994) 589A-600A.

[25] R.G. Compton, C.E. Banks, Understanding Voltammetry, World Scientific, 2018.

[26] N. Elgrishi, K.J. Rountree, B.D. McCarthy, E.S. Rountree, T.T. Eisenhart, J.L. Dempsey, A practical beginner's guide to cyclic voltammetry, Journal of Chemical Education, 95 (2018) 197-206.

[27] C. Batchelor-McAuley, E. Kätelhön, E.O. Barnes, R.G. Compton, E. Laborda, A. Molina, Recent advances in voltammetry, ChemistryOpen, 4 (2015) 224.

[28] Y. Wang, Y. Wan, D. Zhang, Reduced graphene sheets modified glassy carbon electrode for electrocatalytic oxidation of hydrazine in alkaline media, Electrochemistry Communications, 12 (2010) 187-190.

[29] D. Li, C. Lin, C. Batchelor-McAuley, L. Chen, R.G. Compton, Tafel analysis in practice, Journal of Electroanalytical Chemistry, 826 (2018) 117-124.

[30] R. Miao, L. Chen, L. Shao, B. Zhang, R.G. Compton, Electron transfer to decorated graphene oxide particles, Angewandte Chemie International Edition, 58 (2019) 12549-12552.

[31] M.C. Henstridge, E. Laborda, E.J. Dickinson, R.G. Compton, Redox systems obeying Marcus–Hush–Chidsey electrode kinetics do not obey the Randles–Ševčík equation for linear sweep voltammetry, Journal of Electroanalytical Chemistry, 664 (2012) 73-79.

[32] C.-H. Chen, L. Jacobse, K. McKelvey, S.C. Lai, M.T. Koper, P.R. Unwin, Voltammetric scanning electrochemical cell microscopy: dynamic imaging of hydrazine electro-oxidation on platinum electrodes, Analytical Chemistry, 87 (2015) 5782-5789.

[33] V.V. Kondratiev, T.A. Babkova, E.G. Tolstopjatova, PEDOT-supported Pd nanoparticles as a catalyst for hydrazine oxidation, Journal of Solid State Electrochemistry, 17 (2013) 1621-1630.

[34] T. Babkova, V. Kondratiev, D. Shevaldysheva, Oxidation of hydrazine on poly-3, 4-ethylenedioxythiophene polymer films with inclusions of palladium nanoparticles, Russian Journal of Electrochemistry, 49 (2013) 259-264.

[35] P.K. Rastogi, V. Ganesan, S. Krishnamoorthi, Palladium nanoparticles decorated gaur gum based hybrid material for electrocatalytic hydrazine determination, Electrochimica Acta, 125 (2014) 593-600.

[36] H. Ahmar, S. Keshipour, H. Hosseini, A.R. Fakhari, A. Shaabani, A. Bagheri, Electrocatalytic oxidation of hydrazine at glassy carbon electrode modified with ethylenediamine cellulose

immobilized palladium nanoparticles, Journal of Electroanalytical Chemistry, 690 (2013) 96-103.

[37] M. Shamsipur, Z. Karimi, M.A. Tabrizi, A. Shamsipur, Electrocatalytic Determination of Traces of Hydrazine by a Glassy Carbon Electrode Modified with Palladium-Gold Nanoparticles, Electroanalysis, 26 (2014) 1994-2001.

[38] B. Haghighi, H. Hamidi, S. Bozorgzadeh, Sensitive and selective determination of hydrazine using glassy carbon electrode modified with Pd nanoparticles decorated multiwalled carbon nanotubes, Analytical and Bioanalytical Chemistry, 398 (2010) 1411-1416.

[39] J. Li, X. Lin, Electrocatalytic oxidation of hydrazine and hydroxylamine at gold nanoparticle—polypyrrole nanowire modified glassy carbon electrode, Sensors and Actuators B: Chemical, 126 (2007) 527-535.

[40] M. Hosseini, M.M. Momeni, M. Faraji, Electro-oxidation of hydrazine on gold nanoparticles supported on TiO_2 nanotube matrix as a new high active electrode, Journal of Molecular Catalysis A: Chemical, 335 (2011) 199-204.

[41] H. Hamidi, S. Bozorgzadeh, B. Haghighi, Amperometric hydrazine sensor using a glassy carbon electrode modified with gold nanoparticle-decorated multiwalled carbon nanotubes, Microchimica Acta, 184 (2017) 4537-4543.

[42] H.R. Zare, N. Nasirizadeh, Hematoxylin multi-wall carbon nanotubes modified glassy carbon electrode for electrocatalytic oxidation of hydrazine, Electrochimica Acta, 52 (2007) 4153-4160.

[43] A. Benvidi, P. Kakoolaki, H.R. Zare, R. Vafazadeh, Electrocatalytic oxidation of hydrazine at a Co (II) complex multi-wall carbon nanotube modified carbon paste electrode, Electrochimica Acta, 56 (2011) 2045-2050.

[44] A.A. Ensafi, M. Lotfi, H. Karimi-Maleh, New modified-multiwall carbon nanotubes paste electrode for electrocatalytic oxidation and determination of hydrazine using square wave voltammetry, Chinese Journal of Catalysis, 33 (2012) 487-493.

[45] M.M. Shahid, P. Rameshkumar, W.J. Basirunc, U. Wijayantha, W.S. Chiu, P.S. Khiew, N.M. Huang, An electrochemical sensing platform of cobalt oxide@ gold nanocubes interleaved reduced graphene oxide for the selective determination of hydrazine, Electrochimica Acta, 259 (2018) 606-616.

[46] J. Li, H. Xie, L. Chen, A sensitive hydrazine electrochemical sensor based on electrodeposition of gold nanoparticles on choline film modified glassy carbon electrode, Sensors and Actuators B: Chemical, 153 (2011) 239-245.

[47] S. Zhao, L. Wang, T. Wang, Q. Han, S. Xu, A high-performance hydrazine electrochemical sensor based on gold nanoparticles/single-walled carbon nanohorns composite film, Applied Surface Science, 369 (2016) 36-42.

[48] S. Daemi, A.A. Ashkarran, A. Bahari, S. Ghasemi, Fabrication of a gold nanocage/graphene nanoscale platform for electrocatalytic detection of hydrazine, Sensors and Actuators B: Chemical, 245 (2017) 55-65.

[49] S. Golabi, H. Zare, Electrocatalytic oxidation of hydrazine at a chlorogenic acid (CGA) modified glassy carbon electrode, Journal of Electroanalytical Chemistry, 465 (1999) 168-176.

[50] L. Zheng, J.-f. Song, Curcumin multi-wall carbon nanotubes modified glassy carbon electrode and its electrocatalytic activity towards oxidation of hydrazine, Sensors and Actuators B: Chemical, 135 (2009) 650-655.

[51] M. Kamyabi, O. Narimani, H.H. Monfared, Electrocatalytic oxidation of hydrazine using glassy carbon electrode modified with carbon nanotube and terpyridine manganese (II) complex, Journal of Electroanalytical Chemistry, 644 (2010) 67-73.

[52] S.E. Kleijn, B. Serrano-Bou, A.I. Yanson, M.T. Koper, Influence of hydrazine-induced aggregation on the electrochemical detection of platinum nanoparticles, Langmuir, 29 (2013) 2054-2064.

[53] X. Yan, F. Meng, S. Cui, J. Liu, J. Gu, Z. Zou, Effective and rapid electrochemical detection of hydrazine by nanoporous gold, Journal of Electroanalytical Chemistry, 661 (2011) 44-48.

[54] M.R. Majidi, A. Jouyban, K. Asadpour-Zeynali, Electrocatalytic oxidation of hydrazine at overoxidized polypyrrole film modified glassy carbon electrode, Electrochimica Acta, 52 (2007) 6248-6253.

[55] H. Gao, Y. Wang, F. Xiao, C.B. Ching, H. Duan, Growth of copper nanocubes on graphene paper as free-standing electrodes for direct hydrazine fuel cells, The Journal of Physical Chemistry C, 116 (2012) 7719-7725.

[56] G. Karim-Nezhad, R. Jafarloo, P.S. Dorraji, Copper (hydr) oxide modified copper electrode for electrocatalytic oxidation of hydrazine in alkaline media, Electrochimica Acta, 54 (2009) 5721-5726.

[57] L. Zheng, J.-f. Song, Ni (II)–baicalein complex modified multi-wall carbon nanotube paste electrode toward electrocatalytic oxidation of hydrazine, Talanta, 79 (2009) 319-326.

[58] S. Kazemi, B. Hosseinzadeh, S. Zakavi, Electrochemical fabrication of conducting polymer of Ni-porphyrin as nano-structured electrocatalyst for hydrazine oxidation, Sensors and Actuators B: Chemical, 210 (2015) 343-348.

[59] M. Jafarian, T. Rostami, M. Mahjani, F. Gobal, A low cost and highly active non-noble alloy electrocatalyst for hydrazine oxidation based on nickel ternary alloy at the surface of graphite electrode, Journal of Electroanalytical Chemistry, 763 (2016) 134-140.

[60] L.E. Bennett, P. Warlop, Electron transfer to ozone: outer-sphere reactivities of the ozone/ozonide and related non-metal redox couples, Inorganic Chemistry, 29 (1990) 1975-1981.

[61] J.P. Sandall, The mechanism of aromatic nitration in solution: Marcus theory and semiempirical molecular orbital calculations on NO_2^+ and NO^+ as one-electron oxidants, Journal of the Chemical Society, Perkin Transactions 2, (1992) 1689-1693.

[62] T. Lund, L. Eberson, Experimental determination of the reorganization energy of the NO_2^+/NO_2 redox couple. Comparison withtheory, Journal of the Chemical Society, Perkin Transactions 2, (1997) 1435-1444.

[63] K.M. Rosso, J.R. Rustad, Ab initio calculation of homogeneous outer sphere electron transfer rates: Application to $M(OH_2)_6^{3+/2+}$ redox couples, The Journal of Physical Chemistry A, 104 (2000) 6718-6725.

[64] P. Delahay, Reply to "contribution of inner-sphere reorganization in electron transfer reaction in solution" by SUM Khan and JO'M. Bockris, Chemical Physics Letters, 99 (1983) 87-88.

[65] N. Sutin, M.J. Weaver, E.L. Yee, Correlations between outer-sphere self-exchange rates and reaction entropies for some simple redox couples, Inorganic Chemistry, 19 (1980) 1096-1098.

Chapter 5

Hydrazine Oxidation at Glassy Carbon: Self-inhibition

The last chapter reveals that hydrazine oxidation shows Marcusian kinetics at glassy carbon surface, not following the well-recognised Butler-Volmer theory. The electro-oxidation of hydrazine is investigated further in this chapter at the same glassy carbon surface over a wide range of both pH and of unbuffered conditions. It is shown that hydrazine molecules are only electro-active in their un-protonated form, N_2H_4, whereas the protonated species $N_2H_5^+$ is electro-inactive. The oxidation of N_2H_4 releases four protons per molecule which diffuse away from the electrode and rapidly (on the voltammetric timescale) protonate unreacted N_2H_4 molecules diffusing to the electrode converting them into the electro-inactive form, $N_2H_5^+$; the reaction is thus *self-inhibiting* and the currents flowing are significantly reduced compared to those expected for a simple electrolytic conversion to an extent reflecting the pH and buffer content of the solution local to the electrode. The local pH in turn is controlled partly by the quantity of protons released electrolytically. The self-inhibition is modelled by solving the relevant transport equations with coupled homogeneous chemical kinetics, utilising Marcus-Hush electron transfer, giving predicted reduced currents reflecting the pK_a and kinetics of the $N_2H_4/N_2H_5^+$ equilibrium in excellent agreement with experimental voltammetric waveshapes. The work of Chapter 5 has been published in the journal *The Journal of Physical Chemistry Letters*[1], and was carried out under the supervision of Prof. Richard G. Compton (University of Oxford).

5.1 Introduction

The fundamental electrochemistry of hydrazine is fascinating since it presents two challenges. The first of these relates to the unusual voltammetry seen, even at carbon electrodes,[2] in which the voltammetric waves increase only gradually with potential in contrast to the predictions of the semi-empirical Butler-Volmer theory[3, 4] widely used to interpret electrode kinetic data, as reported in Chapter 4.[5] Note that there is either zero or only very weak adsorption of hydrazine molecules at carbon surfaces.[6] The second relates to the magnitude of the currents flowing which, at first sight, suggest either the passage of less than four electrons per molecule of hydrazine or that the latter has a pathologically low diffusion coefficient in aqueous solution. Indeed a review of the literature of the electrochemically determined diffusion coefficients of hydrazine (Table A4.1, Chapter 4) showed values ranging for different media implausibly over a factor of ca. 50 with many values much lower than expected for a molecule of the size of hydrazine.[7-12]

In Chapter 4, the first of these challenges, namely the voltammetric wave shape, was addressed[2] under conditions where N_2H_4 is the sole solution phase species and the effect shown to originate in a potential dependent transfer coefficient which in turn was shown to result from the operation of Marcus-Hush (as opposed to Butler-Volmer) electron transfer kinetics[13, 14] with a rather low re-organisation energy controlling the first electron transfer and which was seen to be rate determining, at least at carbon electrodes.

In Chapter 5 we address the second and greater challenge noting that the oxidation of hydrazine produces protons which on account of the basicity of the molecule may protonate N_2H_4 forming $N_2H_5^+$ in aqueous solution. Thus we hypothesise that the protons released in the electro-oxidation can interfere with the electrode reaction by altering the chemical speciation adjacent to the electrode by altering the local solution pH. Specifically we suggest that the local formation of increased quantities of acid and hence of the $N_2H_5^+$ cation changes the voltammetric response because of the contrasting electrochemical activity of the cation in comparison with the precursor N_2H_4. In particular, on the basis of the voltammetry over a range of pH values and buffer compositions, the former is shown not to be electroactive at carbon electrodes in contrast to the latter. Detailed modelling, based on Marcusian electron transfer kinetics, and the homogeneous chemistry of the $N_2H_4/N_2H_5^+$ acid-base equilibrium, both thermodynamic and kinetic, are shown to validate this hypothesis.

5.2 Experimental

An aqueous solution of 1.5 mM hydrazine supported by 0.1 M KNO_3 was prepared, the pH of which was measured to be 9.7. Analogous hydrazine solutions of pH 2.0 and pH 7.0 were prepared via the addition of tiny amounts of HNO_3 to adjust the pH. A phosphate buffer solution (0.1 M PBS, pH 7.0) with 1.5 mM hydrazine was used for further studies. A digital sensION^{TM}+ PH31 pH meter (HACH, Colorado, USA) was used for pH measurements and calibrated before each measurement. Cyclic voltammetry (CV) measurements were then performed using the prepared solutions after degassing with a N_2 stream for 15 minutes. Control experiments were conducted without hydrazine.

5.3 Results and Discussion

In the following we consider the voltammetry of hydrazine in aqueous solutions of different pH. It is helpful therefore to consider first the speciation of hydrazine noting the pK_{a1} value of ca. 8.0[15-18] and the pK_{a2} of ca. -1.0[19-21] at 298 K which correspond to the following chemical equilibria

$$N_2H_5^+ \rightleftarrows N_2H_4 + H^+ \tag{5.1}$$

$$N_2H_6^{2+} \rightleftarrows N_2H_5^+ + H^+ \tag{5.2}$$

The speciation of hydrazine as a function of pH in pure water is shown in the Appendix Section A5.1, Figure A5.1. In practice the exact speciation at any pH may likely also reflect to some small extent the total electrolyte concentration in the solution, the so-called salt effect;[22, 23] this is considered further below.

The oxidation of hydrazine was first studied electrochemically at a glassy carbon electrode (GCE) in solutions of 1.5 mM hydrazine supported by 0.1 M KNO_3 which had been adjusted to pH 2.0 or pH 7.0 by the addition of tiny amounts of 1 M HNO_3. Note that the dominant species in the solution of pH 2.0 is almost 100% hydrazinium cation $N_2H_5^+$ as shown in Figure A5.1. As depicted in Figure 5.1A (pH 2.0), there are no additional oxidative features seen in the voltammogram (solid line) as compared to the also featureless control experiment conducted in the absence of hydrazine (dash line). This clearly shows that there is no direct oxidation of $N_2H_5^+$ on the surface of the GCE. In contrast, Figure 5.1B (pH 7.0) shows a fully electrochemically irreversible wave[24] with a peak at ca. 0.36 V vs SCE of a current of 2.0 μA (solid line); no voltammetric features were observed in the absence of hydrazine (dash line). It is deduced that the anodic current results from the oxidation of the unprotonated hydrazine N_2H_4 given the 'inactivity' of $N_2H_5^+$ and the negligible concentration of $N_2H_6^{2+}$ in solution (Figure A5.1).

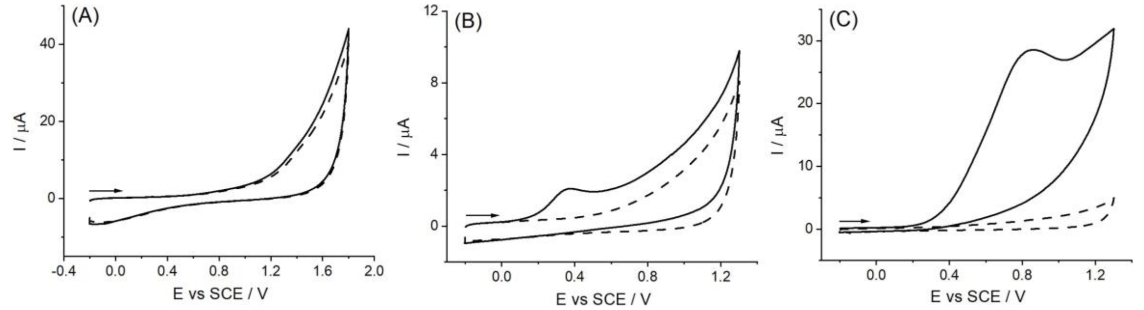

Figure 5.1. Cyclic voltammetry (solid line) at a GCE of 1.5 mM hydrazine supported by the electrolytes: (A) 0.1 M KNO_3, pH 2 (see text), (B) 0.1 M KNO_3 of pH 7 (see text) and (C) 0.1 M PBS of pH 7. The control experiments without hydrazine are shown as the dash lines in each case. Scan rate: 50 mV/s. The arrows indicate the start potential of the voltammetric scans and the direction of sweep. The voltammograms at different scan rates (25 - 400 mV/s) are provided in the Appendix Section A5.2.

It is widely recognized that the oxidation of N_2H_4 is a four-electron transfer process with the release of protons and forming nitrogen, N_2.[25-27] The generation of protons necessarily changes the local pH (of the solution close to the surface of the GCE). To investigate the effect of the local pH variation on the reaction process, 1.5 mM hydrazine supported by phosphate buffer solution (PBS) with a total concentration of 0.1 M was utilized as the electrolyte for comparison and contrast. The voltammograms were recorded and are presented in Figure 5.1C where a clear oxidative peak is observed at ca. 0.85 V vs SCE with a current of ca. 28 μA. Note that there is a dramatic increase in peak current compared to that in Figure 5.1B, when, as in Figure 5.1C, the local proton concentration is largely fixed by the buffer which can combine with the protons released from the electrolysis. The observed potential shift is likely ascribed to the change in the local composition and hence of mass transport of the analyte as the buffer system is introduced. It is inferred that in the KNO_3 electrolyte, the protons released from the oxidation of N_2H_4 and diffusing away from the electrode likely combine with the incoming N_2H_4 molecules diffusing to the electrode to form the 'inactive' $N_2H_5^+$ that, as shown above, is not oxidised at the GCE. This gives rise to the very small anodic current seen in the unbuffered solution (Figure 5.1B) resulting from the N_2H_4 which does not become protonated as it diffuses to the electrode. In other words, the process of hydrazine oxidation on the surface of the GCE is limited to a great extent by the synchronous *self-inhibition* effect from the combination of N_2H_4 molecules and oxidation-produced H^+. This finding is of great significance to all practical uses employing the electro-oxidation of hydrazine, for example and especially in amperometric sensors for this toxic material[28, 29] as well as the correct quantitative interpretation of hydrazine electrochemistry at all electrodes of any chemical composition.

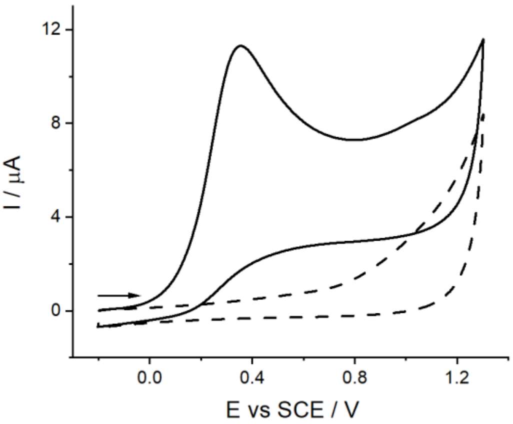

Figure 5.2. Cyclic voltammetry (solid line) at a GCE of 1.5 mM hydrazine supported by 0.1 M KNO_3 of pH 9.7. The control experiment without hydrazine is presented as the dash line. Scan rate: 50 mV/s. The arrow indicates the start potential and direction of the voltammetric scan. The voltammograms at different scan rates (25 - 400 mV/s) are provided in the Appendix Section A5.3.

To probe into the *intrinsic* electron transfer of hydrazine oxidation and the homogeneous dynamics between the redox active N_2H_4 and the redox inactive $N_2H_5^+$, cyclic voltammetry was conducted at a GCE in a system where 1.5 mM hydrazine was solely supported by 0.1 M KNO_3, *without* the addition of any mineral acid or of buffer solution. The pH was determined to be 9.7 as mentioned above. This value implies a pK_a value of 8.3 which compares with the reported value of ~8.0 for pure water at the same temperature (298K)[15-18] implying a small thermodynamic salt effect due to the dissolved KNO_3. The recorded anodic current, as displayed in Figure 5.2, is distinctly larger than that seen for (the acid adjusted) pH 7.0 (0.1 M KNO_3) in Figure 5.1B. The increase mainly results from the enhanced concentration of the electro-active N_2H_4 in bulk solution as seen in Figure A5.1. The current is however less than that expected for a simple diffusion-controlled oxidation of hydrazine reflecting the self-inhibition effect noted above.

DIGISIM is a well-respected commercial simulation software (BASI, West Lafayette, USA) for cyclic voltammetry based on the fast implicit finite difference method invented by M Rudolph.[30, 31] This was utilized to facilitate the analysis of the hydrazine electro-oxidation reaction mechanism and to quantify the associated kinetics on the voltammetric waveshape, the peak currents and the inferred potential dependent transfer coefficient. A planar geometry was adopted in the simulation corresponding to the experimentally deployed macrodisc GCE of 3.0 mm in diameter under a transport regime dominated by linear diffusion.[32] The first electron transfer of the N_2H_4 oxidation process at pH 2 - 11 was found in our study[33] to be reported in Chapter 6 to be rate-determining via the nanoimpact technique. This rate determining step (rds) involves no release of protons, which are expelled in subsequent steps. Thus the rds was inferred in the case of carbon electrodes to involve the formation of the transient radical cation $N_2H_4^{\bullet+}$ on the surface of the electrode or in the solution. The hydrazinium cation $N_2H_5^+$ is not oxidised as mentioned above. Hence, the mechanism was proposed as follows:

$$N_2H_5^+ \rightleftarrows N_2H_4 + H^+ \tag{5.3}$$

$$N_2H_4 \xrightarrow{rds} N_2H_4^{\bullet+} + e^- \tag{5.4}$$

$$N_2H_4^{\bullet+} \xrightarrow{fast} N_2 + 4H^+ + 3e^- \tag{5.5}$$

where the equilibrium constant for the homogeneous chemical reaction was adopted from the experimentally determined pK_a value for 0.1 M KNO_3 aqueous solution as mentioned above and the homogeneous second order rate constant (M^{-1} s^{-1}) for reaction of protons with hydrazine was optimised to give the best fit between experiment and simulation. Independently measured[33] diffusion coefficients for N_2H_4 and $N_2H_5^+$ were used together with a literature value for the proton diffusion coefficient.[34, 35] Note that fixing the K_a value and the second order rate constant necessarily defines the first order rate constant for the dissociation of the hydrazinium cation. The electron transfer kinetics were assumed to be governed by Marcus-Hush theory in the light of the data presented in the Appendix Section A5.4 and our previous study[2] described in Chapter 4 which demonstrated that the Marcus-Hush theory[13, 14] was required to describe the hydrazine oxidation, instead of the potential independent transfer coefficient as assumed in the phenomenological Butler-Volmer kinetics[3, 4, 36]. The reorganization energy in the more physically based Marcus-Hush formalism reflects both solvent polarisation and internal molecular vibration. Accordingly the Marcusian kinetics was selected as the mathematical model in DIGISIM and the previously measured value of 0.35 eV used as the reorganisation energy. The details of the simulation are provided in the Appendix Section A5.5.

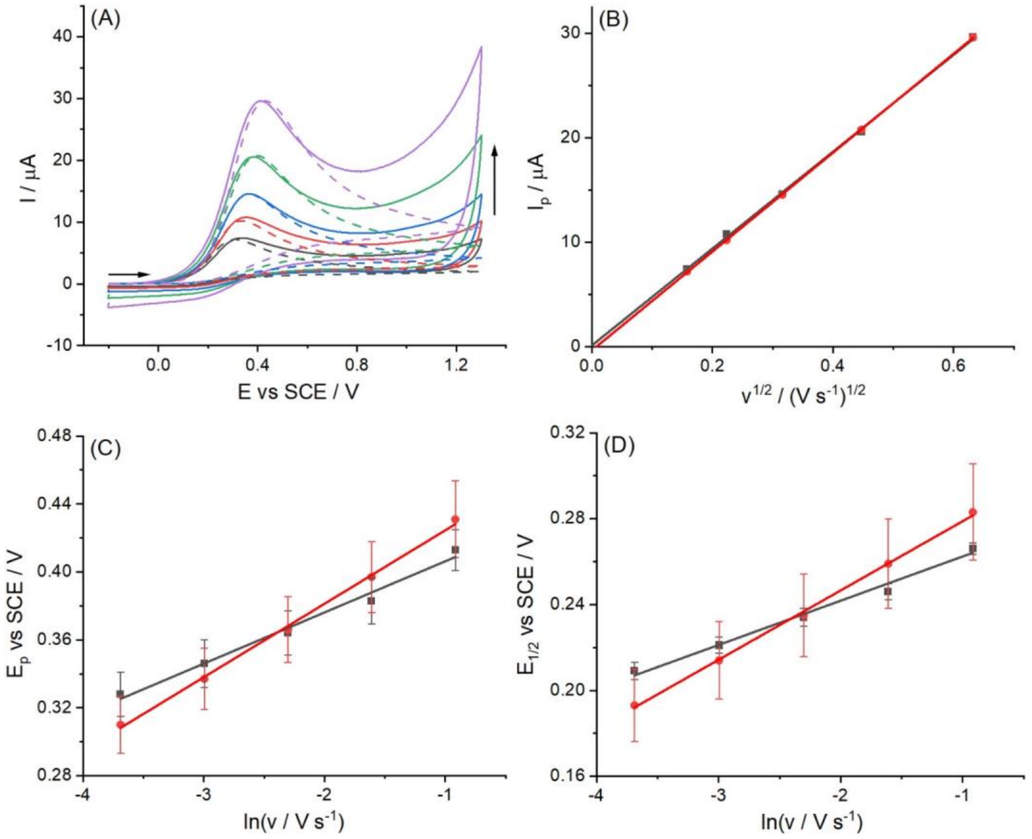

Figure 5.3. The comparison between the experimental and DIGISIM-simulated voltammetry at a GCE of 1.5 mM hydrazine supported by 0.1 M KNO_3 of pH 9.7: (A) the voltammograms (solid for experiment, dash for simulation); (B) the plot of I_p versus $v^{1/2}$; (C) the plot of E_p versus ln*v* and (D) $E_{1/2}$ versus ln*v* (black for experiment, red for simulation). Note that the experimental voltammograms are baseline-corrected. The transverse arrow indicates the start potential and direction of the voltammetric scan. The vertical arrow indicates increasing scan rates. Simulation parameters: initial concentrations of N_2H_4, $N_2H_5^+$ and H^+ are 1.44 mM, 0.06 mM and 2×10^{-10} M respectively; formal potential of $N_2H_4/N_2H_4^{\bullet+}$ is 0.14 V; reorganization energy is 0.35 eV; equilibrium constant of $N_2H_4/N_2H_5^+$ is 5.0×10^{-9} M; diffusion coefficients of N_2H_4 and $N_2H_5^+$ are 7.1×10^{-6} cm^2/s and 2.8×10^{-6} cm^2/s respectively; standard rate constant of the rds step is 4.5×10^{-5} cm/s; second order rate constant for the protonation of hydrazine is 1.1×10^5 M^{-1} s^{-1}; scan rates are 25/50/100/200/400 mV/s.

Figure 5.3A shows the favourable comparison between the experimental voltammograms and the simulated predictions of the above model (using exactly the same parameters) at scan rates in the range of 25 - 400 mV/s. A satisfactory fitting for the studied oxidative peak in terms of shape, size and position is observed for each scan rate. In particular the simulation captures the unusual 'drawn out' shape of the voltammetry which arises from the decrease of the transfer coefficient with potential; simulation using Butler-Volmer kinetics was unable to reproduce this feature. Note that the 'drawn out' shape (indicated in Figure A5.3) is distinguished from the typical electrochemically highly irreversible processes which display a much higher rate of increase of the current with potential.[2] Numerical information about current and potential are presented in the plots of I_p against $v^{1/2}$ (Figure 5.3B) as well as E_p (Figure 5.3C) and $E_{1/2}$ (Figure 5.3D) against ln*v*. Overall good consistency between experiment and theory is attained as is evident from the totality of the data presented in Figure 5.3. Finally the simulations allow the inference of a value of 0.14 V vs SCE for the standard electrode potential where this relates to the first and rate determining electron transfer

$$N_2H_4 \xrightarrow{rds} N_2H_4^{\bullet +} + e^- \tag{5.6}$$

This in turn allows an *approximate* estimation of the associated standard rate constant k_0 of $(4.5 \pm 1.0) \times 10^{-5}$ cm/s for the rate-determining step. Note that these numerical inferences presume the validity of the *symmetric* form of Marcus Hush theory and hence are subject to that important caveat. The slow k_0 is consistent with the full electrochemical irreversibility of hydrazine oxidation under the mass transport conditions prevailing.[37, 38]

5.4 Conclusions

In conclusion, the oxidation of hydrazine in solutions of around neutral pH and more generally in unbuffered media is shown to be an intrinsically self-inhibiting reaction in which the protons released in the course of the oxidation combine with the reactant to form cations of protonated hydrazine which are not electroactive at carbon electrodes. The reaction has been modelled using Marcus-Hush theory which quantitatively and fully accounts for the observed voltammetry provided the thermodynamics and kinetics of the protonation are considered.

Appendix

Section A5.1: Speciation of hydrazine as a function of pH in pure water

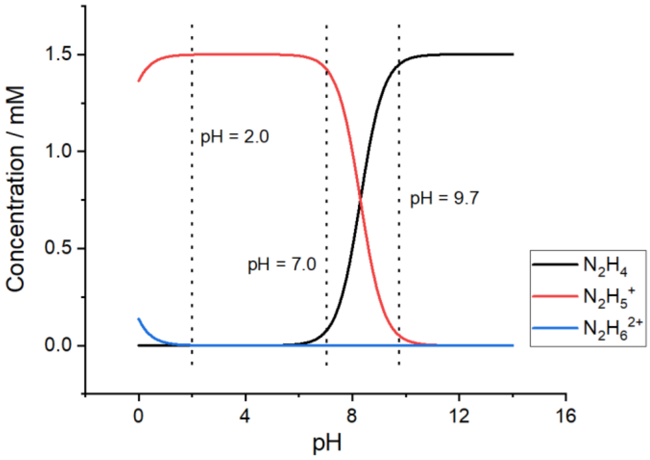

Figure A5.1. The speciation of hydrazine as a function of pH in pure water.

Section A5.2: Voltammograms in 0.1 M KNO3 (pH 2.0), 0.1 M KNO3 (pH 7.0) and 0.1 M PBS (pH 7.0)

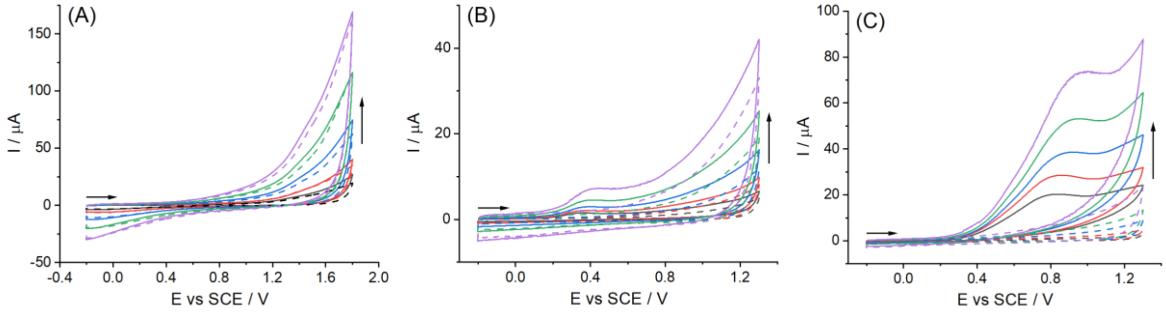

Figure A5.2. Cyclic voltammetry (solid line) at a GCE of 1.5 mM hydrazine supported by the electrolytes: (A) 0.1 M KNO_3 of pH 2, (B) 0.1 M KNO_3 of pH 7 and (C) 0.1 M PBS of pH 7. The control experiments without hydrazine are presented as the dash lines in each case. Scan rates: 25/50/100/200/400 mV/s. The transverse arrow indicates the start potential and direction of the voltammetric scan. The vertical arrow indicates increasing scan rates.

Section A5.3: Voltammograms in 0.1 M KNO_3 (pH 9.7)

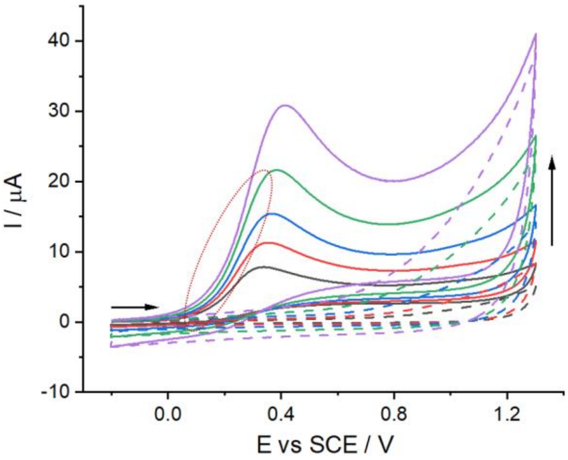

Figure A5.3. Cyclic voltammetry (solid line) at a GCE of 1.5 mM hydrazine supported by 0.1 M KNO_3 of pH 9.7. The control experiments without hydrazine are presented as the dash lines. Scan rates: 25/50/100/200/400 mV/s. The transverse arrow indicates the start potential and direction of the voltammetric scan. The vertical arrow indicates increasing scan rates. The dotted circle indicates the 'drawn out' regions of the voltammograms.

Section A5.4: Tafel analysis

Tafel analysis was conducted for the oxidative voltammetric wave in Figure 5.2 (solid line) to extract transfer coefficient information. Notably, the reactant depletion effect from the limitation of mass transport is minimal in the region from 10% to 30% of the oxidative peak current.[39] Consequently this region was taken for analysis. The resulting plot of the anodic transfer coefficient β versus the applied potential E is presented in Figure A5.4 where, following IUPAC,[40, 41] the transfer coefficient is defined as

$$\beta = \frac{RT}{F}\frac{\partial \ln|I_{ox}|}{\partial E} \tag{5.7}$$

where R is the gas constant, T the absolute temperature, F the Faraday constant, I_{ox} the oxidative current. The data clearly shows that the trasnfer coefficeint is potential dependent signalling that the electron transfer, as noted previously[2] in Chapter 4 is likely governed by Marcus-Hush electron transfer kinetics rather than Butler-Volmer kinetics. In the case of a simple electron transfer in the absence of any coupled homogeneous chemistry, such as hydrazine oxdiation at high pH and under buffered conditions (but not to the conditions of interest in the present study), then the expected behaviour is governed by the equation[2]

$$\beta = \frac{\lambda + FE_f^0}{2\lambda} - \frac{F}{2\lambda} E \tag{5.8}$$

where λ is the reorganization energy and E_f^0 the formal potential.

The use of the equation under conditions where protonation and deprotonation kinetics are important is inappropriate. Accordingly in the following modelling we use the re-organisation energy and standard electrode potential inferred from high, well-buffered pH conditions.[2] Note that the influence of preceding and following coupled chemical kinetics on the measurement of Tafel slopes and hence transfer coefficients has been noted in the context of Butler-Volmer kinetics.[42]

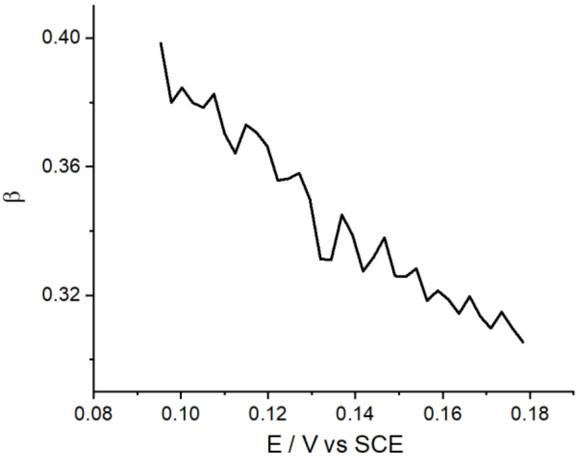

Figure A5.4. Plot of the experimentally measured *apparent* anodic transfer coefficient β versus the applied potential E in the region of 10% to 30% of the oxidative peak current.

Section A5.5: DIGISIM Modelling

The first electron transfer was assumed to be the rate-determining step (rds) for the oxidation of hydrazine which involves four electrons overall. Our recent study[33] in Chapter 6 shows that H^+ or OH^- are not engaged in the rds which likely corresponds to the formation of a very short-lived radical cation $N_2H_4^{\bullet+}$. A scheme that incorporates these facts was modelled in the DIGISIM:

$$N_2H_5^+ \rightleftarrows N_2H_4 + H^+ \tag{5.9}$$

$$N_2H_4 \xrightarrow{rds} N_2H_4^{\bullet+} + e^- \tag{5.10}$$

$$N_2H_4^{\bullet+} \xrightarrow{fast} N_2 + 4H^+ + 3e^- \tag{5.11}$$

The Marcus-Hush model was employed for the simulation, with the formal potential E_f^0 for the redox couple $N_2H_4/N_2H_4^{\bullet+}$ (0.14 V) and its reorganization energy λ (0.35 eV), as indicated above. A planar geometry of an area of 0.0707 cm^2 was selected with a semi-infinite diffusion mode. The initial concentrations of N_2H_4, $N_2H_5^+$ and H^+ were set as Figure A5.1 indicates: $[N_2H_4] = 1.44$ mM, $[N_2H_5^+] = 0.06$ mM and $[H^+] = 2 \times 10^{-10}$ M. The equilibrium constant was calculated be 5.0×10^{-9} M corresponding to the experimentally determined pK_a value of 8.3. The diffusion coefficients of N_2H_4 and $N_2H_5^+$ were 7.1×10^{-6} cm^2/s and 2.8×10^{-6} cm^2/s respectively which were measured precisely in our study in Chapter 6 at the nano-electrodes where the mass transport is well understood and free of the complications of coupled homogeneous kinetics on the timescale of the voltammetry conducted.[33] The diffusion coefficient of H^+ in the potassium electrolyte was set as 7.9×10^{-5} cm^2/s.[34, 35] A *hypothetical* value of 1×10^4 cm/s was used for the standard rate constant of the fast step to ensure its being fully driven. The simulation was conducted in a potential range (-0.2 ~ 1.3 V) with the scan rates of 25/50/100/200/400 mV/s. The fitting result between the experimental and simulated voltammetry is presented in Figure 5.3 (main text). The excellent consistency at each scan rate results in the values for the two important kinetic parameters: the standard rate constant k_0 of the rate-determining step subject to the assumption of symmetric Marcus Hush theory as discussed in the main text ($(4.5 \pm 1.0) \times 10^{-5}$ cm/s) and the rate constant k_f of the dissociation from $N_2H_5^+$ to N_2H_4 ($(5.5 \pm 2.0) \times 10^{-4}$ s^{-1}). Note that the latter value implies a value of 1.1×10^5 M^{-1} s^{-1} for the second order rate constant for the protonation of hydrazine which is fast but less than diffusion control to the extent that its value controls in part the magnitude of the voltammetric peak current.

References

[1] R. Miao, R.G. Compton, The Electro-Oxidation of Hydrazine: A Self-Inhibiting Reaction, The Journal of Physical Chemistry Letters, 12 (2021) 1601-1605.

[2] R. Miao, L. Chen, R.G. Compton, Electro-oxidation of hydrazine shows Marcusian electron transfer kinetics, Science China Chemistry, 64 (2021) 322-329.

[3] T. Erdey-Grúz, M. Volmer, Zur frage der elektrolytischen metallüberspannung, Zeitschrift fur Physikalische Chemie, 157 (1931) 165-181.

[4] J.A.V. Butler, The mechanism of overvoltage and its relation to the combination of hydrogen atoms at metal electrodes, Transactions of the Faraday Society, 28 (1932) 379-382.

[5] C. Batchelor-McAuley, E. Kätelhön, E.O. Barnes, R.G. Compton, E. Laborda, A. Molina, Recent advances in voltammetry, ChemistryOpen, 4 (2015) 224.

[6] B. Wang, X. Cao, The anodic oxidation of hydrazine on glassy carbon electrode, Electroanalysis, 4 (1992) 719-724.

[7] S. Daemi, A.A. Ashkarran, A. Bahari, S. Ghasemi, Fabrication of a gold nanocage/graphene nanoscale platform for electrocatalytic detection of hydrazine, Sensors and Actuators B: Chemical, 245 (2017) 55-65.

[8] G. Kaladevi, S. Meenakshi, K. Pandian, P. Wilson, Synthesis of well-dispersed silver nanoparticles on polypyrrole/reduced graphene oxide nanocomposite for simultaneous detection of toxic hydrazine and nitrite in water sources, Journal of the Electrochemical Society, 164 (2017) B620.

[9] S.M. Ali, Smart perovskite sensors: the electrocatalytic activity of $SrPdO_3$ for hydrazine oxidation, Journal of the Electrochemical Society, 165 (2018) B345.

[10] H.R. Zare, N. Nasirizadeh, Hematoxylin multi-wall carbon nanotubes modified glassy carbon electrode for electrocatalytic oxidation of hydrazine, Electrochimica Acta, 52 (2007) 4153-4160.

[11] M. Kamyabi, O. Narimani, H.H. Monfared, Electrocatalytic oxidation of hydrazine using glassy carbon electrode modified with carbon nanotube and terpyridine manganese (II) complex, Journal of Electroanalytical Chemistry, 644 (2010) 67-73.

[12] L. Wang, T. Meng, H. Jia, Y. Feng, T. Gong, H. Wang, Y. Zhang, Electrochemical study of hydrazine oxidation by leaf-shaped copper oxide loaded on highly ordered mesoporous carbon composite, Journal of Colloid and Interface Science, 549 (2019) 98-104.

[13] N. Hush, Adiabatic rate processes at electrodes. I. Energy-charge relationships, The Journal of Chemical Physics, 28 (1958) 962-972.

[14] C.E. Chidsey, Free energy and temperature dependence of electron transfer at the metal-electrolyte interface, Science, 251 (1991) 919-922.

[15] A. Grekov, Organic chemistry of hydrazine, Tekhnika, Kiev, (1966) 211-212.

[16] L. Meites, Handbook of analytical chemistry, Soil Science, 96 (1963) 358.

[17] R. Rich, Inorganic reactions in water, Springer Science & Business Media2007.

[18] A. Krittayavathananon, P. Srimuk, S. Luanwuthi, M. Sawangphruk, Palladium nanoparticles decorated on reduced graphene oxide rotating disk electrodes toward ultrasensitive hydrazine detection: effects of particle size and hydrodynamic diffusion, Analytical Chemistry, 86 (2014) 12272-12278.

[19] A.Y. Zhakenovich, Y. Valentina, S.T. Tussupbayev Nessipbay, Y. Zhadyra, The Search for New

Methods of Synthesis Possible of Organometallic Compounds of P, As, Sb, Bi, J. Chem, 9 (2015) 500-502.

[20] J.P. Schirmann, P. Bourdauducq, Hydrazine, Ullmann's Encyclopedia of Industrial Chemistry, (2000).

[21] A. Clearfield, K. Karlin), Progress in Inorganic Chemistry, John Wiley & Sons, Inc., New York, 47 (1998) 371-510.

[22] P. Debye, E. Hückel, Zur theorie der elektrolyte. II, Das Grenzgesetz für die Elektrische Leitfähigkeit. Phys, 305 (1923).

[23] M. Malý, M. Boublík, M. Pocrnić, M. Ansorge, K. Lorinčíková, J. Svobodová, V. Hruška, P. Dubský, B. Gaš, Determination of thermodynamic acidity constants and limiting ionic mobilities of weak electrolytes by capillary electrophoresis using a new free software AnglerFish, Electrophoresis, 41 (2020) 493-501.

[24] R.G. Compton, C.E. Banks, Understanding Voltammetry, World Scientific, 2018.

[25] N.V. Rees, R.G. Compton, Carbon-free energy: a review of ammonia-and hydrazine-based electrochemical fuel cells, Energy & Environmental Science, 4 (2011) 1255-1260.

[26] Z. Lu, M. Sun, T. Xu, Y. Li, W. Xu, Z. Chang, Y. Ding, X. Sun, L. Jiang, Superaerophobic electrodes for direct hydrazine fuel cells, Advanced Materials, 27 (2015) 2361-2366.

[27] D.C. de Oliveira, W.O. Silva, M. Chatenet, F.H. Lima, NiOx-Pt/C nanocomposites: highly active electrocatalysts for the electrochemical oxidation of hydrazine, Applied Catalysis B: Environmental, 201 (2017) 22-28.

[28] R. Madhu, V. Veeramani, S.-M. Chen, Fabrication of a novel gold nanospheres/activated carbon nanocomposite for enhanced electrocatalytic activity toward the detection of toxic hydrazine in various water samples, Sensors and Actuators B: Chemical, 204 (2014) 382-387.

[29] P. Bansal, G. Bhanjana, N. Prabhakar, J.S. Dhau, G.R. Chaudhary, Electrochemical sensor based on ZrO2 NPs/Au electrode sensing layer for monitoring hydrazine and catechol in real water samples, Journal of Molecular Liquids, 248 (2017) 651-657.

[30] M. Rudolph, A fast implicit finite difference algorithm for the digital simulation of electrochemical processes, Journal of Electroanalytical Chemistry and Interfacial Electrochemistry, 314 (1991) 13-22.

[31] A. Bott, Simulation of cyclic voltammetry using finite difference methods, Current Separations, 19 (2000) 45-48.

[32] K. Ngamchuea, S. Eloul, K. Tschulik, R.G. Compton, Planar diffusion to macro disc electrodes—what electrode size is required for the Cottrell and Randles-Sevcik equations to apply quantitatively?, Journal of Solid State Electrochemistry, 18 (2014) 3251-3257.

[33] R. Miao, L. Shao, R.G. Compton, Single entity electrochemistry and the electron transfer kinetics of hydrazine oxidation, Nano Research, (2021).

[34] S. Daniele, I. Lavagnini, M.A. Baldo, F. Magno, Steady state voltammetry at microelectrodes for the hydrogen evolution from strong and weak acids under pseudo-first and second order kinetic conditions, Journal of Electroanalytical Chemistry, 404 (1996) 105-111.

[35] X. Jiao, C. Batchelor-McAuley, E. Kätelhön, J. Ellison, K. Tschulik, R.G. Compton, The subtleties of the reversible hydrogen evolution reaction arising from the nonunity stoichiometry, The Journal of Physical Chemistry C, 119 (2015) 9402-9410.

[36] E. Laborda, M.C. Henstridge, A. Molina, F. Martínez-Ortiz, R.G. Compton, A comparison of Marcus–Hush vs. Butler–Volmer electrode kinetics using potential pulse voltammetric

techniques, Journal of Electroanalytical Chemistry, 660 (2011) 169-177.

[37] K. Ojha, E.M. Farber, T.Y. Burshtein, D. Eisenberg, A Multi-Doped Electrocatalyst for Efficient Hydrazine Oxidation, Angewandte Chemie International Edition, 57 (2018) 17168-17172.

[38] T. Wang, Q. Wang, Y. Wang, Y. Da, W. Zhou, Y. Shao, D. Li, S. Zhan, J. Yuan, H. Wang, Atomically Dispersed Semimetallic Selenium on Porous Carbon Membrane as an Electrode for Hydrazine Fuel Cells, Angewandte Chemie, 131 (2019) 13600-13605.

[39] D. Li, C. Lin, C. Batchelor-McAuley, L. Chen, R.G. Compton, Tafel analysis in practice, Journal of Electroanalytical Chemistry, 826 (2018) 117-124.

[40] R. Guidelli, R.G. Compton, J.M. Feliu, E. Gileadi, J. Lipkowski, W. Schmickler, S. Trasatti, Defining the transfer coefficient in electrochemistry: An assessment (IUPAC Technical Report), Pure and Applied Chemistry, 86 (2014) 245-258.

[41] R. Guidelli, R.G. Compton, J.M. Feliu, E. Gileadi, J. Lipkowski, W. Schmickler, S. Trasatti, Definition of the transfer coefficient in electrochemistry (IUPAC Recommendations 2014), Pure and Applied Chemistry, 86 (2014) 259-262.

[42] H. Chen, R.G. Compton, Sub- and super-Nernstian Tafel slopes can result from reversible electron transfer coupled to either preceding or following chemical reaction, Journal of Electroanalytical Chemistry, 880 (2021) 114942.

Chapter 6

Catalytic Hydrazine Oxidation at Palladium Nanoparticles Decorated Graphene Oxides

The previous chapter demonstrated that the oxidation reaction of hydrazine at carbon surface is self-inhibited. In this chapter, we investigate the catalysis of graphene oxide platelets randomly decorated with palladium nanoparticles towards hydrazine oxidation. The mechanism and kinetics of the electro-catalytic oxidation of hydrazine are deduced using single particle impact electrochemical measurements in buffered aqueous solutions across the pH range 2 - 11. Both hydrazine, N_2H_4, and protonated hydrazine $N_2H_5^+$ are shown to be electroactive at palladium electrodes and in contrast to glassy carbon following Butler-Volmer kinetics, of which the relative contribution is strongly pH-dependent. The negligible interconversion between N_2H_4 and $N_2H_5^+$ due to the sufficiently short timescale of the impact voltammetry, allows the analysis of the two electron transfer rates from impact signals thus reflecting the composition of the bulk solution at the pH in question. In this way the rate determining step in the oxidation of each species is deduced to be a one electron step in which no protons are released and so likely corresponds to the initial formation of a very short-lived radical cation either in solution or adsorbed on the platelet. Overall this chapter establishes a generic method for the elucidation of the rate determining electron transfer in a multistep process free from any complexity imposed by preceding or following chemical reactions which occur on the timescale of conventional voltammetry.

The work of Chapter 6 has been published in the journal *Nano Research*,[1] and was carried out under the supervision of Prof. Richard G. Compton (University of Oxford) and in collaboration with Prof. Lidong Shao (Shanghai University of Electric Power) who synthesized the Pd/GO materials.

6.1 Introduction

This chapter seeks to develop and illustrate a generic methodology for the study of complex multi-electron electrode processes mediated via nano-particulate materials and to illustrate this with reference to the electro-catalytic oxidation of hydrazine. The electrochemistry of hydrazine, N_2H_4, is the focus of current intense and broad interest partly because of the need for chemical sensors [2, 3] for this toxic substance but especially because of the scope for its use as the basis of several designs of fuel cells [4, 5]. In particular the reaction

$$N_2H_4(l)+O_2(g)=2H_2O(l)+N_2(g) \tag{6.1}$$

has ΔG^o = -623 kJ/mol with ΔH^o = -622 kJ/mol and ΔS^o = 3.3 J/mol K [6]. These favourable energetics give the basis for fuel cells in which hydrazine is oxidised to nitrogen at the anode whilst the cathodic reaction involves the reduction of oxygen from air to water. In such a cell the choice of optimal electrode materials for both electrodes is challenging and significant efforts have been focused on the four-electron oxidation of hydrazine in aqueous solution

$$N_2(g)+5H^++4e^-=N_2H_5^+(aq) \tag{6.2}$$

for which the formal potential is estimated to be -0.21 V [7] under conditions of unit proton activity and -1.46 V at a pH of 13. Note that the pK_a of the $N_2H_4/N_2H_5^+$ acid-base pair is 8.1 at 298 K [8, 9] so that at pH 13 hydrazine, N_2H_4, is not protonated.

Although the four-electron oxidation of hydrazine to nitrogen is highly thermodynamically favourable, as implicit in these data, it is typically electrode kinetically slow with a significant over-potential at most electrodes and this observation drives the need for the design of suitable electro-catalytic anode materials. The oxidation of hydrazine has been studied at a variety of pure metallic electrodes including platinum [10], gold [11] and palladium [12]. It has also been studied at a carbon electrode [13] as described in Chapter 4 where there are no significant complications from adsorption effects and at which the reaction involves an initial one-electron oxidation of N_2H_4 with fast follow-up chemistry and the electron transfer event shows a potential-dependent transfer coefficient well characterised by Marcus-Hush theory. However, the oxidation on carbon shows a high over-potential whereas this is substantially lowered on other electrode materials in which high-energy intermediates and transition states can be stabilised via adsorption. In all the cases of catalysis via metals such as platinum, gold and silver a major factor is that of the financial cost of the electrode material especially in comparison with carbon-based substrates. Accordingly, work has developed using tiny, minimal quantities of the valuable metals in the form of nanoparticles dispersed over a carbon based substrate. This not only offers economy in the usage of the expensive metals but may offer the additional prospect of altered, preferably improved catalytic behaviour of the nanoparticle in comparison with the bulk metal [14-16].

Materials based on nanoparticles supported on carbon materials are usually formed into a composite material before use as an electrode. Such composites are notoriously difficult to characterise in terms of their intrinsic fundamental electron transfer kinetics at a level other than essentially empirical. The major problem underpinning this is the need to quantitatively describe and decouple the mass transport to and within the composite of uncertain porosity and intrinsic heterogeneity so as to uniquely identify the electron transfer kinetics [17, 18]. In particular, and notoriously, the development of 'thin layer' diffusion within electroactive composites gives the impression of electrochemical reversibility so precluding extraction of any electrode kinetic effects [19-21].

In the case of composites comprised of an aggregated ensemble of single carbon particles themselves decorated with metallic nanoparticles, one approach to circumvent the issues with composites and porous layers is to explore the behaviour of the component decorated particles at the single entity level where the mass transport is well understood. Thus in the present chapter we seek to explore the kinetics and mechanism of the oxidation of hydrazine at crudely square-shaped graphene oxide (GO) nano-platelets (of dimensions *ca.* 3.1 µm in length and 3 nm in thickness corresponding to 2-5 layers [22-24]) of GO which themselves have been decorated with quasi-spherical palladium nanoparticles of *ca.* 2.7 nm in diameter. Fuller information about Pd/GO was reported in Chapters 2 and 3. Figure 6.1 shows a schematic diagram of the Pd/GO particle surface. Thus, in practical use the GO nano-platelets are used to support the nano-particulate Pd catalyst and the decorated platelets themselves are formed into a composite which coats an electrode used to apply a potential to the porous composite.

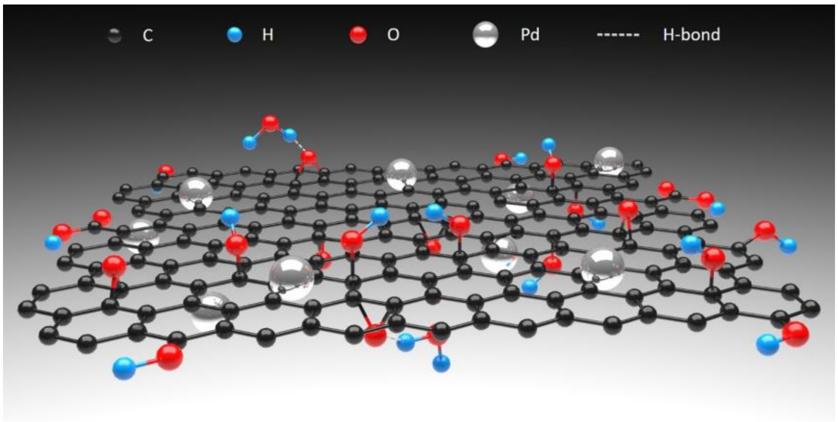

Figure 6.1. Schematic diagram of the monolayer Pd nanoparticles decorated graphene oxide nanoplatelets

(Pd/GO)

In this chapter we use ‘nano-impact’ experiments [25-27] to measure the kinetics and mechanism of the oxidation of hydrazine at Pd/GO platelets at the single entity level. In a nano-impact experiment an electrode is immersed in a suspension of the entities of interest, specifically Pd/GO nano-platelets in the present case, and these particles occasionally impact the electrode by virtue of their random, Brownian motion. The impacting particles can make transient electrical contact with the electrode for the duration of the impact which can last from a few milliseconds to tens or even hundreds of seconds in the case of carbon nanotubes [28]. In this situation for the time of the impact, the collided particle acts as a tiny electrode of a size corresponding to that of the particle itself and, if the solution contains species such as N_2H_4 in the present case to which the particle is electro-catalytic then currents can flow if suitable potentials are applied to the immersed electrode. In the case of Pd/GO platelets impacting an electrode in an aqueous solution of hydrazine the impact is characterised by on-off steps in the current with each switching event corresponding to the arrival or departure of a single platelet from the electrode-solution interface. The magnitude of the current flowing is explored as a function of the applied potential and the solution composition and conditions, especially pH, thus revealing the kinetics and mechanism of the hydrazine oxidation at the platelets. In this way a generic methodology is established and illustrated for deducing the rate determining electron transfer step in a complex multi-electron process with coupled chemical reactions mediated via nanomaterials.

6.2 Experimental

Phosphate buffer solutions of a total concentration 0.1 M were used for the pH range 7 - 11, of which the compositions for each are presented in the Appendix Section A6.1. A solution of 10 mM HNO_3 supported by 0.1 M KNO_3 was used for pH 2. Hydrazine oxidation at higher pHs using PBS buffer solutions with higher concentration (eg. 0.3 M PBS, 0.5 M PBS and 0.5 M PBS with 0.2 M potassium chloride), as investigated in Chapter 4 [13], displayed similar electrochemical responses.

Cyclic voltammetry of hydrazine oxidation at a Pd/GO modified GC electrode

1.0 mg Pd/GO was added into 5 mL deionized water and sonicated for 15 min to obtain a well-dispersed suspension with a Palladium atom concentration of ca. 5.2×10^{-7} M. 7 μL Pd/GO suspension was then drop-cast onto the Glassy Carbon (GC) electrode and dried under a N_2 atmosphere. The prepared electrode served as a working electrode with the reference electrode (SCE) and the counter electrode (graphite rod) completing the circuit. The estimated coverage of Pd/GO nanoplatelets is 7.1×10^{-9} mol/cm^2, the thickness of which is around five layers of nanoplatelets. 5 mL of 0.1 M PBS (pH 8.1) containing 1.5 mM N_2H_4 was vigorously bubbled with N_2 for 15 min prior to the Cyclic Voltammetry (CV) measurements and an atmosphere of N_2 was maintained during the experiment. A control experiment was performed in the same solution but on a bare GC electrode.

Chronoamperometry of hydrazine oxidation on individual Pd/GO particles

A carbon fibre microwire electrode [29] of 7 μm in diameter and 1 mm in length (as described in Section 2.2.2) functions as the working electrode whilst the reference and counter electrodes are as mentioned above. 5 mL of the appropriate buffer solution (see above and Appendix

Section A6.1) containing 1.5 mM hydrazine was degassed with N_2 for 15 min to remove the dissolved oxygen, followed by the addition of the suspension to form a final solution with 1.1 × 10^{-14} M Pd/GO while N_2 kept bubbling for 10 s to make it well-dispersed. Chronoamperometry with the duration of 20 s for each scan was recorded in succession after the microwire electrode was inserted into the suspension. A control experiment was conducted as above but without the addition of the Pd/GO suspension. Note that the potentiostat used herein enables an accurate conservation of the overall charge transferred in an 'nano-impact' event [30].

6.3 Results and Discussion

The catalytic ability of the Pd/GO is first discussed by comparing the electrochemical responses of cyclic voltammetry of hydrazine oxidation at a bare GC electrode and the same GC electrode but modified with Pd/GO via drop-casting. Then the nano-impact method is employed to study the electroactivity of protonated hydrazine ($N_2H_5^+$) and hydrazine (N_2H_4) at pH 2 and 11 respectively where the solution exclusively contains only one or other of the two species, and the kinetics of their oxidation catalysed by the single entity of Pd/GO assisted with DIGISIM simulation. This enables the study of hydrazine oxidation at intermediate pH values of 7 - 8.8 where the oxidation of both N_2H_4 and $N_2H_5^+$ contribute to the electrochemical signal. The interpretation is simplified by the tiny size of the platelets which imposes an extremely short timescale for diffusion. This is so short that the dissociation of protonated hydrazine or the protonation of N_2H_4 can be neglected on the voltammetric timescale of the nano-impact experiments. The current-potential response reflects simply reflects the composition of the bulk solution as dictated by its pH.

Characterization of the Pd/GO nanoplatelets

The Pd/GO nanoplatelets were characterized by transmission electron microscopy (TEM, FEI Tecnai G2 F20). Figure 6.2 displays the lamellate morphology of the sample Pd/GO (3.1 ± 0.2 μm in length and *ca.* 3 nm in thickness comprised of several layers), whilst spheroidal Pd nanoparticles (2.7 ± 0.2 nm in diameter) were observed to be randomly immobilized on the surface of the platelets, of which the distributions were discussed in detail previously [31, 32]. The weight loading of Pd was determined to be 5.5% *via* Inductively Coupled Plasma Mass Spectrometry (ICP-MS), and its surface density was measured to be 1.1×10^{4} μm^{-2} by the software ImageJ.

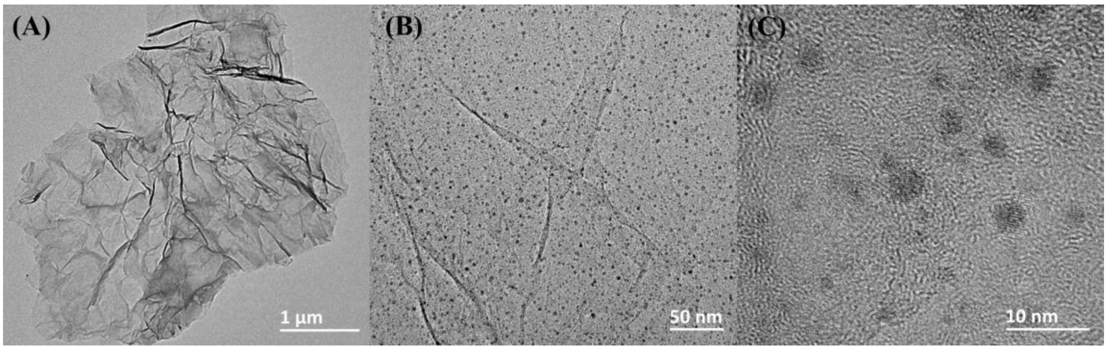

Figure 6.2. TEM images of Pd nanoparticles decorated graphene oxides nanoplatelets (Pd/GO)

Demonstration of the electro-catalytic ability of Pd/GO using Pd/GO modified electrodes

To investigate the electrochemical oxidation of hydrazine at the Pd/GO platelets, cyclic voltammetry (CV) at bare and Pd/GO modified GC electrodes were conducted in 1.5 mM aqueous solutions of hydrazine supported by 0.1 M PBS (pH 8.1). As illustrated in Figure 6.3, irreversible voltammetric features corresponding to the four-electron hydrazine oxidation [33, 34] were observed at both electrodes. The oxidative peak at a scan rate of 50 mV/s appears at 0.81

V vs SCE for the bare electrode (dashed line), while that for the modified electrode (solid line) is seen at -0.14 V vs SCE with a noticeably lower over-potential. Meanwhile, the peaks from the Pd/GO electrode, at all scan rates, display larger anodic currents compared to those from the bare electrode. The latter have a low, potential-dependent transfer coefficient resulting in a peculiarly elongated shape as reported and explained elsewhere[13]. Comparison of the two sets of curves in Figure 6.3 demonstrates the ability of Pd/GO to effectively catalyse hydrazine oxidation that is attributed in part to the high specific surface area of Pd nanoparticles as well as the excellent electro-catalytic behaviour of Pd noted in the literature [35, 36].

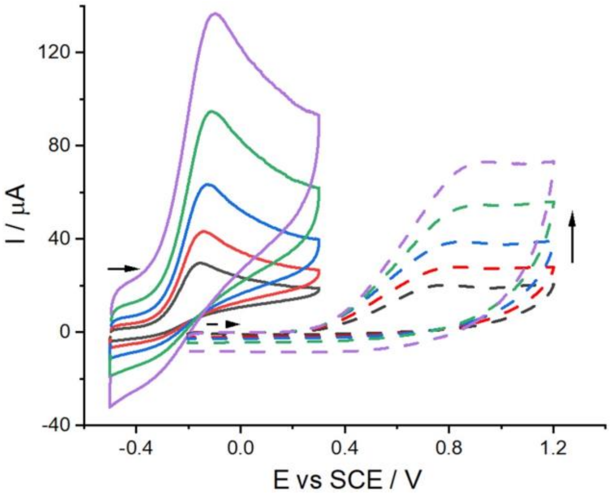

Figure 6.3. Voltammetry at a bare GC electrode (dashed line) and a Pd/GO modified electrode (solid line) in 0.1 M PBS (pH 8.1) with 1.5 mM N_2H_4. Scan rates: 25/50/100/200/400 mV/s. The vertical arrow indicates increasing scan rates. The transverse arrow indicates the start of the voltammetric scans.

Direct oxidation of N_2H_4 and $N_2H_5^+$: nano-impact experiments

Impact electrochemistry was conducted to probe into the thermodynamics and kinetics of hydrazine oxidation via measuring the Faradaic charge transfer from the catalytic current amplification-mediated electron transfer during the collision of individual particles with an electrode [37, 38]. A clean carbon fibre electrode was inserted into a suspension of Pd/GO particles (6.6×10^6 per cm^3) supported by 10 mM HNO_3 and 0.1 M KNO_3 of pH 2 with 1.5

mM hydrazine as described in the experimental section and separately for comparison into a ‘blank’ solution without particles. At pH 2 the hydrazine exists essentially exclusively in its protonated form, $N_2H_5^+$. Upon immersion current-time transients were recorded at an applied potential of 0.75 V vs SCE. As illustrated in Figure 6.4A-B, clear Faradaic current steps were seen with a magnitude of around 0.13 nA in the presence of Pd/GO (red line) whereas no steps or spikes observed in the absence of Pd/GO nano-platelets (black line). This indicates that the impact of single Pd/GO particles on the microwire surface leads to the catalytic oxidation of protonated hydrazine $N_2H_5^+$ by electron transfer to the electrode. The fluctuations in current may be caused by the nanoscopic motion of the particle on the electrode surface that likely brings about the variation of the electrical contact, electro-generated nitrogen may also contribute if nano-bubbles are formed [39]. Note that the sustained current following the step associated with the arrival of the Pd/GO particles indicates that the latter remains close to the surface of the electrode and is kept in electrical contact for several seconds. The average currents of the individual steps (≥ 40 for each potential) from the collision of Pd/GO nano-platelets were measured as a function of the applied potential and the results are shown in Figure 6.5A (black squares), where a voltammogram-like response is seen with a current plateau of *ca.* 0.13 nA when the potential exceeds *ca.* 0.5 V vs SCE. Mass transport corrected Tafel analysis [40] was adopted to analyse the characteristic so to numerically extract the transfer coefficient for the electro-oxidation reaction of $N_2H_5^+$ via a plot of $\ln\left|1/I - 1/\ln I_{\mathrm{lim}}\right|$ versus E (Appendix Section A6.2, Figure A6.1A):

$$\beta = -\frac{RT}{F}\frac{d\ln\left(\frac{1}{I}-\frac{1}{I_{\mathrm{lim}}}\right)}{dE} \tag{6.3}$$

where I is the current, I_{lim} the mass transport limiting current, E the applied potential, R the gas constant, T the absolute temperature and F the Faraday constant. The anodic transfer coefficient $\beta_{N_2H_5^+}$ of the catalytic reaction at individual Pd/GO particles was inferred to be 0.41 ± 0.05 with the implication that the electrode reaction is fully electrochemically irreversible. Note that for a multi-electron process the apparent transfer coefficient is given by n' + β [41] where n' is the number of electrons preceding the rate determining step and β is the transfer coefficient of the rate determining step. Thus the observed value is consistent with n' = 0 and the measured β value is close to 0.5. Since no electrons precede the slowest step the first electron transfer is the rate-determining step [42, 43].

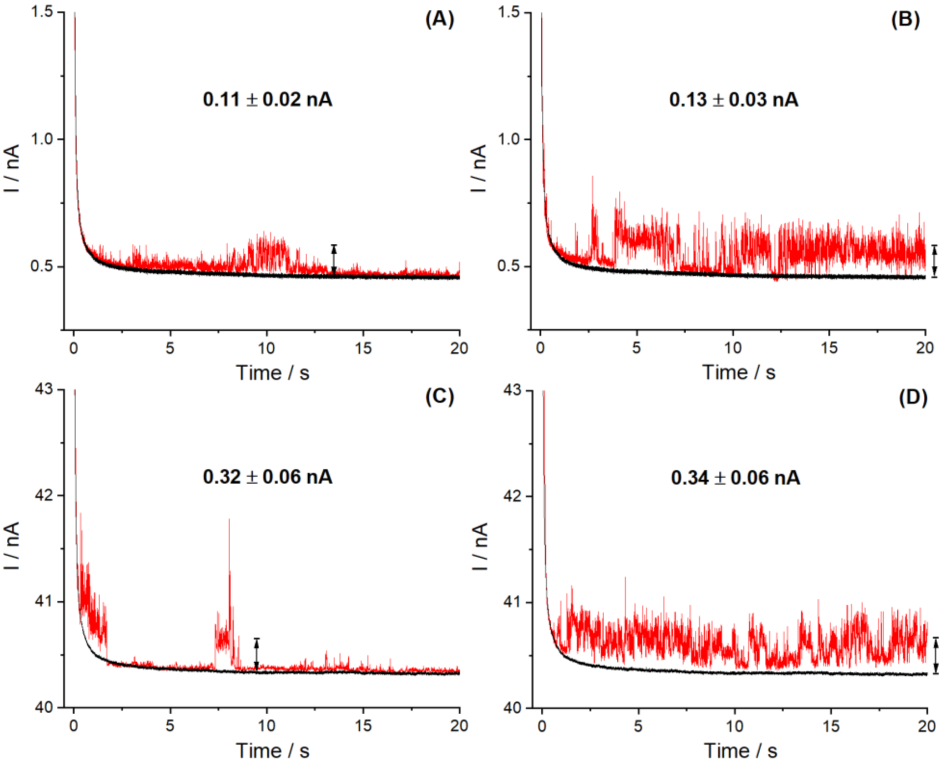

Figure 6.4. Chronoamperometric profiles showing the Faradaic steps from the direct oxidation of hydrazine catalysed by individual Pd/GO particles impacting on the electrode surface in 1.5 mM aqueous solution of hydrazine. (A-B) supporting electrolyte: 10 mM HNO_3 and 0.1 M KNO_3 of pH 2, applied potential: 0.75 V vs SCE; (C-D) supporting electrolyte: 0.1 M PBS of pH 11, applied potential: 0.35 V vs SCE.

Analogous impact experiments were performed for the direct oxidation of unprotonated hydrazine (N_2H_4) in 1.5 mM solution of hydrazine supported by 0.1 M PBS of pH 11 as presented in Figure 6.4C-D where a potential of 0.35 V vs SCE is applied and the high pH ensures that the hydrazine is exclusively present in its deprotonated form, N_2H_4. Figure 6.5A (aquamarine squares) again manifests a voltammogram-like feature with a plateau at *ca.* 0.31 nA from 0.15 V vs SCE. The corresponding $\beta_{N_2H_4}$ value was estimated to be 0.45 ± 0.08 again (Appendix Section A6.2, Figure A6.1B) corresponding to the fully electrochemically irreversible limit and a rate determining first electron transfer.

The electrical contact between the Pd/GO nanoplatelets and the electrode during the impact collision, as discussed in Chapter 3 [31], occurs at one of the edges of the platelet. For this reason and due to the limited conductivity of the GO, the catalytic activity towards hydrazine oxidation is confined to a zone physically close to the impacting edge. In terms of mass transport, this was shown in Chapter 3 [31] to be formally equivalent to a microband electrode with a length of 3.1 ± 0.2 μm and a width of *ca.* 3.0 nm. Modelling the appropriate mass transport regime [28] allows the inference from the plateau currents seen at high over-potentials of the diffusion coefficients $D_{N_2H_5^+}$ and $D_{N_2H_4}$ as $(2.8 \pm 0.3) \times 10^{-6}$ and $(7.1 \pm 0.8) \times 10^{-6}$ cm^2/s respectively based on the Aoki equation [44, 45] for a micro-band electrode (Appendix Section A6.3).

DIGISIM (version 3.03b, Bioanalytical System, Inc, USA) was then utilized to extract further mechanistic detail of the hydrazine oxidation. DIGSIM is a commercial simulation software built on the innovative, pioneering simulation work of M. Rudolph, based on a fully implicit finite difference method [46]. A hemicylindrical geometry was selected in DIGISIM to approximate a catalytically-active microband, using a length of 3.1 μm and an equivalent radius, r, of 1.0 nm from the relationship $r = w/\pi$ [47, 48] where w is the width of the microband as previously inferred [31].

The following mechanism was investigated:

$$N_2H_5^+ \rightleftharpoons N_2H_4 + H^+ \tag{6.4}$$

$$N_2H_5^+ = N_2 + 5H^+ + 4e^- \tag{6.5}$$

$$N_2H_4 = N_2 + 4H^+ + 4e^- \tag{6.6}$$

where the equilibrium constant K_{eq} for the acid-base reaction between hydrazine and its protonated form is known to be 7.9 × 10^{-9} M (pK_a = 8.1 at 298 K). Note that the diffusional timescale of the impact experiment corresponds under the microband/hemicylindrical electrode model employed to voltammetric of w^2/D where D is the diffusion coefficient of the electroactive species. This corresponds to a sub-nanosecond duration so that it is expected that the contribution of the acid-base reaction of Eq. (6.4) is negligible and the response reflects the sum of the individual oxidations of hydrazine and protonated hydrazine with concentrations ‘frozen’ at their bulk values. The modelling below shows that the response is indeed the sum of the two forms of hydrazine without interconversion on the experimental timescale.

First however the data at pH 2 was analysed where the reaction was assumed to be exclusively

$$N_2H_5^+ = N_2 + 5H^+ + 4e^- \tag{6.7}$$

and, where the electrode reaction has a rate determining first electron transfer as implied by the corresponding transfer coefficient inferred above and using the diffusion coefficient for $N_2H_5^+$ deduced above. This simulation (detailed in the Appendix Section A6.4) shows a very satisfactory fit with the experiment as depicted in Figure 6.5B (black line), confirmed the electrochemical irreversibility and gave a composite parameter of $k^0_{N_2H_5^+} e^{-\beta_{N_2H_5^+} F E^0_{f,N_2H_5^+} / RT}$ = 0.06 ± 0.02 cm/s, where $\beta_{N_2H_5^+} = 0.41$ and the value of $D_{N_2H_5^+} = 2.8 \times 10^{-6}$ cm^2/s as deduced above from the plateau current.

Similarly the data from pH 11 was analysed (detailed in the Appendix Section A6.4) exclusively in terms of the process

$$N_2H_4 = N_2 + 4H^+ + 4e^- \tag{6.8}$$

again with a rate determining first electron transfer as signalled by the measured transfer coefficient and using the diffusion coefficient deduced above. Figure 6.5B (aquamarine line) shows a good fit between simulation and experiment using a composite rate constant of $k^0_{N_2H_4} e^{-\beta_{N_2H_4} F E^0_{f,N_2H_4} / RT}$ = 3.3 ± 0.2 cm/s, where $\beta_{N_2H_4}$ = 0.45 and $D_{N_2H_4}$ = 7.1 × 10^{-6} cm^2/s. Note that the above-mentioned kinetic data is extracted from the analysis of the impacts from the view of nano-sized entities; extrapolation of the data to bulk Pd is cautioned [41, 49].

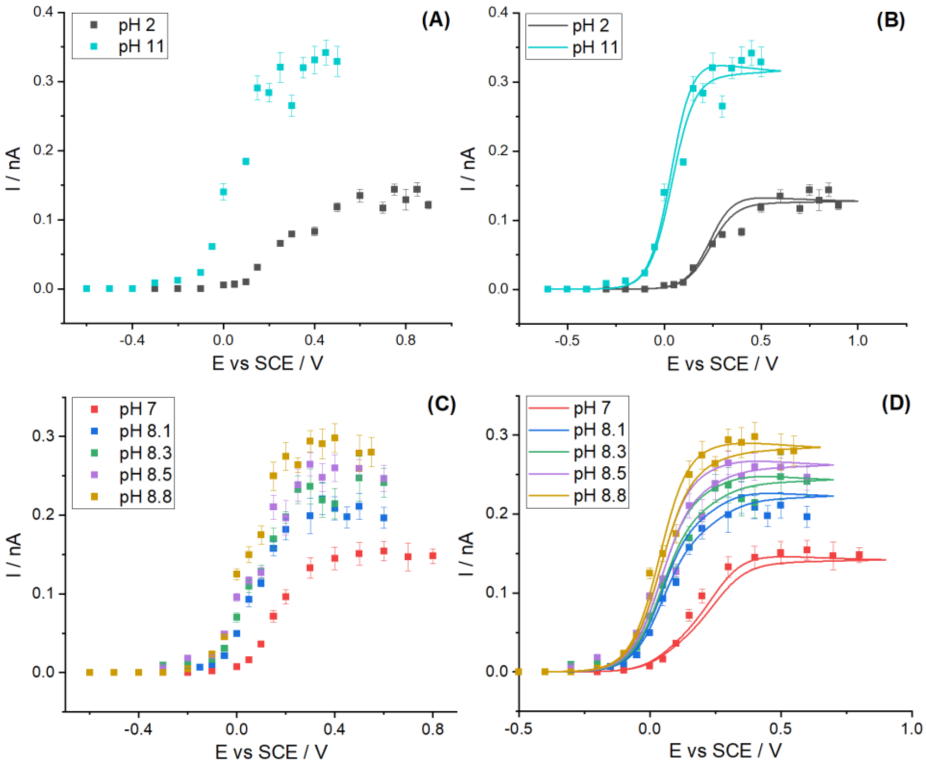

Figure 6.5. Experimental plots of the average oxidative Faradaic step currents versus applied potentials from nano impacts in the solutions of (A) black squares: 1.5 mM hydrazine supported by 10 mM HNO_3 and 0.1 M KNO_3 of pH 2, aquamarine squares: 1.5 mM hydrazine supported by 0.1 M PBS of pH 11; (C) 1.5 mM

hydrazine supported by 0.1 M PBS of the intermediate pH 7/8.1/8.3/8.5/8.8. DIGISIM-simulated curves of (B) black line: $N_2H_5^+$ oxidation at pH 2, aquamarine line: N_2H_4 oxidation at pH 11; (D) concurrent oxidation of $N_2H_5^+$ and N_2H_4 at pH 7/8.1/8.3/8.5/8.8. The input of the forward rate constant is 200 cm/s. The number of the impacting current steps analysed for each square is ≥ 40. The error bar is the standard error of the mean.

Concurrent oxidation of N_2H_4 and $N_2H_5^+$: nano-impact experiments

Next attention was focused on the full scheme given in Eq. (6.4) - (6.6). The two electrode reactions were modelled using the data inferred from the conditions as discussed above where the speciation was essentially exclusively one species or the other. This assumption is explored more fully below in respect of the consideration of the bulk pH. Further the level of buffering was assumed to be such that the equilibrium between the different forms was rapidly established in bulk solution but that in the vicinity of the impacted particles the voltammetric timescale is sufficiently short as to preclude re-equilibration between the two forms as discussed above.

The nano impact experiments were performed in the solutions of 1.5 mM hydrazine supported by 0.1 M PBS at the intermediate pH values from 7 to 8.8 where the electro-oxidations of N_2H_4 and $N_2H_5^+$ may both contribute to the measured signals. The relative extent is controlled not only by the equilibrium constants (K_{eq} , see above), but also, at least in principle, the homogeneous kinetics of the interconversion between the two species. The latter represents a single adjustable parameter in our modelling below. The mean catalytic impact currents under a series of potentials at pH 7 - 8.8 are presented in Figure 6.5C where again pH-dependent “steady-state currents” are seen. Upon the rise of pH, the plateau current increases conspicuously in accordance with that observed in Figure 6.5A due to the increase in the component of N_2H_4 which probably on account of being uncharged has a high diffusion coefficient than protonated hydrazine. Meanwhile, the halfwave potential shifts to more negative potentials reflecting the higher effective composite electrochemical rate constant of N_2H_4 oxidation compared to $N_2H_5^+$.

Based on Eq. (6.4) - (6.6) in consideration of the homogeneous reaction of the two species $N_2H_5^+$ and N_2H_4, the simulation for the concurrent oxidation was conducted using the same hemicylindrical geometry with the kinetic parameters derived above. The excellent fittings in Figure 6.5D confirm the suitability of the proposed mechanism at the intermediate pHs (detailed in the Appendix Section A6.4) and, importantly as shown in Figure A6.2 to be effectively independent of the forward and back rate constants of the homogeneous reaction of Eq. (6.4).

The modelling of the data in Figure 6.5D for the pH range 7 - 8.8 shows a good fit using the values for the electrochemical rate constants for the oxidation of hydrazine at pH 11 and of protonated hydrazine at pH 2. We therefore infer that these values are independent of pH. The mechanistic implications of this observation builds on the basis of the expected pH variation of the electrochemical rate constant for a fully irreversible oxidation (detailed in the Appendix Section A6.5). On this consideration, the first electron transfer and also the rate determining step for both the oxidations of the two species $N_2H_5^+$ and N_2H_4 is not associated with the release of protons during the impact event. This suggests therefore the initial formation of the radical cations $N_2H_5^{2+}$ and $N_2H_4^+$ which survive, either as solution phase or adsorbed species, at least on the voltammetric diffusional timescale of the particle impact (sub-nanoscale), presented as

$$N_2H_5^+ \rightleftarrows N_2H_4 + H^+ \tag{6.9}$$

$$N_2H_5^+ \xrightarrow{rds} N_2H_5^{2+} + e^- \tag{6.10}$$

$$N_2H_5^{2+} \xrightarrow{fast} N_2 + 5H^+ + 3e^- \qquad (6.11)$$

$$N_2H_4 \xrightarrow{rds} N_2H_4^+ + e^- \qquad (6.12)$$

$$N_2H_4^+ \xrightarrow{fast} N_2 + 4H^+ + 3e^- \qquad (6.13)$$

Of course the application of Butler-Volmer theory as in the Appendix Section A6.5 involving a formal potential is unlikely to be realistic at the timescale under consideration. However it is clear that the rate constants for the hydrazine and protonated hydrazine oxidations are exponentially dependent on potential, are controlled by the first electron transfer and are pH independent all signalling that on the Pd/GO nanoplatelets the rate determining step is an initial electron transfer creating a radical cation.

6.4 Conclusions

In this chapter, Palladium nanoparticles decorated graphene oxide nanoplatelets (Pd/GO) were utilized as an electro-catalyst towards hydrazine oxidation either as dropcast (ensemble) modified electrodes or as single entities in nano impact experiments in buffered solutions. The direct oxidation of hydrazine (N_2H_4) and protonated hydrazine ($N_2H_5^+$) were investigated at pH 2 and 11 respectively by impact electrochemistry which generates average impact currents as a function of potential that show voltammogram-like characteristics with steady-state currents, from which the essential kinetics were derived: $\beta_{N_2H_5^+}$ = 0.41, $\beta_{N_2H_4}$ = 0.45, $D_{N_2H_5^+}$ = 2.8 × 10^{-6} cm^2/s, $D_{N_2H_4}$ = 7.1 × 10^{-6} cm^2/s, $k^0_{N_2H_5^+} e^{-\beta_{N_2H_5^+} F E^0_{f,N_2H_5^+} / RT}$ = 0.06 cm/s and $k^0_{N_2H_4} e^{-\beta_{N_2H_4} F E^0_{f,N_2H_4} / RT}$ = 3.3 cm/s. Under the conditions of minimal effect from the interconversion between $N_2H_5^+$ and N_2H_4 due to the ultrashort voltammetric timescale on individual Pd/GO particle, the simulation for the nano-impacts from the intermediate pHs of 7

- 8.8 reveals the mechanism for the hydrazine oxidation, the rate determining step that involves no proton release and provides kinetic data for the latter.

Appendix

Section A6.1: Chemical compositions of the solutions from pH 2 - 11

Table A6.1. Chemical compositions of the solutions from pH 2 - 11

pH	$[H^+]$ / M	$[H_2PO_4^-]$ / mM	$[HPO_4^{2-}]$ / mM	$[N_2H_4]$ / mM	$[N_2H_5^+]$ / mM
2	1.0E-02	/	/	0	1.500
7	1.0E-07	61.3	38.7	0.110	1.390
8.1	7.9E-09	11.2	88.8	0.750	0.750
8.3	5.0E-09	7.4	92.6	0.920	0.580
8.5	3.2E-09	4.8	95.2	1.073	0.427
8.8	1.6E-09	2.5	97.5	1.250	0.250
11	1.0E-11	0.0	100.0	1.498	0.002

Section A6.2: Mass transport corrected Tafel analysis

The Tafel slopes were calculated to be 0.41 ± 0.05 for the direct oxidation of $N_2H_5^+$ at pH 2 and 0.45 ± 0.08 for the direct oxidation of N_2H_4 at pH from mass transport corrected Tafel analysis of the nano-impact data (see the main text).

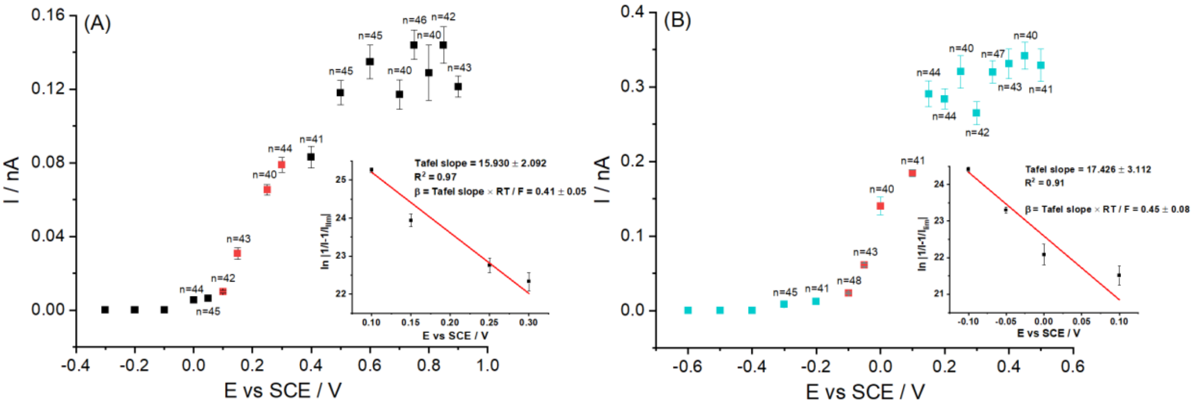

Figure A6.1. Plot of the average impact-induced oxidative Faradaic step currents versus applied potentials where the supporting electrolytes are (A) 10 mM HNO_3 and 0.1 M KNO_3 of pH 2 and (B) 0.1 M PBS of pH 11. n is the number of the steps analysed. The error bar is the standard error of the mean.

Section A6.3: Calculation of the diffusion coefficients

The chronoamperometric transient of a microband electrode is given by

$$i(t) = nFDclf(\tau) \tag{6.14}$$

with

$$f(\tau) = 1.004 + \frac{1}{\sqrt{\pi\tau}} + 1.3\exp(-2.53x) + \left(-1.133 + \frac{0.59}{1+3\exp\left(\frac{x-1}{0.3415}\right)}\right) \times \exp\left(\frac{-9.85}{\left|\ln\left[\tau\left(17.22 - \frac{18.04}{1+\exp\left(\frac{x-1.113}{0.367}\right)}\right)\right]\right|}\right) \tag{6.15}$$

$$\tau = \frac{Dt}{w^2} \tag{6.16}$$

$$x = \log_{10}\frac{l}{w} \tag{6.17}$$

where n is the number of electrons transferred (assumed to be 4 [33, 50, 51]), D the diffusion coefficient, c the concentration of the analyte, l the length of the microband, w the width of the microband and t the time in seconds.

The limiting current is 0.13 ± 0.02 nA for the direct oxidation of $N_2H_5^+$, thus giving the $D_{N_2H_5^+}$ value of $(2.8 \pm 0.3) \times 10^{-6}$ cm^2/s, whist that for N_2H_4 is 0.31 ± 0.04 nA giving the $D_{N_2H_4}$ value of $(7.1 \pm 0.8) \times 10^{-6}$ cm^2/s.

Section A6.4: Details of the DIGISIM simulation

Table A6.2. DIGISIM simulation parameters

pH	$\beta_{N_2H_5^+}$	$k_{N_2H_5^+}$ (cm/s)	$D_{N_2H_5^+}$ (cm^2/s)	$\beta_{N_2H_4}$	$k_{N_2H_4}$ (cm/s)	$D_{N_2H_4}$ (cm^2/s)	$K_{eq,eff}$	k_f (s^{-1})
2	0.41	0.06	2.8×10^{-6}	/	/	/	/	/
7				0.45	3.3	7.1×10^{-6}	0.08	variable
8.1							1.0	
8.3							1.6	
8.5							2.5	
8.8							5.0	
11	/	/	/				/	/

The parameters used in the following simulation are summarised in Table A6.2. $\beta_{N_2H_5^+}$ and $\beta_{N_2H_4}$ are the transfer coefficients of $N_2H_5^+$ and N_2H_4 respectively; $D_{N_2H_5^+}$ and $D_{N_2H_4}$ are the diffusion coefficients of $N_2H_5^+$ and N_2H_4 respectively. Note that because the processes are fully electrochemically irreversible it is not possible to obtain unique values of the formal potentials and the electrochemical rate constants. Rather a single composite rate constant, $k = k^0 e^{-\beta F E_f^0 / RT}$ ($k_{N_2H_5^+}$ for $N_2H_5^+$ oxidation and $k_{N_2H_4}$ for N_2H_4 oxidation), is inferred with the implications that the simulation data are consistent with any pairs of standard electrochemical rate constant and formal potential values which fit the composite relationship.

Simulation for hydrazine oxidation at pH 2

As hydrazine oxidation involves four electrons transferred of which the first is rate-determining [50, 52, 53] and the homogeneous interconversion between N_2H_4 and $N_2H_5^+$ is negligible at pH 2, the mechanism of $N_2H_5^+$ oxidation was:

$$N_2H_5^{+} \xrightarrow{rds} N_2H_{5-a}{}^{2-a} + aH^{+} + e^{-} \qquad (6.18)$$

$$N_2H_{5-a}{}^{2-a} \xrightarrow{fast} N_2 + (5-a)H^+ + 3e^- \tag{6.19}$$

where a is the number of the protons released in the rate determining step. The rate constant for the fast step was set as 1 × 10^4 cm/s so to be fully driven. The formal potential E_f^0 for the rate determining step and the electrochemical rate constants were set arbitrarily as they cannot be determined independently for a fully irreversible process, rather an infinite range of pairs of these values are possible but subject to a composite electrochemical rate constant dependent on both parameters. Given the values of $\beta_{N_2H_5^+} = 0.41$ and $D_{N_2H_5^+} = 2.8 \times 10^{-6}$ cm^2/s as above, the experimental voltammogram-like characteristic from nano-impacts of single Pd/GO in Figure 6.5A (black squares) was fitted well by the numerical simulation as depicted in Figure 6.5B (black line), yielding a composite electrochemical rate constant of $k^0_{N_2H_5^+} e^{-\beta_{N_2H_5^+} F E^0_{f,N_2H_5^+} / RT}$ = 0.06 ± 0.02 cm/s.

Simulation for hydrazine oxidation at pH 11

For pH 11, the mechanism of N_2H_4 oxidation was proposed as:

$$N_2H_4 \xrightarrow{rds} N_2H_{4-b}{}^{1-b} + bH^+ + e^- \tag{6.20}$$

$$N_2H_{4-b}{}^{1-b} \xrightarrow{fast} N_2 + (4-b)H^+ + 3e^- \tag{6.21}$$

where c is the number of the protons released in the rate determining step. Setting the formal potential arbitrarily with the known parameters $\beta_{N_2H_4} = 0.45$ and $D_{N_2H_4} = 7.1 \times 10^{-6}$ cm^2/s, the simulated result in Figure 6.5B (aquamarine line) is in accordance with the experimental data (aquamarine squares), from which the composite parameter $k^0_{N_2H_4} e^{-\beta_{N_2H_4} F E^0_{f,N_2H_4} / RT}$ for the direct oxidation of N_2H_4 was derived to be 3.3 ± 0.2 cm/s.

Simulation for hydrazine oxidation at pH 7 - 8.8

For the intermediate pHs from 7 - 8.8 where both N_2H_4 and $N_2H_5^+$ contribute to the electrochemical signals, a mechanism for the configurative oxidation of $N_2H_5^+$ and N_2H_4 was proposed:

$$N_2H_5^+ \rightleftarrows N_2H_4 + H^+ \tag{6.22}$$

$$N_2H_5^+ \xrightarrow{rds} N_2H_{5-a}{}^{2-a} + aH^+ + e^- \tag{6.23}$$

$$N_2H_{5-a}{}^{2-a} \xrightarrow{fast} N_2 + (5-a)H^+ + 3e^- \tag{6.24}$$

$$N_2H_4 \xrightarrow{rds} N_2H_{4-b}{}^{1-b} + bH^+ + e^- \tag{6.25}$$

$$N_2H_{4-b}{}^{1-b} \xrightarrow{fast} N_2 + (4-b)H^+ + 3e^- \tag{6.26}$$

Note that the *effective* equilibrium constant between $N_2H_5^+$ and N_2H_4 is pH-dependent as $K_{eq,eff} = K_{eq} / \left[H^+\right]$. The simulation was conducted based on the kinetic parameters inferred from pH 2 and 11. The simulated result (lines) is presented in Figure 6.5D, consistent with the experimental data (squares). Figure A6.2 demonstrates that the simulation is almost independent of the forward and back rate constant k_f of the homogeneous reaction. This is likely ascribed to the ultrashort voltammetric timescale for the oxidation reactions occurring at the individual Pd/GO particle refraining from the interconversion between $N_2H_5^+$ and N_2H_4.

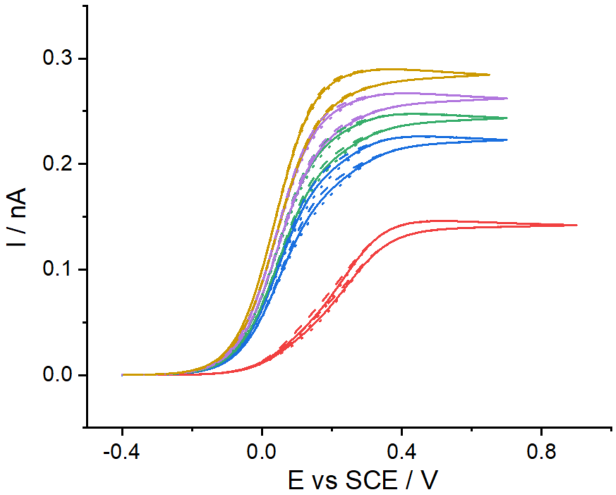

Figure A6.2. DIGISIM-simulated curves for hydrazine oxidation at pH 7 (red)/pH 8.1 (blue)/pH 8.3 (green)/pH 8.5 (purple)/pH 8.8 (yellow) using the parameters derived from pH 2 and pH 11. The forward rate constants k_f are 2 s^{-1} (dotted), 200 s^{-1} (solid) and 2×10^4 s^{-1} (dashed).

Section A6.5: pH dependency of the electrochemical rate constant within a Butler-Volmer perspective

We consider an electrochemical one-electron oxidation process:

$$A = B + mH^{+} + e^{-} \tag{6.27}$$

and note that the equilibrium potential is given via the Nernst equation as indicated by Eq. (1.20):

$$E = E_f^0(A/B/H^{+}) + \frac{RT}{F}\ln\left(\frac{[B]}{[A]}\right) - 2.303\frac{mRT}{F}pH \tag{6.28}$$

where $[A]$ and $[B]$ are the concentrations of the species of A and B respectively; $E_f^0(A/B/H^{+})$ is the formal potential involving the species A, B and H^{+}.

We can alternatively write

$$E = E_f^0\left(A/B\right) + \frac{RT}{F}\ln\left(\frac{[B]}{[A]}\right) \tag{6.29}$$

where $E_f^0\left(A/B\right)$ is the formal potential of the A/B couple if the reaction is analysed simply as the basis of the reaction

$$A = B + e^{-} \tag{6.30}$$

Thus,

$$E_f^0(A/B/H^{+}) = E_f^0\left(A/B\right) + 2.303\frac{mRT}{F}\times pH \tag{6.31}$$

For Eq. (6.27), the Butler-Volmer kinetic equation is

$$j = k^0 e^{\frac{\beta F}{RT}\left[E - E_f^0(A/B/H^{+})\right]} = k^0 e^{\frac{\beta F}{RT}\left[E - E_f^0(A/B)\right]} e^{-m\beta \ln\left[H^{+}\right]} = \frac{k^0}{\left[H^{+}\right]^{m\beta}} e^{\frac{\beta F}{RT}\left[E - E_f^0(A/B)\right]} \tag{6.32}$$

where j is the flux and k^0 the standard electrochemical standard rate constant. Hence, j increases as the proton concentration $\left[H^{+}\right]$ decreases corresponding to an enhanced thermodynamic “driving force” for Eq. (6.27). It follows that if $\left[H^{+}\right]$ is modelled as a simple one-electron concentration of A to B that the effective standard electrochemical rate constant is shown to be pH-dependent given by

$$k_{eff}^{0}=\frac{k^{0}}{\left[H^{+}\right]^{m\beta}} \tag{6.33}$$

In the case of the four-electron oxidation of hydrazine or protonated hydrazine,

$$j=\frac{4k^{0}}{\left[H^{+}\right]^{m\beta}}e^{\frac{\beta F}{RT}\left(E-E_{f}^{0}\right)} \tag{6.34}$$

where E_{f}^{0} is the formal potential of the first rate determining electron transfer as

$$N_2H_4\xrightarrow{rds}X+e \tag{6.35}$$

$$X\xrightarrow{fast}N_2+4H^{+}+3e \tag{6.36}$$

In the main text the effective standard electrochemical rate constant for the oxidation of $N_2H_5^{+}$ and N_2H_4 are shown to be pH-insensitive, showing, on the voltammetric timescale (see main text) that $m\simeq 0$ and no protons are released in the first electron transfer, namely a = 0 and b = 0 in the Appendix Section A6.4. Thus, the realistic mechanism of hydrazine oxidation is given by

$$N_2H_5^{+}\rightleftarrows N_2H_4+H^{+} \tag{6.37}$$

$$N_2H_5^{+}\xrightarrow{rds}N_2H_5^{2+}+e^{-} \tag{6.38}$$

$$N_2H_5^{2+}\xrightarrow{fast}N_2+5H^{+}+3e^{-} \tag{6.39}$$

$$N_2H_4\xrightarrow{rds}N_2H_4^{+}+e^{-} \tag{6.40}$$

$$N_2H_4^{+}\xrightarrow{fast}N_2+4H^{+}+3e^{-} \tag{6.41}$$

References

[1] R. Miao, L. Shao, R.G. Compton, Single entity electrochemistry and the electron transfer kinetics of hydrazine oxidation, Nano Research, (2021).

[2] C.-H. Chen, L. Jacobse, K. McKelvey, S.C. Lai, M.T. Koper, P.R. Unwin, Voltammetric scanning electrochemical cell microscopy: dynamic imaging of hydrazine electro-oxidation on platinum electrodes, Analytical Chemistry, 87 (2015) 5782-5789.

[3] F.A. Harraz, A.A. Ismail, S. Al-Sayari, A. Al-Hajry, M. Al-Assiri, Highly sensitive amperometric hydrazine sensor based on novel α-Fe_2O_3/crosslinked polyaniline nanocomposite modified glassy carbon electrode, Sensors and Actuators B: Chemical, 234 (2016) 573-582.

[4] T. Wang, Q. Wang, Y. Wang, Y. Da, W. Zhou, Y. Shao, D. Li, S. Zhan, J. Yuan, H. Wang, Atomically Dispersed Semimetallic Selenium on Porous Carbon Membrane as an Electrode for Hydrazine Fuel Cells, Angewandte Chemie, 131 (2019) 13600-13605.

[5] Z. Lu, M. Sun, T. Xu, Y. Li, W. Xu, Z. Chang, Y. Ding, X. Sun, L. Jiang, Superaerophobic electrodes for direct hydrazine fuel cells, Advanced Materials, 27 (2015) 2361-2366.

[6] T. Sakamoto, K. Asazawa, U. Martinez, B. Halevi, T. Suzuki, S. Arai, D. Matsumura, Y. Nishihata, P. Atanassov, H. Tanaka, Electrooxidation of hydrazine hydrate using Ni–La catalyst for anion exchange membrane fuel cells, Journal of Power Sources, 234 (2013) 252-259.

[7] B.M. Lindley, A.M. Appel, K. Krogh-Jespersen, J.M. Mayer, A.J. Miller, Evaluating the thermodynamics of electrocatalytic N_2 reduction in acetonitrile, ACS Energy Letters, 1 (2016) 698-704.

[8] D.R. Lide, CRC Handbook of Chemistry and Physics, CRC Press, 2004.

[9] H. Hall Jr, Correlation of the base strengths of amines1, Journal of the American Chemical Society, 79 (1957) 5441-5444.

[10] S. Karp, L. Meites, The voltammetric characteristics and mechanism of electrooxidation of hydrazine, Journal of the American Chemical Society, 84 (1962) 906-912.

[11] B. Alvarez-Ruiz, R. Gomez, J. Orts, J. Feliu, Role of the metal and surface structure in the electro-oxidation of hydrazine in acidic media, Journal of the Electrochemical Society, 149 (2002) D35.

[12] L. Burke, J. Casey, The electrocatalytic behaviour of palladium in acid and base, Journal of Applied Electrochemistry, 23 (1993) 573-582.

[13] R. Miao, L. Chen, R.G. Compton, Electro-oxidation of hydrazine shows Marcusian electron transfer kinetics, Science China Chemistry, 64 (2021) 322-329.

[14] Y. Wang, E. Laborda, K. Tschulik, C. Damm, A. Molina, R.G. Compton, Strong negative nanocatalysis: oxygen reduction and hydrogen evolution at very small (2 nm) gold nanoparticles, Nanoscale, 6 (2014) 11024-11030.

[15] Y. Wang, K.R. Ward, E. Laborda, C. Salter, A. Crossley, R.M. Jacobs, R.G. Compton, A joint experimental and computational search for authentic nano-electrocatalytic effects: electrooxidation of nitrite and L-ascorbate on gold nanoparticle-modified glassy carbon electrodes, Small, 9 (2013) 478-486.

[16] W. Yang, X. Liu, X. Yue, J. Jia, S. Guo, Bamboo-like carbon nanotube/Fe_3C nanoparticle hybrids and their highly efficient catalysis for oxygen reduction, Journal of the American Chemical Society, 137 (2015) 1436-1439.

[17] E. Kätelhön, L. Chen, R.G. Compton, Nanoparticle electrocatalysis: Unscrambling illusory

inhibition and catalysis, Applied Materials Today, 15 (2019) 139-144.

[18] L. Chen, E. Kätelhön, R.G. Compton, Particle-modified electrodes: General mass transport theory, experimental validation, and the role of electrostatics, Applied Materials Today, 18 (2020) 100480.

[19] I. Streeter, G.G. Wildgoose, L. Shao, R.G. Compton, Cyclic voltammetry on electrode surfaces covered with porous layers: an analysis of electron transfer kinetics at single-walled carbon nanotube modified electrodes, Sensors and Actuators B: Chemical, 133 (2008) 462-466.

[20] M.C. Henstridge, E.J. Dickinson, M. Aslanoglu, C. Batchelor-McAuley, R.G. Compton, Voltammetric selectivity conferred by the modification of electrodes using conductive porous layers or films: the oxidation of dopamine on glassy carbon electrodes modified with multiwalled carbon nanotubes, Sensors and Actuators B: Chemical, 145 (2010) 417-427.

[21] M.J. Sims, N.V. Rees, E.J. Dickinson, R.G. Compton, Effects of thin-layer diffusion in the electrochemical detection of nicotine on basal plane pyrolytic graphite (BPPG) electrodes modified with layers of multi-walled carbon nanotubes (MWCNT-BPPG), Sensors and Actuators B: Chemical, 144 (2010) 153-158.

[22] S. Stankovich, D.A. Dikin, R.D. Piner, K.A. Kohlhaas, A. Kleinhammes, Y. Jia, Y. Wu, S.T. Nguyen, R.S. Ruoff, Synthesis of graphene-based nanosheets via chemical reduction of exfoliated graphite oxide, carbon, 45 (2007) 1558-1565.

[23] G. Eda, G. Fanchini, M. Chhowalla, Large-area ultrathin films of reduced graphene oxide as a transparent and flexible electronic material, Nature nanotechnology, 3 (2008) 270-274.

[24] G. Eda, M. Chhowalla, Chemically derived graphene oxide: towards large-area thin-film electronics and optoelectronics, Advanced Materials, 22 (2010) 2392-2415.

[25] K.J. Stevenson, K. Tschulik, A materials driven approach for understanding single entity nano impact electrochemistry, Current Opinion in Electrochemistry, 6 (2017) 38-45.

[26] W. Xu, G. Zou, H. Hou, X. Ji, Single particle electrochemistry of collision, Small, 15 (2019) 1804908.

[27] S.V. Sokolov, S. Eloul, E. Kätelhön, C. Batchelor-McAuley, R.G. Compton, Electrode–particle impacts: a user's guide, Physical Chemistry Chemical Physics, 19 (2017) 28-43.

[28] X. Li, C. Batchelor-McAuley, S.A. Whitby, K. Tschulik, L. Shao, R.G. Compton, Single nanoparticle voltammetry: contact modulation of the mediated current, Angewandte Chemie International Edition, 55 (2016) 4296-4299.

[29] J. Ellison, C. Batchelor-McAuley, K. Tschulik, R.G. Compton, The use of cylindrical micro-wire electrodes for nano-impact experiments; facilitating the sub-picomolar detection of single nanoparticles, Sensors and Actuators B: Chemical, 200 (2014) 47-52.

[30] E. Kätelhön, E.E. Tanner, C. Batchelor-McAuley, R.G. Compton, Destructive nano-impacts: What information can be extracted from spike shapes?, Electrochimica Acta, 199 (2016) 297-304.

[31] R. Miao, L. Chen, L. Shao, B. Zhang, R.G. Compton, Electron transfer to decorated graphene oxide particles, Angewandte Chemie International Edition, 58 (2019) 12549-12552.

[32] Y. Xie, J. Wang, X. Huang, B. Luo, W. Yu, L. Shao, Palladium nanoparticles supported on graphene sheets incorporating boron oxides (B_xO_y) for enhanced formic acid oxidation, Electrochemistry Communications, 74 (2017) 48-52.

[33] A. Krittayavathananon, P. Srimuk, S. Luanwuthi, M. Sawangphruk, Palladium nanoparticles decorated on reduced graphene oxide rotating disk electrodes toward ultrasensitive hydrazine

detection: effects of particle size and hydrodynamic diffusion, Analytical Chemistry, 86 (2014) 12272-12278.

[34] A. Ejaz, M.S. Ahmed, S. Jeon, Highly efficient benzylamine functionalized graphene supported palladium for electrocatalytic hydrazine determination, Sensors and Actuators B: Chemical, 221 (2015) 1256-1263.

[35] R. Chinchilla, C. Najera, Chemicals from alkynes with palladium catalysts, Chemical Reviews, 114 (2014) 1783-1826.

[36] A. Serov, C. Kwak, Direct hydrazine fuel cells: A review, Applied Catalysis B: Environmental, 98 (2010) 1-9.

[37] J.-H. Zhang, Y.-G. Zhou, Nano-impact electrochemistry: Analysis of single bioentities, TRAC Trends in Analytical Chemistry, 123 (2020) 115768.

[38] W. Cheng, R.G. Compton, Electrochemical detection of nanoparticles by ‘nano-impact’ methods, TRAC Trends in Analytical Chemistry, 58 (2014) 79-89.

[39] H. Hodson, X. Li, C. Batchelor-McAuley, L. Shao, R.G. Compton, Single nanotube voltammetry: current fluctuations are due to physical motion of the nanotube, The Journal of Physical Chemistry C, 120 (2016) 6281-6286.

[40] W.J. Albery, Electrode Kinetics, Oxford University Press, 1975.

[41] R.G. Compton, C.E. Banks, Understanding Voltammetry, World Scientific, 2018.

[42] R. Guidelli, R.G. Compton, J.M. Feliu, E. Gileadi, J. Lipkowski, W. Schmickler, S. Trasatti, Defining the transfer coefficient in electrochemistry: An assessment (IUPAC Technical Report), Pure and Applied Chemistry, 86 (2014) 245-258.

[43] M. Ram, J.T. Hupp, Linear free energy relations for multielectron transfer kinetics: a brief look at the Broensted/Tafel analogy, Journal of Physical Chemistry, 94 (1990) 2378-2380.

[44] I.J. Cutress, R.G. Compton, Theory of square, rectangular, and microband electrodes through explicit GPU simulation, Journal of Electroanalytical Chemistry, 645 (2010) 159-166.

[45] K. Aoki, Theory of ultramicroelectrodes, Electroanalysis, 5 (1993) 627-639.

[46] M. Rudolph, D.P. Reddy, S.W. Feldberg, A simulator for cyclic voltammetric responses, Analytical Chemistry, 66 (1994) 589A-600A.

[47] A. Szabo, D.K. Cope, D.E. Tallman, P.M. Kovach, R.M. Wightman, Chronoamperometric current at hemicylinder and band microelectrodes: Theory and experiment, Journal of Electroanalytical Chemistry and Interfacial Electrochemistry, 217 (1987) 417-423.

[48] P.M. Kovach, W.L. Caudill, D.G. Peters, R.M. Wightman, Faradaic electrochemistry at microcylinder, band, and tubular band electrodes, Journal of Electroanalytical Chemistry and Interfacial Electrochemistry, 185 (1985) 285-295.

[49] R.J. Forster, Microelectrodes: new dimensions in electrochemistry, Chemical Society Reviews, 23 (1994) 289-297.

[50] V. Rosca, M. Duca, M.T. de Groot, M.T. Koper, Nitrogen cycle electrocatalysis, Chemical Reviews, 109 (2009) 2209-2244.

[51] N.V. Rees, R.G. Compton, Carbon-free energy: a review of ammonia-and hydrazine-based electrochemical fuel cells, Energy & Environmental Science, 4 (2011) 1255-1260.

[52] G. Kokkinidis, P. Jannakoudakis, Influence of the electrosorption of heavy metals on hydrazine oxidation on platinum, Journal of Electroanalytical Chemistry and Interfacial Electrochemistry, 130 (1981) 153-162.

[53] A. Bard, Chronopotentiometric Oxidation of Hydrazine at a Platinum Electrode, Analytical

Chemistry, 35 (1963) 1602-1607.

Chapter 7

Catalytic Hydrazine Oxidation at Bulk Palladium

Hydrazine oxidation at the composite materials Pd/GO has been studied in the last chapter. In this chapter, the mechanism of the catalytic oxidation of hydrazine at Palladium (Pd) electrodes is probed in aqueous solutions between pH 2 and 11. The voltammetry recorded at pH 2 and 11 reveals that both the unprotonated hydrazine N_2H_4 and the protonated form $N_2H_5^+$ are electro-active at the Pd surface in contrast to glassy carbon (GC) where N_2H_4 is the only species which undergoes oxidation in the potential range of 0.2 to 1.0 V (vs the Saturated Calomel Electrode).

An unexpected reductive voltammetric wave was observed during the cyclic voltammetry of the oxidation of protonated hydrazine and concluded to originate from the reduction of a radical di-cation $N_2H_5^{\bullet 2+}$ which is stable on the voltammetric timescale. The di-cation was inferred to result from the loss of one electron from the single lone pair of electrons on $N_2H_5^+$. It is suggested that, unlike the case of N_2H_4, the absence of a lone pair on the N adjacent to that being oxidised as a result of protonation leads to the stability of the radical di-cation whereas in the oxidation of N_2H_4, the available adjacent lone pair facilitates rapid follow up chemical reaction leading to nitrogen formation.

The work of Chapter 7 has been published in the journal *Electrochimica Acta*[1], and was carried out under the supervision of Prof. Richard G. Compton (University of Oxford).

7.1 Introduction

The four electron electro-oxidation of hydrazine to nitrogen in aqueous solution, under alkaline conditions,

$$N_2H_4(aq) - 4e^- \rightleftarrows N_2(g) + 4H^+(aq) \tag{7.1}$$

and under acidic conditions,

$$N_2H_5^+(aq) - 4e^- \rightleftarrows N_2(g) + 5H^+(aq) \tag{7.2}$$

is of both applied and fundamental significance in respect of fuel cells [2-5] and sensors [6-9], with recent insightful contributions from Ulstrup and colleagues [2, 9]. Extensive efforts have been placed on the development of high-performance electro-catalysts towards hydrazine oxidation, especially including noble metal. For example, Wu et al. [10] reported that the catalyst palladium decorated porous nickel synthesized via de-alloying and galvanic replacement, displayed outstanding electro-catalytic properties towards hydrazine oxidation as well as good long-term durability with only 5% loss of its initial current density after 1000 cycles. Ghasemi et al. [11] fabricated an amperometric nanosensor with platinum-palladium nanoparticles decorated reduced graphene oxides, and it exhibited an excellent sensing performance with a linear response range between 0.007 - 5.5 mM and a 1.7 μM detection limit. Notwithstanding the great progress made empirically, the understanding of the mechanism of the four electron, four/five proton hydrazine oxidation remains challenging, but vital to provide generic, bottom-up guidance for catalyst design.

We have recently explored the hydrazine oxidation at glassy carbon electrodes [12, 13] as described in Chapters 4 and 5 in aqueous solutions where the following equilibrium is important

$$N_2H_5^+ \rightleftarrows N_2H_4 + H^+ \tag{7.3}$$

The work reported in Chapter 5 and elsewhere [13] demonstrated that $N_2H_5^+$ does not undergo oxidation on the surface of glassy carbon over a wide range of potentials whereas the oxidation of N_2H_4 proceeds cleanly albeit with significant over-potential. Importantly from a mechanistic perspective the protons generated from the N_2H_4 oxidation easily combine with the N_2H_4 molecules diffusing to the electrode surface, to form the inactive $N_2H_5^+$ so to inhibit the oxidation; the reaction is self-inhibiting. This highlights the importance of understanding the chemistry occurring at the catalyst surface as well as the intrinsic electron transfer details. Accordingly, herein we study the electron transfer behaviour of N_2H_4 and $N_2H_5^+$ at the noble metal Pd electrodes in aqueous solutions from pH 2 to 11. It was found that both species are fully *electro-active* at Pd, and notably, a *long-lived* radical di-cation $N_2H_5^{\bullet 2+}$ is generated from the oxidation of $N_2H_5^+$ and has a finite lifetime on the voltammetric timescale (*ca.* seconds). Its existence is likely attributed to the fact that the lone pair on the N adjacent to that being oxidised is pronated and so not available for immediate further reaction in contrast to the oxidation of N_2H_4.

7.2 Experimental

An aqueous solution of 1.5 mM hydrazine supported by 0.1 M KNO_3 was prepared, of which the pH was measured to be 9.7. Comparable hydrazine solutions of pH 2.0, 5.0, 6.0 and 7.0 were made by additions of tiny amounts of HNO_3 for pH adjustment. A phosphate buffer solution (PBS, 0.1 M, pH 11.0) with 1.5 mM hydrazine was prepared via mixing K_2HPO_4, KH_2PO_4 and hydrazine in water [14]. All pH measurements were made with a digital pH meter (sensION^{TM}+ pH 31) purchased from HACH, Colorado, USA. The electrochemical cell consisted of three electrodes: palladium (Pd, diameter in 3.01 mm) or glassy carbon (GC, diameter in 2.95 mm) macrodisc working electrodes, a saturated calomel reference electrode (SCE) and a graphite rod counter electrode. Then cyclic voltammetry (CV) measurements were conducted in the above-mentioned solutions that were vigorously degassed with N_2 for 15 min so to remove the dissolved oxygen prior to the measurements. The control experiments were undertaken in equivalent media but without hydrazine.

7.3 Results and Discussion

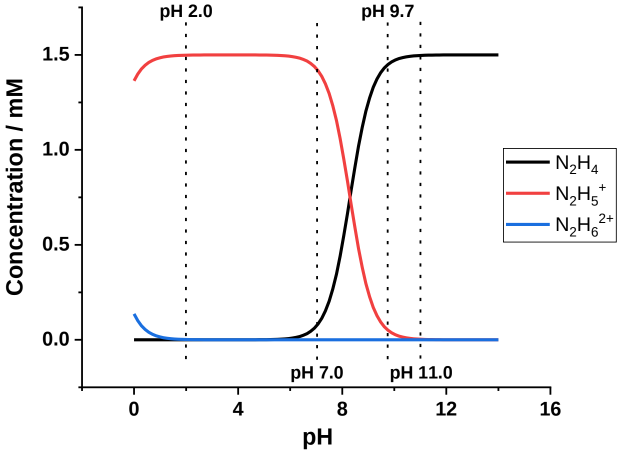

Figure 7.1. The speciation of hydrazine calculated as a function of pH in pure water. Black/Red/Blue lines correspond to the concentrations of N_2H_4, $N_2H_5^+$ and $N_2H_6^{2+}$ respectively.

In aqueous solution hydrazine, N_2H_4, acts as a base, the conjugate acid of which has a pK_a value of *ca.* 8.1 at 25 °C [15-18]. Thus at low pH the molecule exists in its protonated form, $N_2H_5^+$, the hydrazinium cation. At extremely low pH this is further protonated to form $N_2H_6^{2+}$ with a pK_a of *ca.* -1.0 [19-21]. Figure 7.1 shows how the speciation of a solution of hydrazine varies with pH. In particular at pH 2 the composition is almost entirely $N_2H_5^+$ whereas at pH 11.0 it is overwhelmingly N_2H_4. At pH values of 7 and 9.7 both N_2H_4 and $N_2H_5^+$ co-exist.

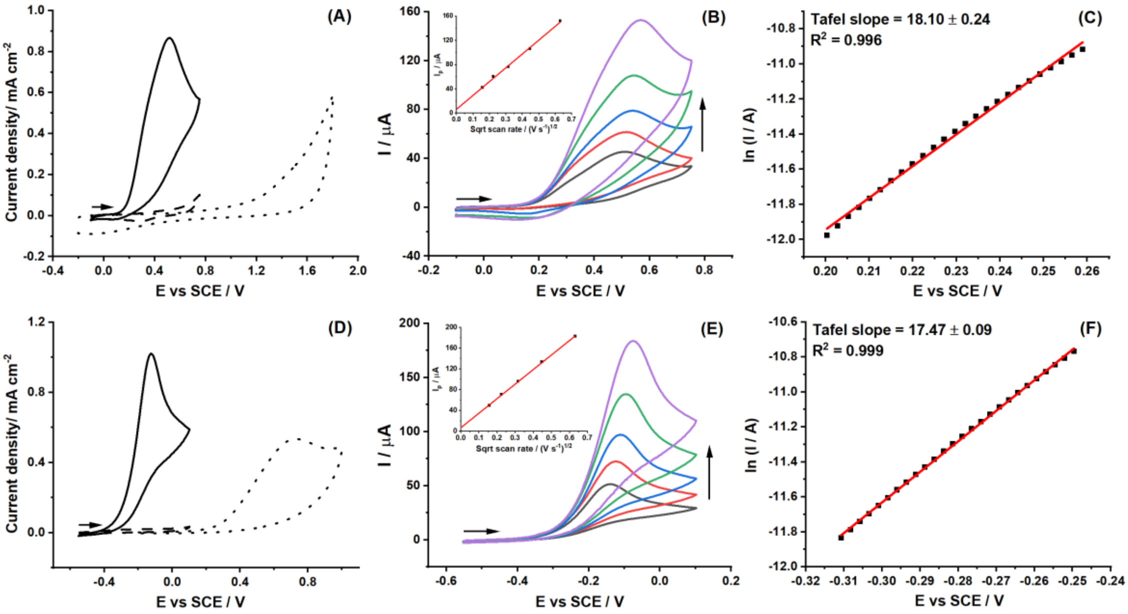

Figure 7.2. (A) and (D) Voltammograms measured at 50 mV/s in 0.1 M KNO_3 of pH 2 and 0.1 M PBS of pH 11 respectively: with 1.5 mM hydrazine at a Pd electrode (solid line), without hydrazine at a Pd electrode (dash line) and with 1.5 mM hydrazine at a GC electrode (dot line). (B) and (E) Scan rate study (25/50/100/200/400 mV/s) in 0.1 M KNO_3 of pH 2 and 0.1 M PBS of pH 11 respectively with 1.5 mM hydrazine at a Pd electrode. The insets are the plots of peak current I_p versus square root of scan rate. (C) and (F) Tafel analysis in the region of 10% to 30% of the oxidative peaks in 0.1 M KNO_3 of pH 2 and 0.1 M PBS of pH 11 respectively with 1.5 mM hydrazine at a Pd electrode. The transverse arrows indicate the start potentials and directions of the voltametric scans. The vertical arrows indicate increasing scan rates.

The comparative electro-catalysis towards hydrazine oxidation was first investigated at Palladium (Pd) and Glassy Carbon (GC) macrodisc electrodes in 1.5 mM hydrazine supported by 0.1 M KNO_3 of pH 2. The pH was controlled by the addition of tiny amounts of HNO_3. As discussed above, under these conditions, protonated hydrazine $N_2H_5^+$ accounts for almost 100% of the hydrazine speciation. The recorded cyclic voltammograms are shown in Figure 7.2A. Considering the Pd electrode, a fully electrochemically and chemically irreversible oxidative wave (solid line) is observed at a peak potential of *ca.* 0.52 V vs SCE with a current density of 0.87 mA cm^{-2} at 50 mV/s in the presence of hydrazine whereas no voltammetric features (dash line) are observed in the absence of hydrazine, indicating the significant anodic current results from the oxidation of $N_2H_5^+$ which is well documented to form exclusively N_2 and protons [22, 23]. The dotted curve recorded at the GC electrode clearly shows no oxidative signals of hydrazine, in agreement with our previous work and as described in Chapter 5 [13] that concluded that $N_2H_5^+$ is fully electro-*inactive* at all potentials in the range studied at a GC electrode. This demonstrates the *effective* catalysis of Pd towards the oxidation of $N_2H_5^+$. The scan rate study at the Pd electrode is depicted in Figure 7.2B where the peak current after baseline correction (but without correction for ohmic drop) is seen to be linearly proportional to the square root of scan rate, signalling it is a diffusion-controlled process [24]. Tafel analysis was conducted to extract the Butler-Volmer anodic transfer coefficient β for $N_2H_5^+$ oxidation from the voltammogram (solid line in Figure 7.2A). The region from 10% to 30% of the oxidative peak current was taken for analysis where the mass transport effects can be ignored [25]. The result after baseline correction is displayed in Figure 7.2C that gives a transfer coefficient $\beta_{N_2H_5^+}$ value of 0.46 ± 0.01 from the Tafel slope for the oxidation of the hydrazinium cation indicating that removal of the first electron is the rate determining step of the oxidation.

Analogous experiments to those above were performed at both Pd and GC electrodes in 0.1 M PBS of pH 11, where nearly all the hydrazine present exists in the unprotonated form N_2H_4. Figure 7.2D shows a fully chemically and electrochemically irreversible voltammetric wave (solid line) at a peak potential of *ca.* -0.12 V vs SCE with a current density of 1.02 mA cm^{-2} for the oxidation of N_2H_4 at the Pd electrode at a scan rate of 50 mV/s. Note that the blank, containing no hydrazine, experiment (dash line) shows no corresponding features. At the GC electrode, an electrochemically irreversible wave with a current density of 0.53 mA cm^{-2} was observed at a peak potential of *ca.* 0.73 V vs SCE indicating the oxidation of N_2H_4 to nitrogen

[12,26]. Comparison of the voltammograms for the oxidation of N_2H_4 at Pd and GC (Figure 7.2D) shows that significantly higher overpotential is required at the GC surface than Pd, evidencing Pd to be an *effective* electro-catalyst towards N_2H_4 oxidation. The oxidation is again diffusional as inferred from the peak current (after baseline correction) versus scan rate plot shown in Figure 7.2E and a value of the transfer coefficient $\beta_{N_2H_4}$ (0.45 ± 0.01) was obtained via the Tafel analysis in Figure 7.2F.

Having evidenced the catalytic ability of Pd towards the oxidation of both N_2H_4 and $N_2H_5^+$, voltammetry was then conducted without the addition of acids or bases. In particular we studied 0.1 M KNO_3 with 1.5 mM added hydrazine. This solution had a measured pH of 9.7 reflecting the equilibrium

$$N_2H_4 + H_2O \rightleftharpoons N_2H_5^+ + OH^- \tag{7.4}$$

The measured pH was used to estimate the pK_a of hydrazine in 0.1 M KNO_3 giving a value of 8.3 ± 0.1 which is close to that cited above but there applying to pure water. The discrepancy can be attributed to a small thermodynamic salt effect [27-29].

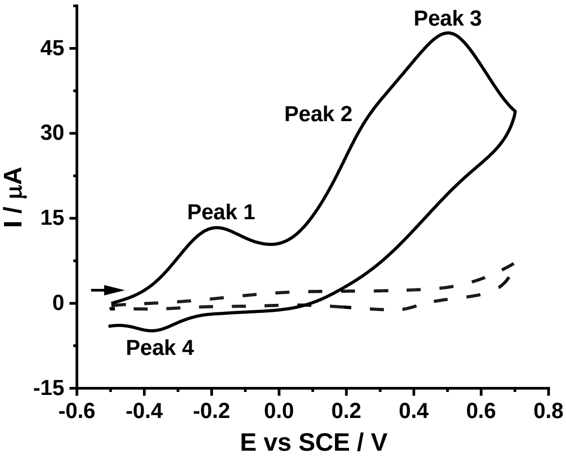

Figure 7.3. Voltammogram (solid line) recorded in 0.1 M KNO_3 with 1.5 mM hydrazine (no buffering, measured pH 9.7) at a Pd electrode at 50 mV/s. Also shown is the voltammogram (dash line) under the same conditions but without hydrazine. The transverse arrow indicates the start potential and direction of the voltametric scans.

The voltammetry (solid line) was recorded as illustrated in Figure 7.3, of which three oxidative peaks, and most unexpectedly a hitherto unexpected reductive peak, are clearly seen (labelled in order of the voltammetric scan) in the presence of hydrazine, while there are no voltammetric features seen without hydrazine present (dash line). The peak potentials of Peaks 1, 2, 3 and 4 are *ca.* -0.17, 0.26, 0.50 and -0.37 V vs SCE respectively at the scan rate of 50 mV/s.

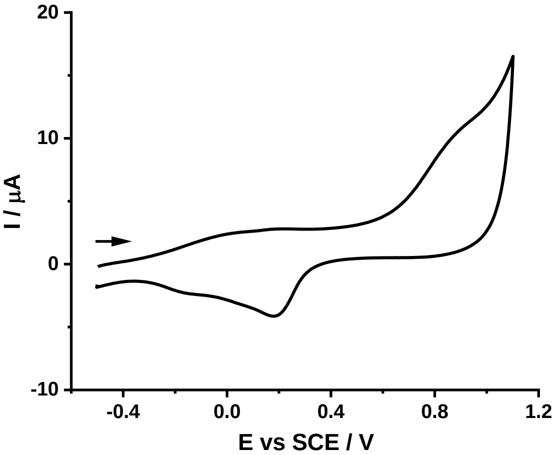

Figure 7.4. Voltammograms recorded in 0.1 M KNO_3 (no buffering, pH 9.7) at a Pd electrode at 50 mV/s. The transverse arrow indicates the start potential and direction of the voltametric scan.

It has been reported [30, 31] in the case of the oxidation of hydrazine at platinum electrodes that surface oxides are crucial to the electrocatalysis. So to explore this possibility voltammetry was conducted in the absence of hydrazine at the Pd electrode. As illustrated in Figure 7.4, a quasi-irreversible oxidative peak is seen at a peak potential of *ca.* 0.88 V vs SCE. It is clear that the formation of Palladium oxides (PdO) requires a much higher overpotential than hydrazine oxidation (solid line in Figure 7.2A) under these conditions. It follows that Peaks 1, 2, 3 and 4 on Figure 7.3 are not related to the formation or stripping of PdO, the involvement of which in the hydrazine oxidation were thus discounted, in contrast to the case of Platinum electrodes. The details on the formation of PdO at pH 2, 7 and 11 are presented in the Appendix Section A7.1. Again there is no involvement of palladium oxides in hydrazine oxidation at these pH values.

Returning to Figure 7.3, it is noticeable that Peaks 1 and 3 show complete consistency in peak potential with the oxidative peaks of N_2H_4 (solid line in Figure 7.2A) and $N_2H_5^+$ (solid line in Figure 7.2D) respectively. Hence, it is inferred that Peak 1 corresponds to the *direct* oxidation of N_2H_4 while Peak 3 is assigned to the *direct* oxidation of $N_2H_5^+$ as follows:

Peak 1:

$$N_2H_4 \xrightarrow{-4e^-} N_2 + 4H^+ \tag{7.5}$$

Peak 3:

$$N_2H_5^+ \xrightarrow{-4e^-} N_2 + 5H^+ \tag{7.6}$$

It is well-known that the chemical equilibrium between the two hydrazine species, protonated or unprotonated, acts in parallel with the electron transfer reactions [32-34]. Importantly the protons from hydrazine oxidation can significantly change the local pH thus in turn affecting the oxidation process [13]. Hence, we infer that Peak 2 likely corresponds to the prior dissociation of $N_2H_5^+$ to N_2H_4 followed by oxidation of the produced N_2H_4 as follows, and to be distinguished from the direct oxidation of N_2H_4 assigned to Peak 1:

Peak 2:

$$N_2H_5^+ \rightleftarrows N_2H_4 + H^+ \tag{7.7}$$

$$N_2H_4 \xrightarrow{-4e^-} N_2 + 4H^+ \tag{7.8}$$

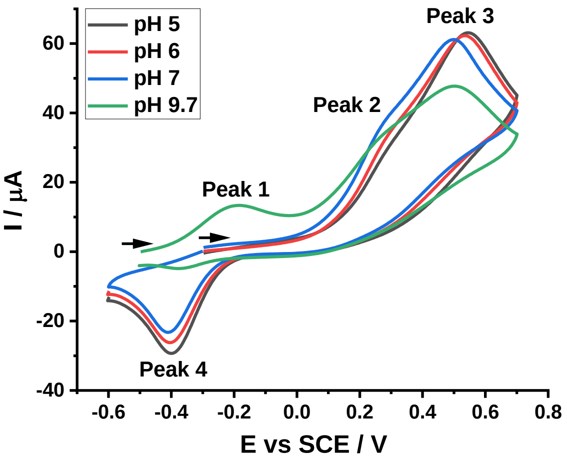

Figure 7.5. Voltammograms recorded in 0.1 M KNO_3 with 1.5 mM hydrazine of different pHs (pH 5/6/7/9.7) at a Pd electrode at 50 mV/s. The transverse arrows indicate the start potentials and directions of the voltammetric scans.

A pH study of the hydrazine oxidation was then performed so to further clarify the peak information. The electrolytes in support of 1.5 mM hydrazine were unbuffered, 0.1 M KNO_3, of which the pHs were controlled by additions of tiny amounts of nitric acid so as to realise bulk pH values of 5, 6, 7 and 9.7. The results are shown in Figure 7.5. It is clear that an increase in pH leads to the increased anodic current of Peak 1 whereas that of Peak 3 is seen to decrease, in accord with the pH-dependent speciation of N_2H_4 and $N_2H_5^+$ in solutions in Figure 7.1. This is consistent with the above inference that Peaks 1 and 3 correspond to the direct oxidation of N_2H_4 and $N_2H_5^+$ respectively, and also accounts for the fact that only one peak is seen at pH 2 or pH 11 since for each there is the only active hydrazine species, $N_2H_5^+$ or N_2H_4. Meanwhile, an increasing visibility of Peak 2 is qualitatively expected as the pH rises facilitating the dissociation process, and the observed behaviour further qualitatively evidences the involvement of the chemically preceding dissociation reaction in the formation of Peak 2. Moreover, the peak separation between Peaks 1 and 2 induced by the preceding chemical reaction is measured to be *ca.* 0.38 to 0.49 V, where the uncertainty reflects the fact that Peak 2 appears as a shoulder on Peak 3, thus generating an *effective* dissociation constant $K_{a,eff}$ value of approximately 3.3×10^{-4} M to 2.0×10^{-3} M where $K_{a,eff}$ is the product of the true K_a divided by the local proton concentration $K_{a,eff} = K_a \big/ \left[H^+\right]_{local}$ (see Appendix Section A7.2). The latter varies at different potentials on the oxidative wave but a value of *ca.* 10^{-3} M for the local proton concentration in the vicinity of the peak can be inferred suggesting that the estimated value is not inconsistent with the reported value of K_a (8.5×10^{-7} M) [35, 36]. This value quantitatively reflects the role of the chemical equilibrium and local pH change in the oxidation of N_2H_4 and the suggested origin of Peak 2.

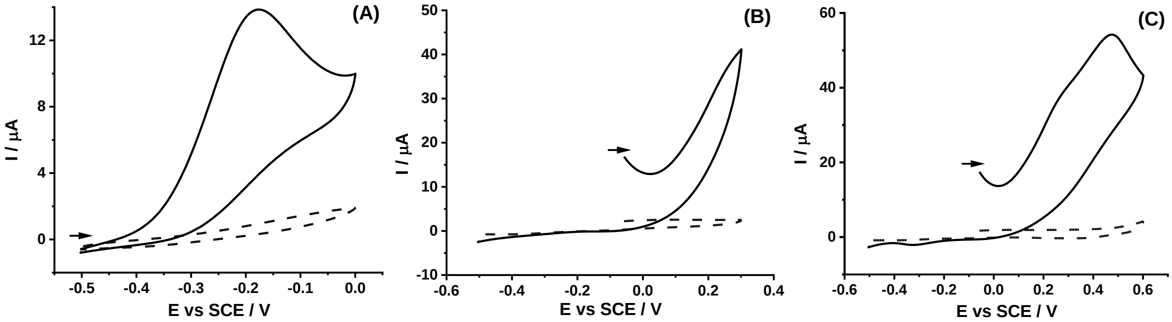

Figure 7.6. Voltammograms (solid line) recorded in 0.1 M KNO_3 with 1.5 mM hydrazine (no buffering, measured pH 9.7) at a Pd electrode at 50 mV/s within different potential windows: (A) scan from -0.5 V anodically to 0 then cathodically to -0.5 V, (B) scan from -0.05 V anodically to 0.3 V then cathodically to -0.5 V and (C) scan from -0.05 V anodically to 0.6 V then cathodically to -0.5 V. Also shown are voltammograms (dash line) under the same conditions but without hydrazine. The transverse arrows indicate the start potentials and directions of the voltametric scans.

Next the focus was turned to the investigation of the novel Peak 4 in Figure 7.3. A series of variable potential window experiments were carried out to probe into the origin of Peak 4. The voltammetric curve in Figure 7.6A was scanned from a start potential of -0.5 V to 0 V at which point it was reversed to -0.5 V. The scan shows *only* an oxidative peak with a current of 13.8 μA at a peak potential of -0.17 V vs SCE (50 mV/s), fully consistent with Peak 1 (Figure 7.3). The absence of a back peak indicates no causal connection between Peaks 1 and 4 (Figure 7.3). Figure 7.6B displays a voltammogram that starts at -0.05 V then scans anodically to 0.3 V and ends at -0.5 V so as to explore any causal relation between peak 4 with peak 2. Again no back peak was observed leading to the conclusion that the reductant for Peak 4 does not originate from the products of Peak 2 which as discussed above relates to the oxidation of N_2H_4 formed by dissociation of $N_2H_5^+$. Then in a third experiment the potential upper vertex was extended to 0.6 V to encompass the direct oxidation of $N_2H_5^+$ (Peak 3) and voltammetry was recorded as presented in Figure 7.6C. Two obvious oxidative peak are observed at peak potentials of *ca.* 0.26 V and 0.48 V matching with Peaks 2 and 3 (Figure 7.3) respectively. Notably a reductive peak appears at *ca.* -0.33 V which is comparable with Peak 4 in Figure 7.3. Therefore, the reductant for Peak 4 is the product from the direct oxidation of $N_2H_5^+$ (Peak 3). The details of the full scan rate study at pH 9.7 within the variable potential windows are given in Figure 7.7. All these data point to the origin of Peak 4 resulting from the direct oxidation of $N_2H_5^+$.

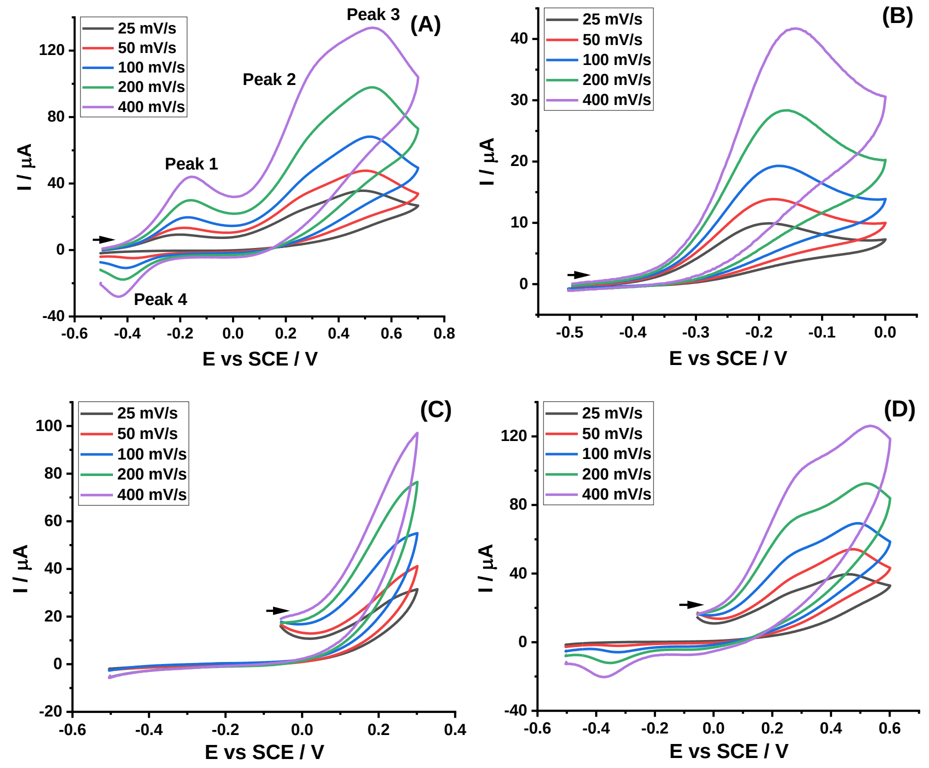

Figure 7.7. Voltammograms recorded in 0.1 M KNO_3 with 1.5 mM hydrazine (no buffering, pH 9.7) at a Pd electrode at various scan rates (25/50/100/200/400 mV/s) within different variable potential windows. The transverse arrow indicates the start potential and direction of the voltametric scans.

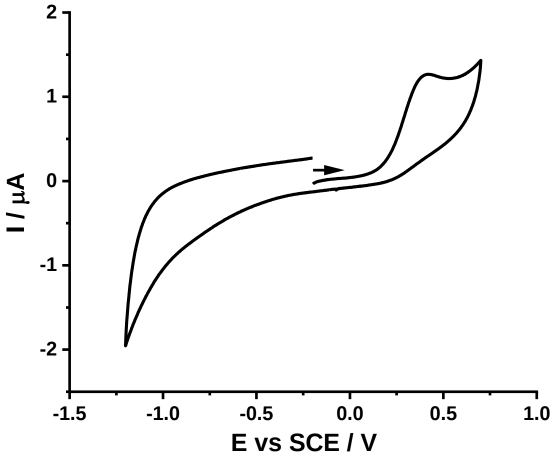

Figure 7.8. Voltammogram recoded in 0.1 M KNO_3 with 1.5 mM hydrazine (no buffering, pH 7) at a GC electrode at 50 mV/s. The transverse arrow indicates the start potential and direction of the voltammetric scan.

To further explore the origins of Peak 4, we revisited the voltammetry at a GC electrode in 1.5 mM hydrazine supported by 0.1 M KNO_3 of pH 7, since our previous work [13] as described in Chapter 5 reported that the oxidation of $N_2H_5^+$ was electro-inactive at all potentials in the range studied. Figure 7.8 shows the voltammetry where a single fully irreversible oxidative peak appears and this peak results (see above) from N_2H_4 oxidation, coincident with our reported observations [13] as given in Chapter 5. No reductive peaks were apparent correlated to the absence of any preceding hydrazinium oxidation. This again is not inconsistent with our above conclusion about Peak 4 (Figure 7.3).

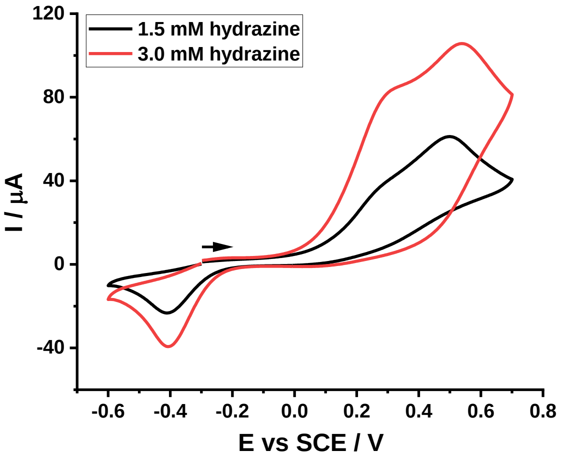

Figure 7.9. Voltammograms recorded in 0.1 M KNO_3 with 1.5 mM (black line) and 3.0 mM (red line) hydrazine (no buffering, pH 7) at a Pd electrode at 50 mV/s. The transverse arrow indicates the start potential

and direction of the voltammetric scans.

Next a concentration study of hydrazine oxidation at a Pd electrode at pH 7 was performed. The current of the peaks is seen to be doubled in size when the hydrazine concentration is doubled from 1.5 mM to 3.0 mM as shown in Figure 7.9, implying that all the peaks including peak 4 are hydrazine-related. Note that the direct oxidation of N_2H_4 is, herein, not obvious which is attributed to the very limited concentration of N_2H_4 in the solution of pH 7 (Figure 7.1). These experiments further support the idea that Peak 4 is the voltammetrically reductive feature of the $N_2H_5^+$-oxidation product.

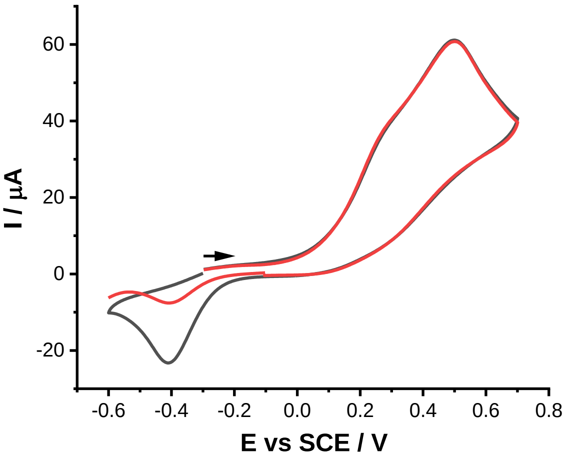

Figure 7.10. Voltammograms recorded in 0.1 M KNO_3 with 1.5 mM hydrazine (no buffering, pH 7) at a Pd electrode at 50 mV/s. Black line: a continuous scan; red line: a scan that pauses at -0.1 V for 20 seconds on the back way. The transverse arrow indicates the start potential and direction of the voltammetric scans.

Finally a 'voltammetric stop/start' study was conducted so to investigate the species which is reducing giving rise to Peak 4 (Figure 7.3). Figure 7.10 presents the comparison between a continuous voltammetric scan (black line) and a scan that pauses for 20 seconds at a potential of -0.1 V vs SCE before the reductive scan and the observation of the reduction wave (red line). A marked decrease in the reductive current is discerned after the pause, importantly, indicating the reductant is kinetically unstable on the voltammetric timescale. As is well known that the first electron transfer of hydrazine oxidation is rate-determining [37-41] and the first step involves no protons at the Pd surface [42], hence, it is inferred that the reductant for Peak 4 (Figure 7.3) is likely a radical di-cation $N_2H_5^{\bullet 2+}$ resulting from the loss of the first electron of $N_2H_5^+$, which is able to survive for a timescale of seconds. This is also confirmed by the decreasing reductive currents with the rise of pH in Figure 7.5 on account of the fact that high hydroxide concentration limits certainly the formation and probably the lifetime of $N_2H_5^{\bullet 2+}$. Note that studies at lower pH than those reported are precluded since a significant proton reduction on the electrode occurs masking the possible reductive signal of the radical di-cation and leading to the generation of hydrogen gas which distorts the voltammetry.

In the light of the evidence above, we infer that the oxidation of $N_2H_5^+$ very likely forms a radical di-cation $N_2H_5^{\bullet 2+}$ which is stable on the voltammetric timescale (*ca.* seconds). This can be rationalised via the fact that the lone pair on the N adjacent to that being oxidised is pronated and so not available for reaction. We thus further infer that for N_2H_4 the availability of the adjacent lone pair facilitates the rapid reaction following electron transfer. The possible mechanism for hydrazine oxidation at Pd electrodes is proposed as following:

Peak 1:

$$N_2H_4 \xrightarrow[slow]{-e^-} N_2H_4^{\bullet +} \xrightarrow[fast]{-3e^-} N_2 + 4H^+ \tag{7.9}$$

Peak 2:

$$N_2H_5^+ \rightleftarrows N_2H_4 + H^+ \tag{7.10}$$

$$N_2H_4 \xrightarrow[slow]{-e^-} N_2H_4^{\bullet +} \xrightarrow[fast]{-3e^-} N_2 + 4H^+ \tag{7.11}$$

Peak 3:

$$N_2H_5^+ \xrightarrow{-e^-} N_2H_5^{\bullet 2+} \xrightarrow{-3e^-} N_2 + 5H^+ \tag{7.12}$$

Peak 4:

$$N_2H_5^{\bullet 2+} \xrightarrow{+e^-} N_2H_5^+ \tag{7.13}$$

The absence of $N_2H_5^+$ voltammetry on glassy carbon is attributed to the much higher overpotential seen on that material as compared to Palladium.

7.4 Conclusions

In this chapter, the mechanism of hydrazine oxidation was studied electrochemically at both Pd and GC electrodes in solutions of different pHs (pH 2, 5, 6, 7, 9.7 and 11). It was found that both the unprotonated hydrazine N_2H_4 and the protonated form $N_2H_5^+$ are *electro-active* at the Pd electrode whereas at the GC electrode only the oxidation of N_2H_4 occurs. Notably, a hitherto unexpected reductive feature of hydrazine oxidation was observed and clarified as the reduction of a long-lived radical di-cation $N_2H_5^{\bullet 2+}$ which is stable on the voltammetric timescale (*ca.* seconds). Its existence is likely attributed to the fact that the lone pair on the N adjacent to the one being oxidised is pronated and thus not available for reaction, in contrast to N_2H_4 where the available lone pair may facilitate rapid follow up chemical reaction leading to further N-N bonding and the formation of nitrogen, as illustrated in Figure 7.11.

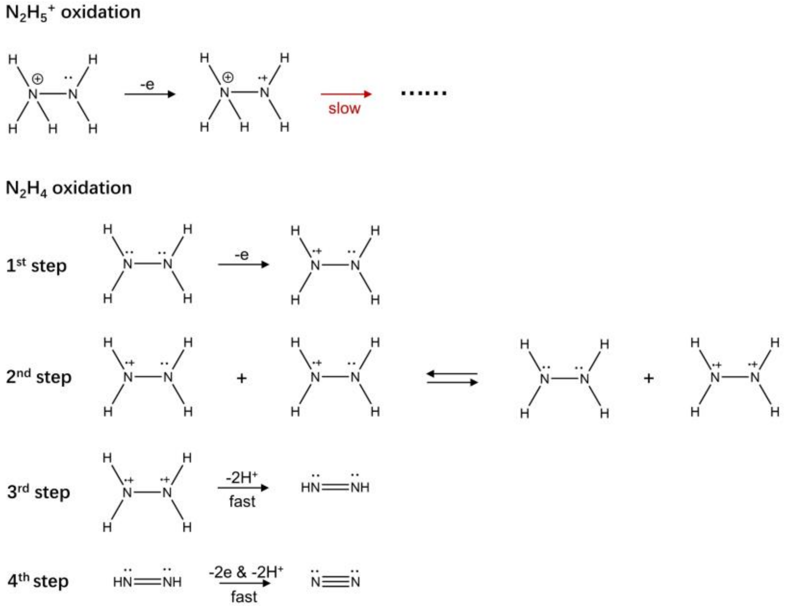

Figure 7.11. Schematic diagram for the oxidation of $N_2H_5^+$ and N_2H_4.

Appendix

Section A7.1: Palladium oxide voltammetry

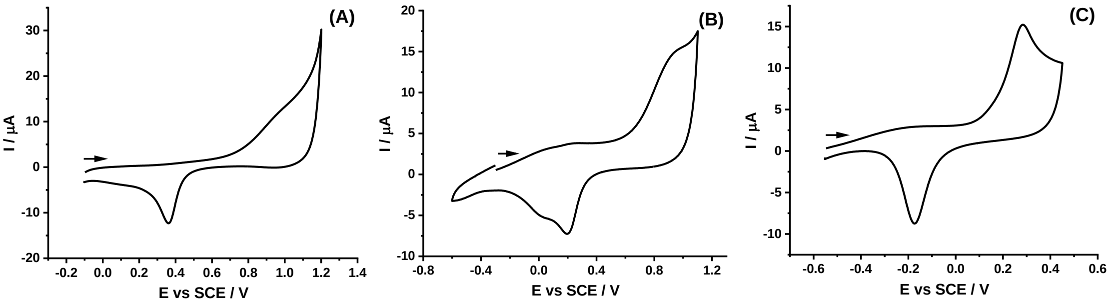

Figure A7.1. Voltammograms recorded at a Pd electrode at 50 mV/s in (A) 0.1 M KNO_3 of pH 2, (B) 0.1 M KNO_3 of pH 7 and (C) 0.1 M PBS of pH 11. The transverse arrows indicate the start potentials and directions of the voltametric scans.

Section A7.2: Calculation of the effective dissociation constant

It is argued in the main text that in Figure 7.3, Peak 1 corresponds to the direct oxidation of N_2H_4 and Peak 2 to the coupled pair of reactions consisting of a chemical dissociation reaction of $N_2H_5^+$ to N_2H_4 and then the following oxidation of the produced N_2H_4. Their mechanisms are as below:

Peak 1:

$$N_2H_4 \xrightarrow[slow]{-e^-} N_2H_4^{\bullet+} \xrightarrow[fast]{-3e^-} N_2 + 4H^+ \tag{7.14}$$

Peak 2:

$$N_2H_5^+ \rightleftarrows N_2H_4 + H^+ \tag{7.15}$$

$$N_2H_4 \xrightarrow[slow]{-e^-} N_2H_4^{\bullet+} \xrightarrow[fast]{-3e^-} N_2 + 4H^+ \tag{7.16}$$

The peak potential shift between Peaks 1 and 2 is thus attributed to the preceding chemical equilibrium. Hence this separation can be used to describe the energetics of the equilibrium.

$$\Delta E = E_{Peak\,2} - E_{Peak\,1} = -\frac{RT}{\beta F}\ln K_{a,eff} \tag{7.17}$$

where $E_{Peak\,1}$ and $E_{Peak\,2}$ are the peak potentials of Peaks 1 and 2 respectively, ΔE the peak potential separation between both peaks, R the gas constant of 8.314 J mol^{-1} K^{-1}, T the temperature of 298.15 K, β the anodic transfer coefficient of N_2H_4 oxidation with a value of 0.42 from Tafel analysis (main text), F the Faraday constant of 96,485 C mol^{-1}, and $K_{a,eff}$ is the effective dissociation constant for $N_2H_5^+$ to N_2H_4 which is the product of the true K_a divided by the local proton concentration $K_{a,eff} = K_a / \left[H^+\right]_{local}$. Note that the local proton concentration is closely related to the progress of the oxidation of hydrazine with a value of *ca.* 10^{-3} M in the vicinity of the peak position where the exact value reflects not only the oxidation of hydrazine releasing four protons but also the high diffusion coefficient of the latter in aqueous media.

ΔE was estimated from Figure 7.3 (main text) to be *ca.* 0.38 to 0.49 V where the uncertainty arises from the overlapping of Peaks 2 and 3. Hence, $K_{a,eff}$ is calculated to be 3.3×10^{-4} M to 2.0×10^{-3} M, which when corrected for the estimated local pH is consistent with the literature theoretical value of K_a (8.5×10^{-7} M) [35, 36]. This value signifies the significant effect of the preceding chemical equilibrium and local pH change as reported in our previous work [13] as described in Chapter 5.

References

[1] R. Miao, R.G. Compton, Mechanism of hydrazine oxidation at Palladium electrodes: Long-lived radical di-cation formation, Electrochim. Acta, (2021) 138655.

[2] B. Luo, T. Wu, L. Zhang, F. Diao, Y. Zhang, L. Ci, J. Ulstrup, J. Zhang, P. Si, Monometallic nanoporous nickel with high catalytic performance towards hydrazine electro-conversion and its DFT calculations, Electrochim. Acta, 317 (2019) 449-458.

[3] A. Serov, M. Padilla, A.J. Roy, P. Atanassov, T. Sakamoto, K. Asazawa, H. Tanaka, Anode catalysts for direct hydrazine fuel cells: from laboratory test to an electric vehicle, Angew. Chem., 126 (2014) 10504-10507.

[4] H. Wen, G.-X. Cao, M.-H. Chen, Y.-P. Qiu, L.-Y. Gan, P. Wang, Surface phosphorization of hierarchically nanostructured nickel molybdenum oxide derived electrocatalyst for direct hydrazine fuel cell, Appl. Catal. B, 268 (2020) 118388.

[5] Z. Lu, M. Sun, T. Xu, Y. Li, W. Xu, Z. Chang, Y. Ding, X. Sun, L. Jiang, Superaerophobic electrodes for direct hydrazine fuel cells, Adv. Mater., 27 (2015) 2361-2366.

[6] C. Saengsookwaow, R. Rangkupan, O. Chailapakul, N. Rodthongkum, Nitrogen-doped graphene–polyvinylpyrrolidone/gold nanoparticles modified electrode as a novel hydrazine sensor, Sens. Actuators B Chem., 227 (2016) 524-532.

[7] S. Mutyala, J. Mathiyarasu, Preparation of graphene nanoflakes and its application for detection of hydrazine, Sens. Actuators B Chem., 210 (2015) 692-699.

[8] Y. Liu, S.-S. Chen, A.-J. Wang, J.-J. Feng, X. Wu, X. Weng, An ultra-sensitive electrochemical sensor for hydrazine based on AuPd nanorod alloy nanochains, Electrochim. Acta, 195 (2016) 68-76.

[9] M. Zhang, A. Halder, C. Hou, J. Ulstrup, Q. Chi, Free-standing and flexible graphene papers as disposable non-enzymatic electrochemical sensors, Bioelectrochemistry, 109 (2016) 87-94.

[10] L.-S. Wu, X.-P. Wen, H. Wen, H.-B. Dai, P. Wang, Palladium decorated porous nickel having enhanced electrocatalytic performance for hydrazine oxidation, J. Power Sources, 412 (2019) 71-77.

[11] S. Ghasemi, S.R. Hosseini, F. Hasanpoor, S. Nabipour, Amperometric hydrazine sensor based on the use of Pt-Pd nanoparticles placed on reduced graphene oxide nanosheets, Microchim. Acta, 186 (2019) 1-9.

[12] R. Miao, L. Chen, R.G. Compton, Electro-oxidation of hydrazine shows Marcusian electron transfer kinetics, Sci. China Chem., 64 (2021) 322-329.

[13] R. Miao, R.G. Compton, The Electro-Oxidation of Hydrazine: A Self-Inhibiting Reaction, J. Phys. Chem. Lett., 12 (2021) 1601-1605.

[14] Potassium Phosphate Preparation, AAT Bioquest, Inc, 2021.

[15] D.R. Lide, CRC Handbook of Chemistry and Physics, CRC Press, 2004.

[16] D.L.H. Williams, Nitrosation Reactions and the Chemistry of Nitric Oxide, Elsevier, 2004.

[17] A. Radushev, L. Chekanova, V.Y. Gusev, E. Sazonova, Determination of hydrazides and 1, 2-diacylhydrazines of aliphatic carboxylic acids by conductometric titration, J. Anal. Chem., 55 (2000) 445-448.

[18] J.W. Sutherland, Pulse radiolysis of aqueous hydrazine solutions. The triazene species, J. Phys. Chem., 83 (1979) 789-795.

[19] N. Wiberg, Holleman-Wiberg's Inorganic Chemistry, Academic Press, San Diego, 2001.

[20] J.P. Schirmann, P. Bourdauducq, Hydrazine, Ullmann's Encyclopedia of Industrial Chemistry, 2000.

[21] A.Y. Zhakenovich, Y. Valentina, S.T. Tussupbayev Nessipbay, Y. Zhadyra, The Search for New Methods of Synthesis Possible of Organometallic Compounds of P, As, Sb, Bi, J. Chem. Chem. Eng., 9 (2015) 500-502.

[22] J. Zhao, M. Zhu, M. Zheng, Y. Tang, Y. Chen, T. Lu, Electrocatalytic oxidation and detection of hydrazine at carbon nanotube-supported palladium nanoparticles in strong acidic solution conditions, Electrochim. Acta, 56 (2011) 4930-4936.

[23] X. Bo, J. Bai, J. Ju, L. Guo, A sensitive amperometric sensor for hydrazine and hydrogen peroxide based on palladium nanoparticles/onion-like mesoporous carbon vesicle, Anal. Chim. Acta, 675 (2010) 29-35.

[24] R.G. Compton, C.E. Banks, Understanding Voltammetry, World Scientific, 2018.

[25] D. Li, C. Lin, C. Batchelor-McAuley, L. Chen, R.G. Compton, Tafel analysis in practice, J. Electroanal. Chem., 826 (2018) 117-124.

[26] B. Wang, X. Cao, The anodic oxidation of hydrazine on glassy carbon electrode, Electroanalysis, 4 (1992) 719-724.

[27] M. Malý, M. Boublík, M. Pocrnić, M. Ansorge, K. Lorinčíková, J. Svobodová, V. Hruška, P. Dubský, B. Gaš, Determination of thermodynamic acidity constants and limiting ionic mobilities of weak electrolytes by capillary electrophoresis using a new free software AnglerFish, Electrophoresis, 41 (2020) 493-501.

[28] J.K. Sa'ib, Titrimetric study of the solubility and dissociation of benzoic acid in water: effect of ionic strength and temperature, Am. J. Chem., 6 (2015) 429.

[29] J. Reijenga, A. Van Hoof, A. Van Loon, B. Teunissen, Development of methods for the determination of pKa values, Anal. Chem. Insights, 8 (2013) ACI. S12304.

[30] Y. Huang, J. Zhang, A. Kongkanand, F.T. Wagner, J.C. Li, J. Jorné, Transient platinum oxide formation and oxygen reduction on carbon-supported platinum and platinum-cobalt alloy electrocatalysts, J. Electrochem. Soc., 161 (2013) F10.

[31] K. Hauff, U. Tuttlies, G. Eigenberger, U. Nieken, Platinum oxide formation and reduction during NO oxidation on a diesel oxidation catalyst–Experimental results, Appl. Catal. B, 123 (2012) 107-116.

[32] V. Rosca, M. Duca, M.T. de Groot, M.T. Koper, Nitrogen cycle electrocatalysis, Chem. Rev., 109 (2009) 2209-2244.

[33] A. Serov, C. Kwak, Direct hydrazine fuel cells: A review, Appl. Catal. B, 98 (2010) 1-9.

[34] M. Petek, S. Bruckenstein, An isotopic labeling investigation of the mechanism of the electrooxidation of hydrazine at platinum: An electrochemical mass spectrometric study, J. Electroanal. Chem. Interf. Electrochem., 47 (1973) 329-333.

[35] F. Cardulla, Hydrazine, J. Chem. Educ., 60 (1983) 505.

[36] L.J. Vieland, R.P. Seward, The Electrical Conductance of Weak Acids in Anhydrous Hydrazine, J. Phys. Chem., 59 (1955) 466-469.

[37] J. Li, X. Lin, Electrocatalytic oxidation of hydrazine and hydroxylamine at gold nanoparticle—polypyrrole nanowire modified glassy carbon electrode, Sens. Actuators B Chem., 126 (2007) 527-535.

[38] M. Shamsipur, Z. Karimi, M.A. Tabrizi, A. Shamsipur, Electrocatalytic Determination of Traces of Hydrazine by a Glassy Carbon Electrode Modified with Palladium-Gold Nanoparticles,

Electroanalysis, 26 (2014) 1994-2001.

[39] P.K. Rastogi, V. Ganesan, Krishnamoorthi, Palladium nanoparticles decorated gaur gum based hybrid material for electrocatalytic hydrazine determination, Electrochim. Acta, 125 (2014) 593-600.

[40] B. Alvarez-Ruiz, R. Gomez, J. Orts, J. Feliu, Role of the metal and surface structure in the electro-oxidation of hydrazine in acidic media, J. Electrochem. Soc., 149 (2002) D35.

[41] H. Hamidi, S. Bozorgzadeh, B. Haghighi, Amperometric hydrazine sensor using a glassy carbon electrode modified with gold nanoparticle-decorated multiwalled carbon nanotubes, Mikrochim Acta, 184 (2017) 4537-4543.

[42] R. Miao, L. Shao, R.G. Compton, Single entity electrochemistry and the electron transfer kinetics of hydrazine oxidation, Nano Res., (2021).

Chapter 8

Catalytic Hydrazine Oxidation at Palladium Nanoparticles

The previous chapter reported the mechanism of hydrazine oxidation at bulk Palladium (Pd) electrodes, while in this chapter, the focus is placed on its oxidation at Pd nanoparticles. Pd nanoparticles in the form of a layer on the surface of an electrode are shown to be electro-catalytic in respect of the four-electron oxidation of hydrazine to form di-nitrogen. Quantitative voltammetry shows that the reduced over-potential in comparison with both carbon and bulk palladium electrodes partly arises from the increased surface area of the interface and partly from an increased catalytic activity of the nanoparticles relative to the bulk material. The relative catalytic activity per unit surface area of the nanoparticles as compared to the bulk material is shown to be ca. 35 - 45.

The work of Chapter 8 has been published in the journal *The Journal of Physical Chemistry Letters*[1], and was carried out under the supervision of Prof. Richard G. Compton (University of Oxford) and in collaboration with Dr. Minjun Yang (University of Oxford) who provided the SEM and TEM images of the drop-casted Pd nanoparticles.

8.1 Introduction

The search for electro-catalysts unpins vast areas of current research in electrochemistry driven by demands for new or improved energy transformation devices and for better selective and more sensitive chemical sensors[2-5]. In both areas investigations of an extraordinarily diverse range of nano-particulate materials are ubiquitous and extensively reported as can be judged from some recent reviews[6-9]. Whilst the generation of new nano-materials is seemingly boundless as judged merely from the diversity of reported shapes - cauliflowers[10], raspberries[11], sea-urchins[12] and hollow spheres[13] - and sources of origin - metals[14], blood[15], seaweed[16], pomegranate peel[17] - as recently insightfully lampooned by Pumera et al.[18] - even before the diversity of chemical composition is considered. Whilst candidate electro-catalysts abound the criteria by which electro-catalysis is judged is limited, relying primarily on voltammetric methods to probe the potential at which electrochemical reactions occur on different surfaces with a lowering of over-potential usually suggests successful catalysis. In practice however for many processes of interest such as the reductions of carbon dioxide, of di-oxygen, of nitrogen or the oxidation of carboxylic acids the electrochemistry is far from near reversible and improvements in electro-catalysts are simply benchmarked via lowered oxidation or reduction potentials.

It is usually implicit in voltammetric studies of electro-catalysts that the origin of a reduced over-potential is a change in the rate of the electrochemical reaction, specifically the rate of electron transfer at the solution-electrode interface. However voltammetric half-wave potentials and peak potentials reflect not solely the heterogeneous electron transfer rate but also the prevailing mass transport conditions. Thus for example a peak potential reflects roughly the potential at which the rates of mass transport and electron transfer balance[19, 20]. Consequently a change in a voltammetry can, and indeed often is, caused by a change in the rate of mass transport alone. Most familiarly this is seen in the shift observed in voltammetry of electrochemically irreversible processes between macro- and micro- electrodes with the enhanced local rates of diffusion to the latter creating a greater over-potential at electrodes made of the same material. The change simply reflects the physical size of the electrode, not the chemistry. More subtly, Kätelhön et al.[21] recently described the simulation of an electrode reaction at a macro-electrode which was constrained to show reversible (Nernstian) electron transfer behaviour. It was shown that if entirely inert particles showing no adsorption or electrochemistry of their own were immobilised on the surface of the electrode (thus altering the mass transport to the interface), the potential shifts at voltammetric waves would be consistent with either positive or negative electro-catalysis, depending on the size of the spheres and the voltage scan rate, despite the simulation pinning the electron transfer to be Nernstian. The shifts were related to the altered mass transport to the electrode surface as a result of the presence of the porous layers of particles and the observed responses reflected the different extent to which the diffusion layer extended into or beyond the layer of particles. Clearly the voltammetry reflected physical not chemical effects despite at first sight the shifts in the voltammetric waves signalling electro-catalysis. Similarly a simulation by Ward[22] of electrochemically irreversible processes at smooth and rough or highly porous electrodes under conditions of semi-infinite diffusion showed that a rough or porous surface could enhance the *apparent* electron transfer rate as compared to a smooth surface with a same intrinsic electrochemical rate constant by providing a greater surface area for reaction before the onset of diffusional limitations where the rate of mass transport becomes controlled by the geometric electrode area rather than the 'true' electrochemical surface area. Again this revealed a manifestation of physical not chemical catalysis.

In the present chapter we explore the use of palladium nanoparticles to alter the electro-oxidation of hydrazine, N_2H_4, as explored voltammetrically. The reaction and its electro-catalysis are of considerable importance for fuel cells[23, 24] and as a basis for chemical sensors[25, 26] given the considerable toxicity of hydrazine. In particular we consider the electrochemical responses seen at glassy carbon electrodes, at bulk palladium electrodes and at palladium nanoparticle modified electrodes of both types. The addition of the palladium particles to the electrode surface is seen to markedly lower the potentials required for the oxidation which leads to the formation of di-nitrogen. We seek to identify the cause of the potential shift and ask if this is due to altered chemistry at the nanoscale, to electrode roughness, to electrode porosity or to some combination of these.

8.2 Experimental

A phosphate buffer solution (PBS, 0.1 M, pH 7.0) with 1.5 mM hydrazine was prepared for electrochemical measurements[27]. Note that all the solutions were vigorously degassed with N_2 for 15 minutes before the electrochemical measurements. A standard three-electrode configuration was employed: a Pd macrodisc (namely Pd bulk) or GC of geometric surface area 7.07×10^{-6} m^2 as the working electrode, a saturated calomel electrode (SCE) as the reference electrode and a graphite rod as the counter electrode. The cyclic voltammetry (CV) was carried out in the abovementioned solution, and recorded via the electrochemistry software NOVA. The control experiments were conducted equivalently but without hydrazine.

Voltammetry of hydrazine oxidation at a Pd nanoparticle decorated macro-disc electrodes (GC and Pd)

Well-dispersed suspensions of Pd NPs with variable concentrations were prepared via the addition of Pd NPs into the deionized water with subsequent sonication for 15 min. 7 μL of Pd NP suspension was drop-casted onto a polished GC macrodisc electrode (of geometric surface area 7.07 × 10^{-6} m^2) and dried under a N_2 atmosphere, forming a wide range of 0.02 ~ 18 layers of Pd NPs. The modified electrode is labelled 'Pd NP/GC'. Note that the 'layers' is an estimated dropcast coverage under the assumption that the Pd NPs are spherical with a determined radius of 12.4 ± 5.4 nm and arranged in a close packed hexagonal structure. The details in the coverage and roughness estimation of the drop-casted Pd NPs are presented in the Appendix Section A8.1. Similar Pd NP drop-casting was conducted on a Pd macrodisc electrode (of geometric surface area 7.07 × 10^{-6} m^2) to form 0.02 layers and 6 layers of Pd NPs. Then the voltammetric measurements were conducted in the abovementioned solution (0.1 M PBS of pH 7.0 with 1.5 mM hydrazine) using the modified GC electrode as the working electrode. Two control experiments were performed: a bare GC electrode in the same solution, and a Pd NP modified GC electrode in the equivalent media but without hydrazine.

Analogous voltammetric experiments were conducted at a Pd NP modified Pd macro-disc electrode with the coverage of 0.02 and 6 layers. The modified electrode is labelled 'Pd NP/Pd'.

8.3 Results and Discussion

The oxidation of hydrazine was first investigated voltammetrically in 0.1 M phosphate buffer solutions (PBS) of pH 7.0 containing 1.5 mM hydrazine, at Glassy Carbon (GC) and Pd macrodisc electrodes respectively. The cyclic voltammetry was recorded as a function of voltage scan rate. A typical voltammogram is shown in Figure 8.1A for the scan rate of 50 mV/s where an electrochemically and chemically irreversible oxidative wave (solid curve) was observed at Pd macrodisc with a peak potential of ca. 0.18 V vs. SCE and a peak current of ca. 67 μA, whereas there were no voltammetric features in the absence of hydrazine (dash curve) confirming that the wave arises from the oxidation of hydrazine. At the GC surface (dot curve), as expected on the basis of the work in Chapter 5, an irreversible oxidative wave of hydrazine was also seen but with a peak potential of ca. 0.85 V vs. SCE and a peak current of ca. 27 μA. Evidently a much higher overpotential is required for the oxidation at the GC surface as compared to the bulk Pd surface, suggesting Pd is in comparison an effective electro-catalyst towards hydrazine oxidation. Then Tafel analysis was conducted upon the solid curve at the Pd surface so to extract the Butler-Volmer transfer coefficient. The plot of the natural logarithm of peak current lnI versus the applied potential E is displayed in the inset of Figure 8.1A. Note that only 10% ~ 30% of the peak current was selected for analysis to exclude the significant mass transport effect at high overpotentials.[28] The anodic transfer coefficient β was calculated to be 0.48 ± 0.01 based on the equation $\beta = Tafel\ slope \times RT/F$, where R is the gas constant, T the temperature and F the Faraday constant. The variable scan rate data at the Pd macroelectrode was then analysed and it was found that the peak current was directly proportional to the square root of scan rate as shown in Figure 8.1B. This suggests the reaction be diffusion-controlled, and meanwhile the diffusion coefficient D of hydrazine was estimated to be 1.0×10^{-5} cm^2/s according to the irreversible Randles-Ševčík equation $I_p = 2.99 \times 10^5 n \beta^{1/2} c A D^{1/2} v^{1/2}$, where n is the number of electrons transferred, c the analyte concentration, A the geometric area and v the scan rate. Note that hydrazine oxidation is a four-electron transfer reaction, hence n = 4 and that the first electron transfer has been assumed rate-determining[29, 30].

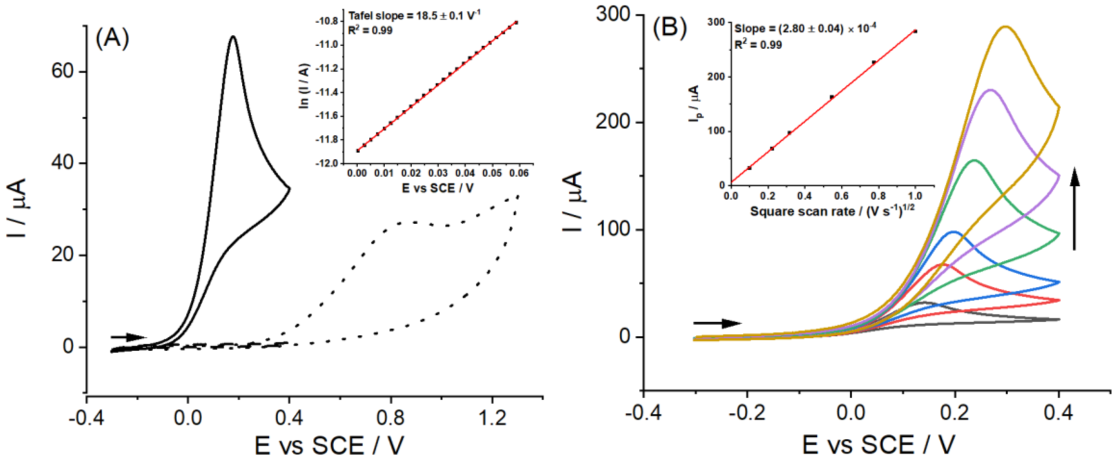

Figure 8.1. (A) Voltammograms in 0.1 M PBS of pH 7.0 at a scan rate of 50 mV/s: with 1.5 mM hydrazine at a Pd macrodisc electrode (solid curve), with 1.5 mM hydrazine at a GC macrodisc electrode (dot curve) and without hydrazine at a Pd macrodisc electrode (dash curve). (B) Voltammograms at the Pd macrodisc electrode in 0.1 M PBS of pH 7.0 with 1.5 mM hydrazine at variable scan rates (10/50/100/300/600/1000 mV/s). Note that the oxidative current values were obtained after baseline correction. The transverse arrows indicate the start and direction of the voltammetric scans. The vertical arrow indicates the increasing scan rates.

Having shown that bulk Palladium is electro-catalytic towards hydrazine oxidation, at least in comparison with carbon we next investigated whether this catalysis was changed at the nanoscale and work focused on the hydrazine oxidation at the GC electrode modified with variable coverages of Pd NPs in 1.5 mM hydrazine supported by 0.1 M PBS of pH 7.0. The characterisations of the drop-casted Pd nanoparticles via scanning electron microscopy (SEM) and transmission electron microscopy (TEM) are reported in the Appendix Section A8.2. The different coverage corresponded to 2/6/7/8/12/15/18 layers of nanoparticles where the number of layers is estimated by assuming that the Pd NPs are spherical with a radius of 12.4 nm (from the TEM image) and arranged in a close packed hexagonal structure. The estimation of coverage and roughness is shown in the Appendix Section A8.1. For the higher nanoparticle coverages, as shown in Figure A8.1, the drop-casted layers are essentially continuous over the electrode surface and have a high degree of porosity. The corresponding voltammograms at the voltage scan rate of 50 mV/s are plotted in Figure 8.2A. Significant cathodic peak potential shifts are seen for Pd NP/GC (solid curves) in comparison with Pd bulk (dash curve), suggesting a possible superior catalytic ability of Pd NPs towards hydrazine oxidation, since the peak potential at bulk Pd of 0.18 V vs. SCE shifts to -0.20 V vs. SCE for the maximum coverage studied. Note that as reported above the GC surface has a negligible response at the potentials studied.

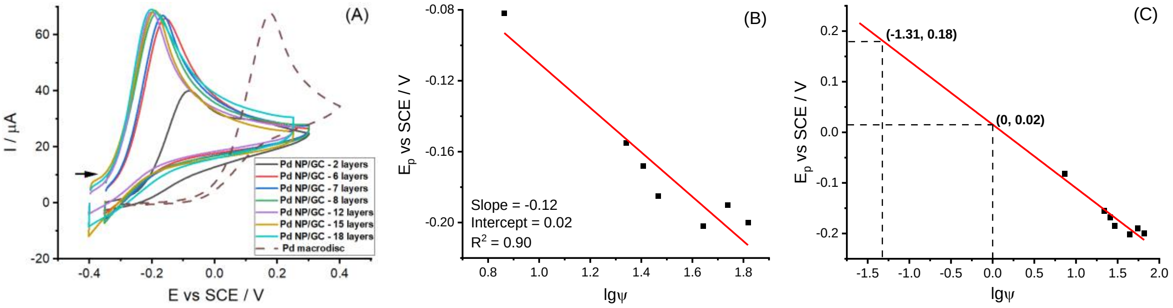

Figure 8.2. (A) Voltammograms at a Pd NP modified GC macrodisc electrodes with variable coverage (2/6/7/8/12/15/18, solid curves) and at a Pd macro-disc electrode (dash curve) in 0.1 M PBS of pH 7.0 at 50 mV/s. The transverse arrow indicates the start and direction of the voltammetric scans. (B) Plot of the peak potentials E_p obtained at Pd NP modified GC macro-disc electrodes versus the logarithm of the modification coverage lgψ. (C) The extrapolation upon the fitting line in Figure 8.2B.

Interestingly the average baseline-corrected peak current density J calculated using the geometric area of the electrode as reported (9.22 ± 0.20 A/m^2) in Table 8.1 seen on the drop-casted electrodes is very close to that seen at Pd bulk (9.48 ± 0.07 A/m^2) suggesting that the voltammetric response again corresponds to that of semi-infinite diffusion with an electrochemical reaction which is overall four-electron and with the first electron transfer rate-determining. Note that the peak current data for variable coverages shows that full coverage (from a diffusional perspective) was only realised for more than 2 layers, corresponding to the values in the table. The inference of the rate-determining step was confirmed via Tafel analysis of the voltammograms obtained for different coverages of Pd nanoparticles. The measured anodic transfer coefficients, β, are summarised in Table 8.1 which shows that the values are, within experimental error the same as for bulk Pd.

Table 8.1. Peak current density and anodic transfer coefficient of hydrazine oxidation at the bulk Pd and the Pd NP/GC of variable drop-casting coverages

Layers	**6**	**7**	**8**	**12**	**15**	**18**	**Bulk**
J (A/m^2)	9.12	9.19	9.24	9.34	9.19	9.25	9.48
	± 0.10	± 0.09	± 0.08	± 0.09	± 0.09	± 0.11	± 0.07
β	0.47	0.48	0.47	0.49	0.49	0.49	0.48
	± 0.01	± 0.01	± 0.01	± 0.01	± 0.01	± 0.01	± 0.01

Significantly the peak potentials of the voltammograms seen at the drop-casted electrode surfaces can be seen in Figure 8.2A to systematically move cathodically with an increase in the coverage of Pd nanoparticles leading to a value more negative than ca. -0.2 V vs. SCE for coverages in excess of 12 layers. The variation of peak potential and the essential invariance of the peak current to coverage together with the close similarity of the peak current density to the bulk Pd signal suggest that although the hydrazine oxidation reaction has reached the full electrochemically irreversible limit[22], the *effective* electrochemical rate constant of the oxidation seemingly increases with the loading of the drop-casted Pd NPs at the GC surface. As discussed above the peak potential in a voltammogram reflects a balance between the mass transport and the rate of the electrochemical reaction. The similarity of the peak current densities as measured relative to the geometric area of the electrode indicates that the mass transport is controlled by semi-infinite diffusion. The effective electrochemical rate constant for an electrochemically irreversible electrode reaction at a rough/porous surface has been studied by Ward et al.[22, 31] via detailed simulation who considered both the electrochemical rate constant and the effective area of the particles forming the conductive porous layer. Ward established the following equation

$$E_p = E_f^0 + \frac{RT}{\beta F}\left[0.780 - 2.303\lg\left(\psi k^0\right) + \ln\left(\sqrt{\frac{\beta F D v}{RT}}\right)\right] \tag{8.1}$$

where E_f^0 is the formal potential, k^0 the standard electrochemical rate constant and ψ the roughness factor (ψ = total surface area of electroactive nanoparticles/substrate geometric area). The total surface area of the nanoparticles used to modify the electrode for each coverage was calculated assuming spherical particles of radius 12.4 nm (from the TEM image) and a plot of experimental E_p vs. $\lg\psi$ was then made and analysed as shown in Figure 8.2B giving a slope of -0.12 ± 0.01, from which β can be deduced to be 0.49 ± 0.03. This value is in good agreement with that extracted from the voltammogram via Tafel analysis, suggesting that the cathodic potential shift resulting from the coverage change is (at least partially) controlled by the physical surface roughness leading to an enhanced total surface area of electro-catalytic Pd. Figure 8.2C displays the extrapolation of the fitting line in Figure 8.2B, from which notably as $\lg\psi = 0$ ($\psi = 1$) theoretically corresponding to bulk Pd, the peak potential is ca. 0.02 V vs. SCE. This is less than the experimentally measured one (0.18 V) in Figure 8.2A (dash curve). The results suggest that the modification of the GC electrode with Pd nanoparticles creates a surface which is electro-catalytic towards hydrazine oxidation partly because of a surface area effect and additionally partly because the Pd nanoparticles are more chemically catalytic than bulk Pd.

Next the standard electrochemical rate constants for the nanoparticles and for the bulk Pd were considered and the rate constant ratio $k_{\mathrm{Pd\ NP/GC}}^0/k_{\mathrm{Pd}}^0$ was introduced to quantitatively describe the enhanced catalytic ability from Pd NPs, in contrast to Pd bulk, on the electrochemical rate constant. Herein, $k_{\mathrm{Pd\ NP/GC}}^0$ and $k_{\mathrm{Pd\ bulk}}^0$ are the electrochemical rate constants of hydrazine oxidation at the Pd NP/GC and Pd macrodisc electrode respectively. Comparison of the two rate constants indicates the relative electro-catalytic activity of the two types of palladium, bulk and nano-particulate. By measuring the peak potential variation with coverage as plotted in Figure 8.2B and comparing with the peak potential for bulk Pd where the electrochemical surface area is approximated by the geometrical area multiplied by a surface roughness, it is possible to estimate the ratio of $k_{\mathrm{Pd\ NP/GC}}^0/k_{\mathrm{Pd\ bulk}}^0$ of 43 ± 11, suggesting the electrochemical rate constant was increased by around 43 times due to differences in chemical reactivity at the nanoparticles as compared to the bulk Pd. Note that by using Ward's equation as the basis for the plot in Figure 8.2B the changes in area are accounted for so that the ratio of electrochemical rate constants reflects the changed chemical catalysis separate from the physical effects of the altered area. Note that the error of the ratio results from the possible surface roughness of Pd bulk ($\psi = 1.6 \pm 0.4$)[32-35]. The details of the estimation of the electrochemical rate constant ratio are given in the Appendix Section A8.3.

To further confirm the above insights we next investigated Pd electrodes modified with Pd nanoparticles where microscopy again indicated the evolution of agglomerates/aggregates of Pd nanoparticles developing on the surface with an increased coverage of nanoparticles. Figure 8.3 shows that modifying a bulk Pd electrode with 6 layers of Pd NPs leads to a very similar shift of potential as seen on the GC electrode thus ruling out substrate effects and allowing a measure of the ratio $k_{\mathrm{Pd\ NP/Pd}}^0/k_{\mathrm{Pd\ bulk}}^0$ which was found to be 32 ± 8 in good agreement with the ratio $k_{\mathrm{Pd\ NP/GC}}^0/k_{\mathrm{Pd\ bulk}}^0$ determined above, where $k_{\mathrm{Pd\ NP/Pd}}^0$ is the standard electrochemical rate constant of hydrazine oxidation at the Pd NP/Pd.

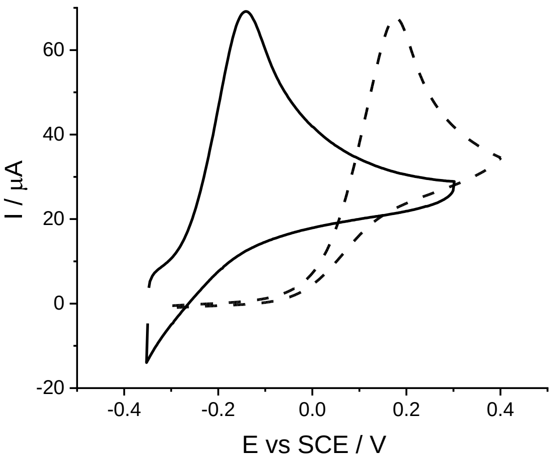

Figure 8.3. Voltammograms in 0.1 M PBS of pH 7.0 at the scan rate of 50 mV/s at the Pd NP modified Pd macrodisc electrode of 6 layers (solid curve) and Pd macrodisc electrode (dash curve).

Last it is interesting to look at the voltammetry of hydrazine oxidation for sparse coverages of nanoparticles. Specifically we considered 0.02, 0.1 and 0.2 layers of the Pd NP/GC. As illustrated in Figure 8.4, three types of peaks were observed as labelled 1, 2 and 3 where Peaks 1 and 2 emerged on the addition of increased Pd nanoparticles to the surface and Peak 3 was related to the response of the unmodified GC electrode in the absence of hydrazine (see Appendix Section A8.4). Noting that the scanning electron microscopy images in Figure A8.1 showed that the low coverage surfaces were comprised of individual nanoparticles or tiny agglomerates together with larger agglomerates with the latter evolving into the porous structures noted above, Peak 1, absent at very low coverages, was assigned to the response of large aggregates whilst peak 2, dominant at very low coverages was assigned to individual Pd NPs or tiny agglomerates. It is interesting that two voltammetric peaks result from one simple modification of the (inactive) electrode surface and this further confirms the above inference that both physical and chemical effects can cause catalysis. Thus the small shift in peak potential seen relative to bulk Pd for Peak 2 confirms the chemical catalysis whereas the larger shift from Peak 1 reflects both the changed catalysis and the increased surface area of the surface agglomerates as they grow with increased coverage into the layers which can once of a sufficient size be analysed according to Ward's equation. Interpretation of the relative sizes on Peaks 1 and 2 is governed at least in principle by the overlap of the different diffusional fields of the electrochemical heterogeneous surface.[19]

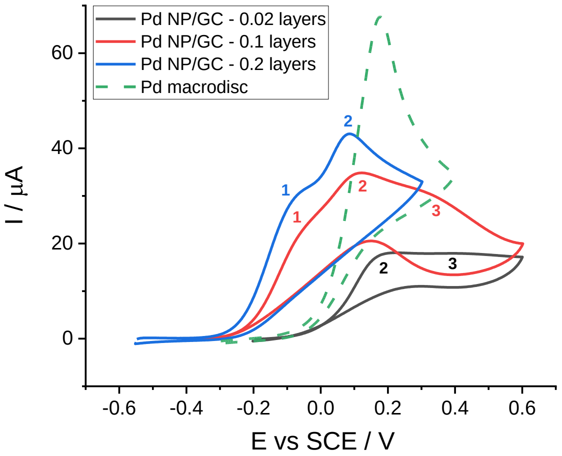

Figure 8.4. Voltammograms in 0.1 M PBS of pH 7.0 at 50 mV/s: (black curve) Pd NP modified GC macrodisc electrode of 0.02 layers, (red curve) Pd NP modified GC macrodisc electrode of 0.1 layers, (blue curve) Pd NP modified GC macrodisc electrode of 0.2 layers and (green curve) Pd macrodisc.

8.4 Conclusions

In conclusion, the catalysis of the electro-oxidation of hydrazine by palladium has been investigated both at the macro- and nano-scales. Specifically the response of layers of nanoparticles deposited on an electrode surface have been studied and the voltammetric responses analysed quantitatively. In this way it is revealed that both surface area effects and changes of chemical catalytic behaviour contribute to the reduction in over-potential noted at the modified electrodes in comparison with bulk Palladium. The results have specific importance for the case of hydrazine and also generic significance in highlighting the essential need to dissect physical and chemical effects in electrochemical catalysis.

Appendix

Section A8.1: Estimation of the number of drop casted layers and the surface roughness

As indicated in the Experimental section above, certain volume $V_{dropcast}$ (7 μL in this work) of the Pd NP suspension with concentration c was drop-casted onto polished GC or Pd macrodisc substrates with geometric area $A_{geometric}$, and dried under a N_2 atmosphere, forming a wide range of 0.02 ~ 18 layers of Pd NPs. The amount $m_{dropcast}$ of Pd NPs drop-casted on the surface was estimated:

$$m_{dropcast} = cV_{dropcast} \tag{8.2}$$

For single Pd nanoparticle with diameter d (assumed as sphere) and density ρ, its mass is estimated:

$$m_{single\ Pd\ NP} = \frac{\pi}{6}\rho d^3 \tag{8.3}$$

Hence, the number N of drop-casted Pd NPs is

$$N = \frac{m_{dropcast}}{m_{single\ Pd\ NP}} = \frac{6cV_{dropcast}}{\pi\rho d^3} \tag{8.4}$$

Assume that the drop-casted Pd NPs are arranged in a hexagonal close packed structure. The projected area $A_{project\text{ - }single\ Pd\ NP}$ of each Pd NP is

$$A_{project\text{ - }single\ Pd\ NP} = \frac{\sqrt{3}}{2}d^2 \tag{8.5}$$

Thus, the total projected area $A_{project\text{ - }total\ Pd\ NPs}$ of drop-casted Pd NPs is

$$A_{project\text{ - }total\ Pd\ NPs} = NA_{project\text{ - }single\ Pd\ NP} = \frac{3\sqrt{3}cV_{dropcast}}{\pi\rho d} \tag{8.6}$$

Hence, the number L of the drop-casted layers is

$$L = \frac{A_{\text{project - total Pd NPs}}}{A_{\text{geometric}}} = \frac{3\sqrt{3}cV_{\text{dropcast}}}{\pi \rho d A_{\text{geometric}}} \tag{8.7}$$

Moreover, the surface area $A_{\text{surface - single Pd NP}}$ of single Pd NP is

$$A_{\text{surface - single Pd NP}} = \pi d^2 \tag{8.8}$$

Thus, the total surface area $A_{\text{surface - total Pd NPs}}$ of drop-casted Pd NPs is

$$A_{\text{surface - total Pd NPs}} = N A_{\text{surface - single Pd NP}} = \frac{6cV_{\text{dropcast}}}{\rho d} \tag{8.9}$$

Hence, the roughness factor ψ (ψ = total surface area of electroactive nanoparticles/substrate geometric area) is

$$\psi = \frac{A_{\text{surface - total Pd NPs}}}{A_{\text{geometric}}} = \frac{6cV_{\text{dropcast}}}{\rho d A_{\text{geometric}}} \tag{8.10}$$

Section A8.2: Characterisation of drop-casted Pd nanoparticles

Scanning Electron Microscopy (SEM)

The drop-casted Pd nanoparticles of different coverages (0.2, 2 and 6 layers) were first characterised by scanning electron microscopy (SEM, Zeiss Sigma 300 FEG) with an accelerating voltage of 2.0 kV. The SEM samples were prepared using a glassy carbon stub and mirrored the dropcast procedures in the electrochemical experiments. The stub containing the dropcast samples were dried overnight prior to the SEM imaging. In the work revealed by Zhang et al.[36], heterogeneous particle distribution from the centre to the edge of the dropcast is not uncommon due to the 'coffee ring' effect. As a result, to allow meaningful comparison between different particle loadings, the SEM images in Figure A8.1 shows the central region of the dropcast ring at low coverage of 0.2 layers, which reveals numerous porous clusters due to the agglomeration of Pd nanoparticles. In addition to the clusters, some tiny agglomerates and individual Pd nanoparticles (nominally < 25 nm reported in the supplier's specification) can be seen in the inlay of Figure A8.1D. As the loading of Pd NPs increases from the coverage of 0.2 to 6 layers the size and number of the clusters can be seen to increase to eventually form a thick layer on the substrate with high porosity. Such behaviour is well known, reported and reviewed[37], and is common for metal nanoparticles like Pt[36], Ag[38] and Au[39], as well as carbon nanotubes[40, 41].

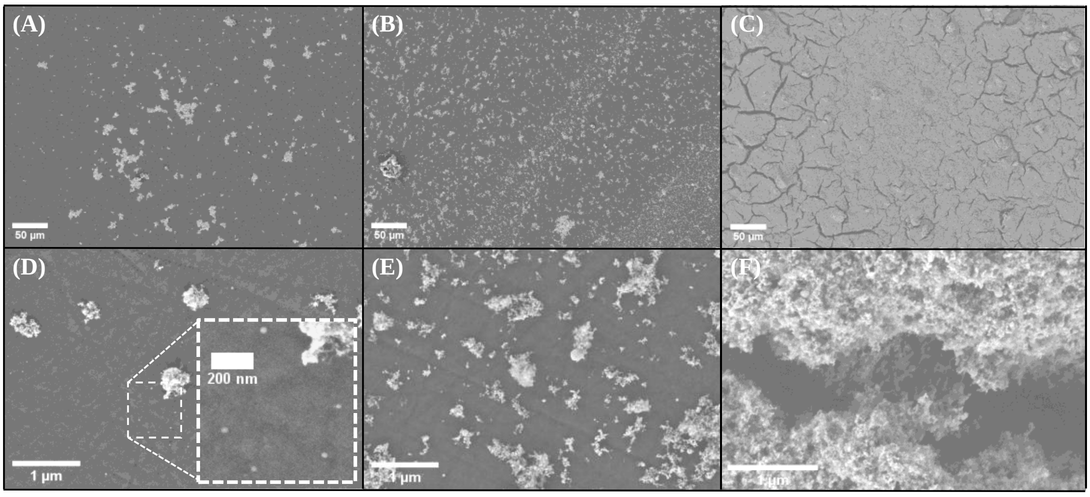

Figure A8.1. SEM images of drop-casted Pd nanoparticles onto glassy carbon: (A) and (D) 0.2 layers, (B) and (E) 2 layers, and (C) and (F) 6 layers. (A-C) with a scale bar of 50 μm and (D-F) with a scale bar of 1 μm.

Transmission Electron Microscopy (TEM)

Transmission electron microscopy (TEM, FEI Tecnai T12) at an accelerating voltage of 120 kV was then deployed for extracting smaller scale information of the drop-casted Pd NPs. The solution containing the Pd NPs was drop-casted onto a carbon grid supported by copper (AGS160, Agar Scientific Ltd., UK). The substrate was dried overnight prior to TEM imaging. Figure A8.2A shows a large agglomerate of Pd NPs together with a few smaller agglomerates as well as some dispersed quasi-spherical individual particles. The diameter distribution of the individual Pd NPs is presented in Figure A8.2B, and the mean value was estimated to be 12.4

± 5.4 nm (98 measurements).

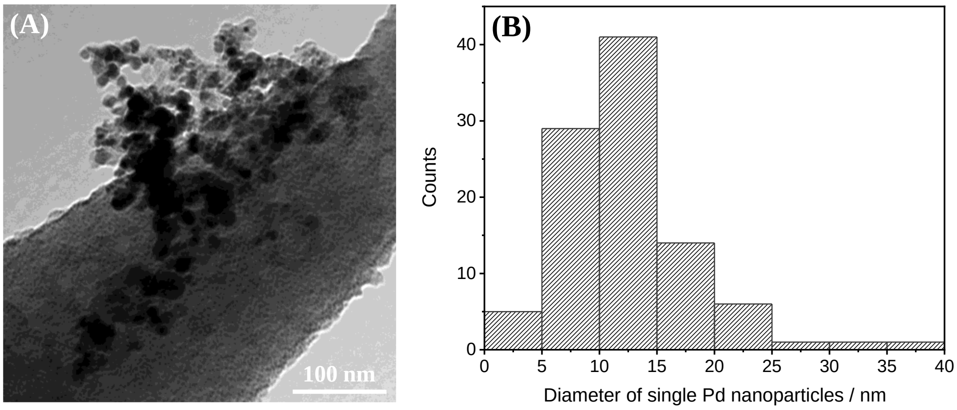

Figure A8.2. (A) TEM image of Pd nanoparticles drop-casted onto a copper-carbon TEM grid. (B) The diameter distribution of single Pd nanoparticles as measured from the TEM image using ImageJ.

Section A8.3: Estimation of the electrochemical rate constant ratio

As reported by Ward et al.[22, 31], the effective electrochemical rate constant for an electrochemically irreversible electrode reaction at a rough/porous surface follows the equation:

$$E_p = E_f^0 + \frac{RT}{\beta F}\left[0.780 - \ln\left(\psi k^0\right) + \ln\left(\sqrt{\frac{\beta F D v}{RT}}\right)\right] \tag{8.11}$$

where E_p is the peak potential of the studied voltammogram, E_f^0 the formal potential, R the gas constant, T the temperature, β the anodic transfer coefficient, F the Faraday constant, D the diffusion coefficient of the analyte, ψ the roughness factor, k^0 the standard electrochemical rate constant and v the voltage scan rate.

Then the rate constant ratios $k_{\text{Pd NP/GC}}{}^0/k_{\text{Pd}}{}^0$ and $k_{\text{Pd NP/Pd}}{}^0/k_{\text{Pd}}{}^0$ were introduced to quantify the enhanced catalytic ability of drop-casted Pd NPs at GC and Pd surfaces respectively, on the electrochemical rate constant of the oxidation of hydrazine, in comparison with the bulk Pd. The ratios were obtained as followed:

$$\frac{k^0_{Pd\,NP/GC}}{k^0_{Pd\,bulk}} = \frac{\psi_{Pd\,bulk}}{\psi_{Pd\,NP/GC}} e^{\frac{\beta F}{RT}\left(E_{p-Pd\,bulk} - E_{p-Pd\,NP/GC}\right)} = 43 \pm 11 \tag{8.12}$$

$$\frac{k^0_{Pd\ NP/Pd\ bulk}}{k^0_{Pd\ bulk}} = \frac{\psi_{Pd\ bulk}}{\psi_{Pd\ NP/Pd\ bulk}} e^{\frac{\beta F}{RT}\left(E_{p-Pd\ bulk} - E_{p-Pd\ NP/Pd\ bulk}\right)} = 32 \pm 8 \qquad (8.13)$$

where $\psi_{\mathrm{Pd\ bulk}}$ is the roughness factor (1.6 ± 0.4) of the Pd bulk surface[32-35]; $\psi_{\mathrm{Pd\ NP/GC}}$ and $\psi_{\mathrm{Pd\ NP/Pd}}$ correspond to the roughness factors via the estimation in the Appendix Section A8.1 for Pd NPs drop-casted onto the GC surface and onto the Pd bulk surface respectively; $E_{\mathrm{p\text{-}Pd\ bulk}}$ is the measured peak potential (0.18 V vs. SCE) at the Pd macrodisc electrode; $E_{\mathrm{p\text{-}Pd\ NP/GC}}$ and $E_{\mathrm{p\text{-}Pd\ NP/Pd\ bulk}}$ correspond to the peak potentials measured at Pd NPs/GC (-0.155 V vs. SCE) and Pd NPs/Pd bulk (-0.14 V vs. SCE) of 6 layers respectively.

Section A8.4: Voltammograms at a sparsely covered Pd NP/GC (0.02 layers)

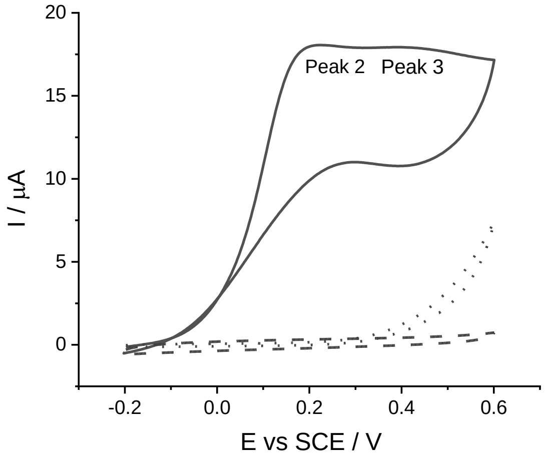

Figure A8.3. Voltammograms in 0.1 M PBS of pH 7.0 at 50 mV/s: with 1.5 mM hydrazine at the Pd NP modified GC macrodisc electrode of 0.02 layers (solid curve), without hydrazine at the Pd NP modified GC macrodisc electrode of 0.02 layers (dash curve) and with 1.5 mM hydrazine at the bare GC macrodisc electrode (dot curve).

References

[1] R. Miao, M. Yang, R.G. Compton, The electro-oxidation of hydrazine with Palladium nanoparticle modified electrodes: Dissecting chemical and physical effects: catalysis, surface roughness, or porosity?, J. Phys. Chem. Lett., 12 (2021) 6661-6666.

[2] X. Chia, M. Pumera, Characteristics and performance of two-dimensional materials for electrocatalysis, Nat. Catal., 1 (2018) 909-921.

[3] Z.-F. Huang, J. Song, Y. Du, S. Xi, S. Dou, J.M.V. Nsanzimana, C. Wang, Z.J. Xu, X. Wang, Chemical and structural origin of lattice oxygen oxidation in Co-Zn oxyhydroxide oxygen evolution electrocatalysts, Nat. Energy, 4 (2019) 329-338.

[4] T.D. Thanh, J. Balamurugan, H. Van Hien, N.H. Kim, J.H. Lee, A novel sensitive sensor for serotonin based on high-quality of AuAg nanoalloy encapsulated graphene electrocatalyst, Biosens. Bioelectron., 96 (2017) 186-193.

[5] P. Balasubramanian, M. Annalakshmi, S.-M. Chen, T.-W. Chen, Ultrasensitive non-enzymatic electrochemical sensing of glucose in noninvasive samples using interconnected nanosheets-like NiMnO3 as a promising electrocatalyst, Sens. Actuators B Chem., 299 (2019) 126974.

[6] Z. Chang, J. Xu, X. Zhang, Recent progress in electrocatalyst for Li-O_2 batteries, Adv. Energy Mater., 7 (2017) 1700875.

[7] J. He, A. Manthiram, A review on the status and challenges of electrocatalysts in lithium-sulfur batteries, Energy Storage Mater., 20 (2019) 55-70.

[8] S. Alim, J. Vejayan, M.M. Yusoff, A. Kafi, Recent uses of carbon nanotubes & gold nanoparticles in electrochemistry with application in biosensing: a review, Biosens. Bioelectron., 121 (2018) 125-136.

[9] S. Shrivastava, N. Jadon, R. Jain, Next-generation polymer nanocomposite-based electrochemical sensors and biosensors: A review, Trends Analyt. Chem., 82 (2016) 55-67.

[10] W. Wei, K. Sun, Y.H. Hu, Synthesis of 3D cauliflower-fungus-like graphene from CO_2 as a highly efficient counter electrode material for dye-sensitized solar cells, J. Mater. Chem. A, 2 (2014) 16842-16846.

[11] Q. Wang, W. Zheng, H. Chen, B. Zhang, D. Su, X. Cui, Plasmonic-induced inhibition and enhancement of the electrocatalytic activity of Pd-Au hetero-nanoraspberries for ethanol oxidation, J. Power Sources, 316 (2016) 29-36.

[12] H. Zhang, X. Qiu, Y. Chen, S. Wang, S.E. Skrabalak, Y. Tang, Shape Control of Monodispersed Sub-5 nm Pd Tetrahedrons and Laciniate Pd Nanourchins by Maneuvering the Dispersed State of Additives for Boosting ORR Performance, Small, 16 (2020) 1906026.

[13] F. Xu, Z. Tang, S. Huang, L. Chen, Y. Liang, W. Mai, H. Zhong, R. Fu, D. Wu, Facile synthesis of ultrahigh-surface-area hollow carbon nanospheres for enhanced adsorption and energy storage, Nat. Commun., 6 (2015) 1-12.

[14] S. Dang, Q.-L. Zhu, Q. Xu, Nanomaterials derived from metal–organic frameworks, Nat. Rev. Mater., 3 (2017) 1-14.

[15] W.-J. Jiang, W.-L. Hu, Q.-H. Zhang, T.-T. Zhao, H. Luo, X. Zhang, L. Gu, J.-S. Hu, L.-J. Wan, From biological enzyme to single atomic Fe–N–C electrocatalyst for efficient oxygen reduction, Chem. Commun., 54 (2018) 1307-1310.

[16] L. Liu, X. Yang, N. Ma, H. Liu, Y. Xia, C. Chen, D. Yang, X. Yao, Scalable and cost-effective synthesis of highly efficient Fe_2N-based oxygen reduction catalyst derived from seaweed

biomass, Small, 12 (2016) 1295-1301.

[17] S. Kaviya, E.J.A.M. Prasad, Sequential detection of Fe^{3+} and As^{3+} ions by naked eye through aggregation and disaggregation of biogenic gold nanoparticles, Anal. Methods, 7 (2015) 168-174.

[18] L. Wang, Z. Sofer, M. Pumera, Will any crap we put into graphene increase its electrocatalytic effect?, ACS nano, 14 (2020) 21-25.

[19] R.G. Compton, C.E. Banks, Understanding Voltammetry, World Scientific, 2018.

[20] H.H. Girault, Analytical and Physical Electrochemistry, EPFL Press, New York, 2004.

[21] E. Kätelhön, L. Chen, R.G. Compton, Nanoparticle electrocatalysis: Unscrambling illusory inhibition and catalysis, Appl. Mater. Today, 15 (2019) 139-144.

[22] K.R. Ward, M. Gara, N.S. Lawrence, R.S. Hartshorne, R.G. Compton, Nanoparticle modified electrodes can show an apparent increase in electrode kinetics due solely to altered surface geometry: The effective electrochemical rate constant for non-flat and non-uniform electrode surfaces, J. Electroanal. Chem., 695 (2013) 1-9.

[23] N.V. Rees, R.G. Compton, Carbon-free energy: a review of ammonia-and hydrazine-based electrochemical fuel cells, Energy Environ. Sci., 4 (2011) 1255-1260.

[24] A. Serov, C. Kwak, Direct hydrazine fuel cells: A review, Appl. Catal. B, 98 (2010) 1-9.

[25] P.B. Deroco, I.G. Melo, L.S. Silva, K.I. Eguiluz, G.R. Salazar-Banda, O. Fatibello-Filho, Carbon black supported Au-Pd core-shell nanoparticles within a dihexadecylphosphate film for the development of hydrazine electrochemical sensor, Sens. Actuators B Chem., 256 (2018) 535-542.

[26] F. Gao, Q. Wang, N. Gao, Y. Yang, F. Cai, M. Yamane, F. Gao, H. Tanaka, Hydroxyapatite/chemically reduced graphene oxide composite: Environment-friendly synthesis and high-performance electrochemical sensing for hydrazine, Biosens. Bioelectron., 97 (2017) 238-245.

[27] Potassium Phosphate (pH 5.8 to 8.0) Preparation, AAT Bioquest, Inc, 2021.

[28] D. Li, C. Lin, C. Batchelor-McAuley, L. Chen, R.G. Compton, Tafel analysis in practice, J. Electroanal. Chem., 826 (2018) 117-124.

[29] V. Rosca, M. Duca, M.T. de Groot, M.T. Koper, Nitrogen cycle electrocatalysis, Chem. Rev., 109 (2009) 2209-2244.

[30] R. Miao, R.G. Compton, The Electro-Oxidation of Hydrazine: A Self-Inhibiting Reaction, J. Phys. Chem. Lett., 12 (2021) 1601-1605.

[31] K.R. Ward, R.G. Compton, Quantifying the apparent ‘catalytic’effect of porous electrode surfaces, J. Electroanal. Chem., 724 (2014) 43-47.

[32] S. Henning, J. Herranz, H.A. Gasteiger, Bulk-palladium and palladium-on-gold electrocatalysts for the oxidation of hydrogen in alkaline electrolyte, J. Electrochem. Soc., 162 (2014) F178.

[33] T. Chierchie, C. Mayer, W. Lorenz, Structural changes of surface oxide layers on palladium, J. Electroanal. Chem. Interf. Electrochem., 135 (1982) 211-220.

[34] A. Bolzan, M. Martins, A. Arvia, The complex processes involved at Pd electrodes in 1 M H_2SO_4 in the potential range of oxygen electroadsorption-electrodesorption reactions, J. Electroanal. Chem. Interf. Electrochem., 157 (1983) 339-358.

[35] D. Rand, R. Woods, The nature of adsorbed oxygen on rhodium, palladium and gold electrodes, J. Electroanal. Chem. Interf. Electrochem., 31 (1971) 29-38.

[36] Y. Zhang, A.K. Selva Kumar, D. Li, M. Yang, R.G. Compton, Nanoparticle-and Nanotube-

Modified Electrodes: Response of Drop-Cast Surfaces, ChemElectroChem, 7 (2020) 4614-4624.

[37] A.K.S. Kumar, Y. Zhang, D. Li, R.G. Compton, A Mini-review: how reliable is the drop casting technique?, Electrochem. Commun., (2020) 106867.

[38] A.L. Suherman, K. Ngamchuea, E.E. Tanner, S.V. Sokolov, J. Holter, N.P. Young, R.G. Compton, Electrochemical detection of ultratrace (picomolar) levels of Hg^{2+} using a silver nanoparticle-modified glassy carbon electrode, Anal. Chem., 89 (2017) 7166-7173.

[39] A.L. Suherman, G. Zampardi, S. Kuss, E.E. Tanner, H.M. Amin, N.P. Young, R.G. Compton, Understanding gold nanoparticle dissolution in cyanide-containing solution via impact-chemistry, Phys. Chem. Chem. Phys., 20 (2018) 28300-28307.

[40] K. Chiou, S. Byun, J. Kim, J. Huang, Additive-free carbon nanotube dispersions, pastes, gels, and doughs in cresols, Proc. Natl. Acad. Sci. U.S.A., 115 (2018) 5703-5708.

[41] W.J. Lee, A.J. Clancy, J.C. Fernández-Toribio, D.B. Anthony, E.R. White, E. Solano, H.S. Leese, J.J. Vilatela, M.S. Shaffer, Interfacially-grafted single-walled carbon nanotube/poly (vinyl alcohol) composite fibers, Carbon, 146 (2019) 162-171.

Conclusions

In this thesis, electrochemical methods including cyclic voltammetry, chronoamperometry and nano-impacts, were employed to probe the reaction mechanism and electron transfer kinetics of hydrazine oxidation.

Firstly, the response of individual palladium decorated graphene oxide particles (Pd/GO) which act as individual nanoelectrodes, was studied in terms of catalysing both the hydrogen oxidation reaction (HOR) and the hydrogen evolution reaction (HER). Impact electrochemistry revealed that only the part of the graphene oxide (GO) particle physically close to the point of contact between the platelet and the impacted electrode is active, due to the high resistance of the ultrathin GO. This electrochemical characterisation upon Pd/GO was essential for the following study upon its catalysis towards hydrazine oxidation via *nano-impacts*.

To understand intrinsically the reaction of hydrazine electro-oxidation, the priority of our work was placed on the theory model for describing the voltammetric behaviour of the reaction. The widely used Butler-Volmer (BV) theory was evidenced to be not appropriate for elucidating the electron transfer kinetics of hydrazine oxidation. The study of the electro-oxidation at a non-adsorbing carbon surface shows that the transfer coefficient is in fact markedly potential dependent and is well described by the symmetric Marcus-Hush (sMH) theory which indicates a reorganization energy of *ca.* 0.35 eV.

The further investigation upon the reaction mechanism of hydrazine oxidation was conducted at the glassy carbon surface. It was found that the protonated hydrazine species $N_2H_5^+$ is electro-inactive, and the protons released from the oxidation of the unprotonated species N_2H_4

combine with the unreacted N_2H_4 diffusing to the electrode surface via changing the local pH. This synchronous combination reaction results in the formation of the inactive $N_2H_5^+$ so to inhibit the overall oxidation process to a large extent. Meaningful electron transfer kinetics and protonation thermodynamics were quantitatively extracted from the voltammetric signals based on the Marcus-Hush theory via DIGISIM simulation.

Subsequently the catalysis of the individual Pd/GO towards hydrazine oxidation was explored in buffered solutions across a wide pH range of 2 – 11 via *nano-impacts*. In contrast to the observations for carbon electrodes, both N_2H_4 and $N_2H_5^+$ are evidenced to be electroactive with $N_2H_5^+$ showing significantly slower electron transfer kinetics. Given the very limited interconversion between N_2H_4 and $N_2H_5^+$ during the ultrashort voltammetric, diffusional timescale of the single entity voltammetry of individual Pd/GO particles, a general mechanism for hydrazine oxidation was established where the electrochemical signal has contributions from both species. The rate-determining steps for each oxidation involve no proton release accompanying the one electron transfer, which indicates the initial formation of radical cations, either in solution or adsorbed.

To seek further insights into the catalytic hydrazine oxidation at Palladium surfaces, the electrochemical analysis of hydrazine oxidation was carried out at both bulk and particulate palladium. An unexpected *long-lived* radical di-cation $N_2H_5^{\bullet 2+}$ was proven to exist around or on the surface of bulk Palladium, which is stable for a voltammetric timescale of *ca.* seconds. The di-cation was demonstrated to originate from the oxidation of the hydrazinium cation. Additionally in terms of palladium nanoparticles, it was found that the catalysis upon hydrazine oxidation was controlled by both the physical roughness of the modified surface and the chemically enhanced catalytic ability of palladium nanoparticles. The apparent electrochemical rate constant of the reaction was quantified. This work provides a generic method for identifying the effective components of certain designed catalyst towards the reaction of interest, and proposed a quantitative indicator for the catalyst performance allowing the dissection of the chemical and physical contributions to the catalysis.

In summary, this thesis focuses on the exploration into the reaction mechanism and electron transfer kinetics of the hydrazine oxidation in various electrolytes at surfaces including carbon, bulk Palladium, particulate Palladium and Pd/GO. At carbon surfaces, it was found that N_2H_4 is the only electro-active species and the oxidation reaction of hydrazine follows the Marcus-Hush theory; at Palladium surfaces, both N_2H_4 and $N_2H_5^+$ were evidenced to be electro-active, and an unexpected long-lived radical di-cation $N_2H_5^{\bullet 2+}$ was observed (originating from the oxidation of hydrazinium cation) in terms of bulk Palladium, as well as the superior catalytic ability of particulate Palladium towards hydrazine oxidation is attributed to both physical roughness and enhanced chemical reactivity. The electrode kinetics of above situations were extracted successfully with the assistance of the software DIGISIM.

This thesis provides generic electrochemical methods to probe into the reaction mechanism and electron transfer kinetics, as well as physical and chemical insights upon the widely-used reaction - hydrazine oxidation, which will be of significant interest to the broad chemical world and electrochemistry community. Next work may be the exploration into the nano-impact behaviour of individual Pd nanoparticles towards hydrazine oxidation, as well as the comparison between the widely-used catalysts (eg. Pt, Au, Ag) and Pd in terms of the catalytic ability towards hydrazine oxidation.